Techniques for Optical Tweezers & SLM Microscopy

Michael Peter Lee

School of Physics and Astronomy
College of Science and Engineering
University of Glasgow

A thesis submitted to the University of Glasgow in accordance with the requirements for the degree of Doctor of Philosophy.

September 18, 2014

Abstract

With the development of pixelated liquid crystal displays, a new paradigm has emerged in the field of optics. Essentially, these displays enable interfacing a computer program with light, and therefore allow a wide range of light beams to be created. In this thesis, I shall be using liquid crystal displays to create phase diffraction patterns and, in this case, the displays are more commonly referred to as Spatial Light Modulators (SLMs). One area where SLMs have shown particular promise is that of optical microscopy. Here, they have been used in two different applications, namely holographic optical tweezers and SLM microscopy; this thesis concerns both. The aim of the thesis is to explore and develop new techniques combining SLMs with microscopy.

The first part of this thesis goes into results of the experiments I have carried out in holographic optical tweezers. Hydrodynamic interactions play an important role in many physical and biological processes. I present experimental evidence for the partial synchronisation of the stochastic oscillations of two spheres in a bistable optical trap. This experiment showed that, even in the absence of an external driving force, a degree of synchronisation still exists due to the Brownian motion alone. I then describe a new procedure to protect the optical trap from contamination in sensitive samples. Microrheology using optical tweezers requires lengthy position measurements in order to obtain the linear viscoelastic properties of fluids and this measurement is often compromised by freely diffusing material entering the trap. I then apply rotational Doppler velocimetry to a particle spinning in an optical tweezers. This is the first time that structured illumination has been used to determine rotation rate in the micro regime.

The second part describes the development of an SLM microscope and a series of experiments I carried out with it. The set up of the microscope is described and images are characterised in terms of the point spread function. I also demonstrate the multimodal capabilities by diffracting three different images, each with a unique spatial frequency filter, onto a single camera chip. Next, I report the development of some new frequency

filters, namely holographic stereo microscopy and three variations, including stereo with defocus which mimics human binocular vision where we have two eyes (views) of the world, each having its own lens. I used 3D particle tracking to investigate sedimentation in a confined microscope sample. This experiment brought together SLM microscopy and optical tweezers to create a new technique for particle sizing, or study surface effects.

This thesis describes several new applications of SLMs in microscopy, with the common theme being that the SLM is placed in the Fourier plane of the sample. Both holographic optical tweezers and SLM microscopy have been expanded by the techniques I have developed. In future, this work will serve as foundation for the combination for 3D particle tracking and visualisation with SLM microscopy, whilst microrheology will benefit from the new approaches.

Contents

List of Tables

List of Figures

Publications

Related to this thesis

M. P. Lee, A. Arran, G. M. Gibson, M. Tassieri, N. R. Heckenberg, and M. J. Padgett. **Optical shield: measuring viscosity of turbid fluids using optical tweezers**, Optics Express, **20**, 12127–12132, 2012.

M. P. Lee, and M. J. Padgett. **Optical tweezers: a light touch**, Journal of Microscopy, **248**, 219–222, 2012.

A. Curran, **M. P. Lee**, M. J. Padgett, J. M. Cooper, and R. Di. Leonardo. **Partial synchronization of stochastic oscillators through hydrodynamic coupling**, Physical Review Letters, **108**, 240601, 2012.

M. P. Lee, G. M. Gibson, R. Bowman, S. Bernet, M. Ritsch-Marte, D. B. Phillips, and M. J. Padgett. **A multi-modal stereo microscope based on a spatial light modulator**. Optics Express **21**, 16541–16551, 2013.

M. P. Lee, G. M. Gibson, D. Phillips, M. J. Padgett, and M. Tassieri. **Dynamic stereo microscopy for studying particle sedimentation**. Optics Express **22**, 4671-4677, 2014.

D. Phillips, **M. Lee**, F. C. Speirits, S. M. Barnett, S. H. Simpson, M. P. J. Lavery, M. J. Padgett, and G. Gibson. **Rotational Doppler velocimetry to probe the angular velocity of spinning micro-particles**. Phys. Rev. A **90**, 011801, 2014.

R. Hay, D. Phillips, **M. Lee**, G. Gibson, and M. J. Padgett. **Four Directional stereo microscopy for 3D particle tracking with real time error estimation**. Optics Express **22**, 18662, 2014.

Unrelated to this thesis

M. Dienerowitz, **M. Lee**, G. Gibson, and M. Padgett. **Measuring nanoparticle flow with the image structure function**. Lab on a Chip, **13**, 2359–2363, 2013.

F. Ferri, A. DAngelo, **M. Lee**, A. Lotti, M. C. Pigazzini, K. Singh, and R. Cerbino. **Kinetics of colloidal fractal aggregation by differential dynamic microscopy**, The European Physical Journal-Special Topics, **199**, 139–148, 2011.

Conference Proceedings

A. Curran, **M. P. Lee**, R. Di Leonardo, M. J. Padgett. **Hydrodynamic assisted barrier escape**, SPIE NanoScience+ Engineering, 80970Q-80970Q-7, 2011.

M. P. Lee, G. Gibson, M. Tassieri, D. Phillips, S. Bernet, M. Ritsh-Marte, M. J. Padgett. **Spatial light modulation for improved microscope stereo vision and 3D tracking**, SPIE NanoScience+ Engineering, 881022-881022-8, 2013.

Acknowledgements

I am indebted to a number of people who helped me to write this thesis. I would like to thank my supervisor, Prof. Miles Padgett, for the opportunities and guidance he gave me during my PhD. Dr Johannes Courtial, my second supervisor, is acknowledged mainly for saying things like, "Running?" or, "Lunch?"

Dr Graham Gibson deserves a big "thank you" for his skill in the workshop, and being limitlessly helpful in the lab. Throughout my PhD, he has been a dependable post doc and has tolerated my occasionally questionable choice of music. Thank you for proof reading this thesis. Dr Manlio Tassieri has been enthusiastic driving force in my study. His encouragement and passion for the subject has gone along way to keep my work focused, and our discussion have always been good fun.

Dr Arran Curran took me on as an early PhD student to work with him on the work which now makes up Chapter 3 of this thesis. Moreover, I heard recently that he climbed a 7a at Bowden. Dr Maria Dienerowitz and I worked together on a paper which did not fit within the scope of this thesis. Maria's belief in that work made it a success, which is something I am glad to have learnt from her.

Dr Richard Bowman pioneered some the techniques used in this thesis, and I would like to thank him for answering my emails in great detail. More than this, Richard has shared his passion for hill running with me, and I am very grateful for the experiences of pain and rain I am now imbued with. I would like to thank Dr David Phillips for a number or things, including, proof reading this thesis, enthusiasm for the subject, helping out in a number of experiments and the recent post work visits to the pub.

I would like to thank Dr Neal Radwell for introducing me to board games, Daniel Giovannini for his references to films I have not seen, Baoqing Sun for showing me no mercy at table tennis, Martin Lavery for making everything seem more easy, Emma W-B for her cakes (ask her for her apple crumble recipe), Rueben Aspden for taking sarcasm to new levels and the rest of the Glasgow Optics Group for being top notch chums over the past few years. Thanks also to the baristas of Kember and Jones Fine Foods Emporium for obvious reasons.

During my third year, I had the role of Post Graduate student representative for the School of Physics and Astronomy. I would like to thank Dr Craig Buttar and Heather Lambie helping me in that role. I would also like to thank SUPA for supporting me during a 2 month secondment at Boulder Nonlinear Systems (BNS) during my fourth year. At

BNS I would like to thank Kelly Gregorak, Anna Linnenberger, Mike Taylor and Steve Serati for their hospitably during this time.

Finally, thanks to Cath Mitchell who has, over the course of my PhD, done the following: helped with a 3000 piece jigsaw, cooked my tea, helped me catch sheep, held my ropes, proof read this thesis and not complained (too much).

Declaration

I hereby declare that the work presented in this thesis is the result of my own work, except where explicit reference is made to the work of others. This work has not been presented in any previous application for a degree at this or any other institution.

Michael P. Lee

A record is not just a record,
Records can hold memories.

- Elizabeth Morris

I

Optical Tweezers

That light can exert a force is now well documented, although still somewhat beguiling. The force was predicted by J. C. Maxwell in, "A Treatise on Electricity and Magnetism," published in 1873 [1]. One of the first experimental demonstrations of radiation pressure from light was in 1901, where an experiment was performed using silvered microscope coverslips as mirrors suspended inside a de-pressurised bell-jar. The mirrors were illuminated with an arc lamp and were observed to rotate, proving the existence of radiation pressure [2].

It is worthwhile to note that this experiment and associated theory was done before the idea of a photon was suggested. The radiation pressure was inferred from the concept of light being a wave. As concluded by Maxwell,

"In a medium in which waves are propagated there is a pressure normal to the waves and numerically equal to the energy in unit volume."

With the advent of quantum mechanics, and the explanation of photons as the minimum unit of energy carried by a light beam, the force exerted by light could be interpreted as the transfer a photon's momentum to a scattering or absorbing object.

The momentum of a photon is given by $\mathbf{p} = \hbar\mathbf{k}$, where $\hbar$ is Planck's constant divided by 2π and $\mathbf{k}$ is the wave vector of the light, $|\mathbf{k}| = \frac{2\pi}{\lambda}$. The optical force arises from objects changing either the magnitude or direction of the momentum vector,

$$\mathbf{F} = \frac{\mathrm{d}\mathbf{p}}{\mathrm{dt}}. \tag{1.1}$$

where $\mathbf{F}$ is the optical force vector. For light scattering off a mirrored surface, as in the 1901 experiment, each photon is reflected at normal incidence. This means there is $2\hbar k$ of momentum per photon given to the mirror, Fig. 1.1. The number of photons per second is given by the power of the light source.

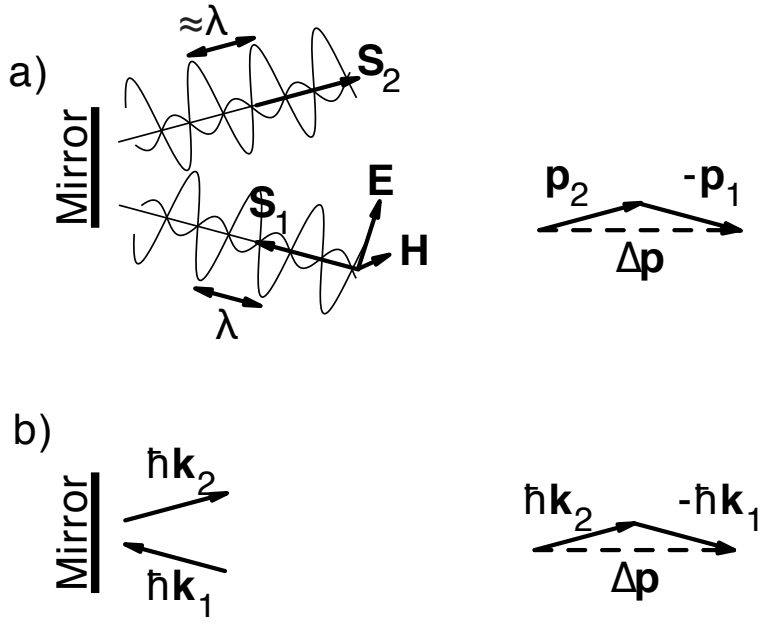

Figure 1.1: The wave and photon interpretations of radiation pressure on a mirror. a) shows the origin of radiation pressure for the point of view of light being a wave. $S_{1,2}$ are the incident and reflected Poynting vectors of the electromagnetic field near the mirror. The magnitude of the momentum is given by $\frac{U}{c}$, where U is the energy of the field, and the direction is given by the Poynting vector, $\mathbf{S} = \mathbf{E} \times \mathbf{H}$, where $\mathbf{E}$ and $\mathbf{H}$ are the electric and magnetic fields respectively. b) shows the photon interpretation. Each photon gives a $\Delta\mathbf{p}$ kick of momentum to the mirror.

The energy of one photon is given by $\mathrm{E} = \hbar\omega$, where ω is the angular frequency of the photon. As the photons in the experiment are close to being perfectly reflected, it seems as if the energy of the photon is unchanged. However, this cannot be the case as the mirror was initially at rest and was accelerated to some velocity, v, and therefore has an energy proportional to v^2. The origin of this energy must be from the light itself, and arises from a Doppler red shift of the photons reflecting off the moving surface, although this shift is usually ignored.

Everyday experience tells us that if there is an optical force, it must be particularly small. It is therefore perhaps inevitable that the phenomenon has found application in microscopy. An object's volume, and therefore mass, scales with the cube of its radius, meaning a factor of a million reduction in radius gives a 10^{18} reduction in mass. The first observation of microscopic particles being influenced by light came in 1969. Ten years after the invention of the laser, Ashkin [3] reported that a laser could accelerate microscopic particles at 10^5 times acceleration due to gravity. In his experiment, thermal effects were avoided by using transparent particles which did not absorb light, yet did deflect the light owing to the particles having a higher refractive index compared to the surrounding fluid (water). Ashkin reported that the particles were, "drawn in to the beam axis and accelerated in the direction of the light," which hints at the presence of two mechanisms, one to pull the particle in and one to push the particle upwards.

Optical tweezers use tightly focussed light to trap and move particles [4]. Developed by Ashkin in 1986, and originally termed as a "gradient force optical trap," optical tweezers represented a significant development in optical trapping [5]. The key feature of this technique is the focusing of the beam, which makes use of the propensity of light to pull high refractive index objects into high intensity regions. This force is called the gradient force and can be considered from two different view points [6]. For particles much larger than the wavelength of light, it is sufficient to consider a ray optical approach, see Fig. 1.2. A dielectric sphere of higher refractive index than the surrounding medium is illuminated by a focused laser beam. If the particle was displaced downwards from the beam focus, as in Fig. 1.2 b), the refracted beam deflected by the particle is now more diverging. The upward component of the deflected beam's momentum is therefore reduced, while all transverse components remain unchanged. In order to conserve momentum, the particle must move upwards, i.e., the particle gains the momentum that the light has lost, and moves towards the beam focus. That the sphere moves back towards the focus is also true if the sphere is displaced up from the focus, or laterally, Fig. 1.2 c).

Figure 1.2 only shows the refracted rays, however there are also reflected rays. These rays also change their momentum when interacting with the sphere, and have the effect of pushing the sphere in the direction the light is propagating. This force is called the

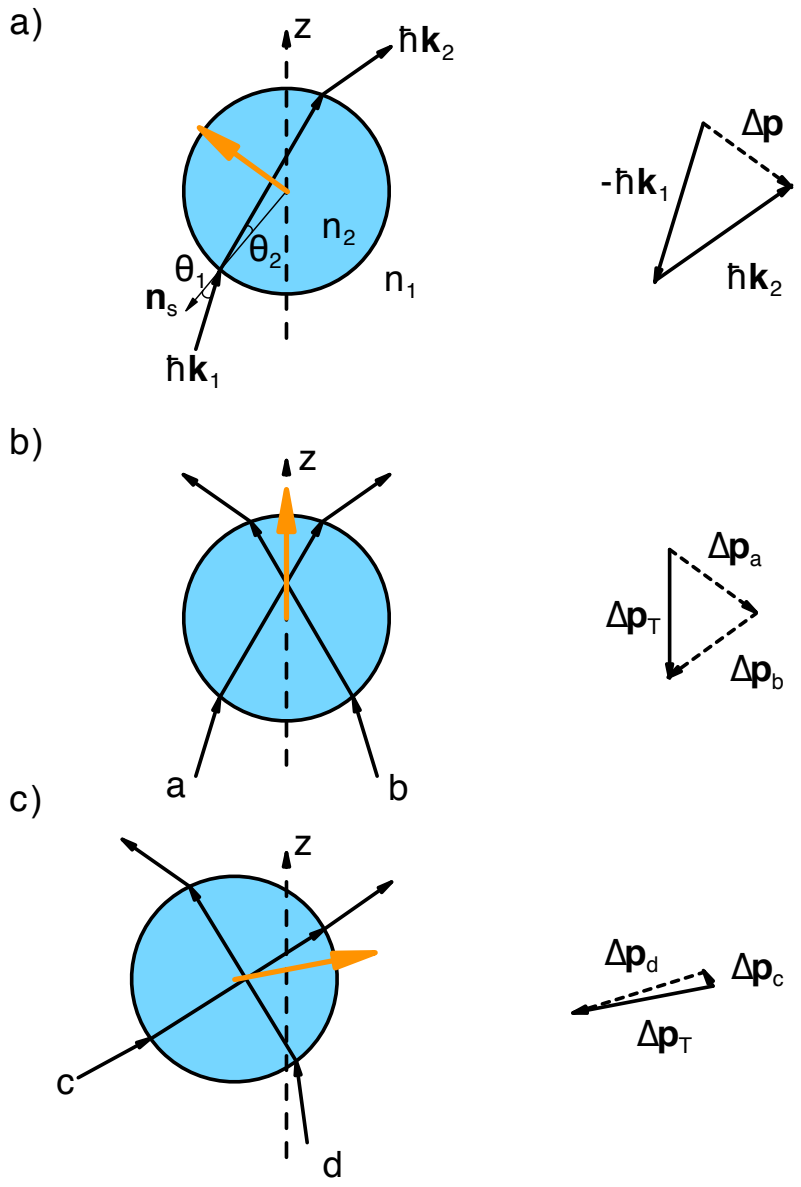

Figure 1.2: Understanding optical trapping from a ray optical perspective. a) shows a single ray of light with momentum $\hbar\mathbf{k}_1$ per photon that is incident on a dielelctric sphere at an angle θ_1 from the surface normal, $\mathbf{n}_s$. If the refractive index inside the sphere (n_2) is greater than the refractive index outside the sphere (n_1), the rays direction will refract towards the normal at θ_2. Upon exiting the sphere, the ray changes direction again, this time refracting away the surface normal. The change in momentum of the light is calculated in the right column. In order to conserve momentum, an equal and opposite reaction force acts on the sphere (shown in with an orange arrow). In b) and c), pairs of rays are used. The total momentum change, $\Delta\mathbf{p_T}$, is the sum of the change in momentum for each ray. For both b) and c), the direction of the reaction force is towards a equilibrium position where the momentum change to the light ray is zero. Reflected rays (omitted for clarity) mean the equilibrium is at a larger z than would be otherwise.

scattering force and means the trap centre is located slightly above the focus of the laser beam.

If the particle is much smaller than the wavelength of light, then the ray optics picture cannot be used. Instead, the particle is considered to have a dipole induced by the electromagnetic field of the light. A dipole in an electric field gradient - as is present in a focused laser beam - feels a force towards the highest intensity of electric field, or towards the beam focus [7]. In optical tweezers, the size of the particles tend to lie between the two models [8].

It should be noted that optical tweezers are not the only occurrence of a gradient force in physics. Another example is the so-called Coandă effect, whereby a fluid flow entrains the surrounding fluid. Fig 1.3. Here, there is a gradient of the fluid flux. If there was an object near the flow, entrainment is prevented and the effect is the deflection of the flow around the object. The deflection causes a change in momentum of the fluid flow, which must be conserved, and, as in optical tweezers, the object moves towards the high intensity. This makes a popular demonstration in science museums, as well as being the mechanism that was used in a now abandoned military project to build a hover vehicle, known as the Avrocar [9].

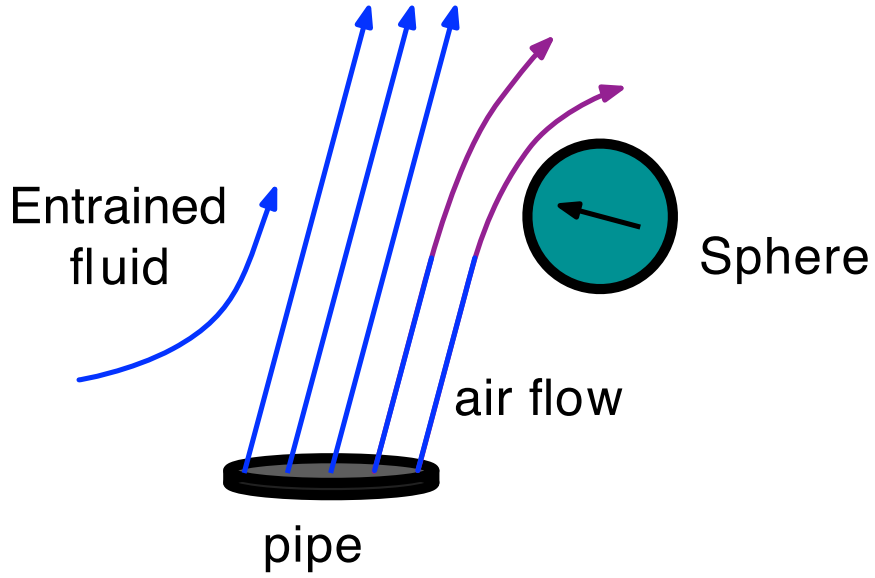

Figure 1.3: A sphere is near a flow of air. The air flow is pulled towards to sphere, meaning there is a reaction force on the sphere into the flow. In the steady state case, the sphere's weight is balanced by the impacts of air molecules off the sphere's surface.

In optical tweezers, for small displacements from the equilibrium position, the restoring force on the particle is linear, i.e., the trap is like a Hookean spring, with a trap stiffness κ. Displacements from the trap centre occur naturally due to the noisy Brownian fluid in which optical tweezers' experiments usually take place. The small size of the particles

used means that Brownian fluctuations are sufficient to agitate the particle. However, the fluid has the benefit of damping any fluctuations so that the particle does not resonate inside the trap. The damping arises from a systematic slowing down of moving objects in a fluid - as an object moves forwards, it is more likely to collide with molecules in the fluid on its front surface than its rear. This is the origin of viscosity, which has the symbol, η.

1.1 The position autocorrelation function

A data analysis tool in optical tweezers is the Position Autocorrelation Function (PAF). This function measures how similar a bead's position is to itself at a later time. The bead's position is limited to being inside the optical trap, so we assume a parabolic potential for all displacements from the trap centre. Qualitatively, after short times, the bead is likely to be in similar positions (i.e., the bead is probably where it was), whereas, after long times, the bead's positional probability reflects the potential (i.e., the bead is probably at the bottom of the potential well). How the bead's position goes from correlated to uncorrelated in described by the PAF and provides useful insights into the properties of the surrounding fluid. It is calculated from experimental data as,

$$A_x(\tau) = \langle x(t)x(t+\tau)\rangle \tag{1.2}$$

where $A_x(\tau)$ is the PAF and $x(t)$ is the experimentally obtained position data. The angle brackets are an average over all start times, t, and τ is the lag time. In this section, the autocorrelation function of a bead in a viscous fluid, held in a harmonic optical potential is derived. I shall show this by first deriving the power spectrum for the bead in a trap, from which the autocorrelation can be obtained by the Wiener-Khinchin Theorem [10].

The power spectrum is given by the modulus squared of the Fourier transform of the sphere's trajectory. The governing equation for the position, $x(t)$, of the bead in the Langevin equation, given as:

$$m\frac{\delta^2 x(t)}{\delta t^2} + \gamma\frac{\delta x(t)}{\delta t} + \kappa x(t) = \xi(t) \tag{1.3}$$

where m is the particle's mass, $x(t)$ is the particle's trajectory, $\gamma = 6\pi\eta a$ (a is the particle's radius) is the Stokes' drag coefficient for a sphere and $\xi(t)$ is the noise term, driving the Brownian motion. To get the power spectrum, we first compute the Fourier transform of Eq. 1.3. For this, the following result is required:

$$\frac{\delta\tilde{x}(\omega)}{\delta t} = \frac{\delta}{\delta t}\int_{-\infty}^{\infty} x(t)e^{i\omega t}dt = i\omega\tilde{x}(\omega), \tag{1.4}$$

where $\tilde{x}(\omega)$ is the Fourier transform of $x(t)$. The Fourier transform of Equation 1.3 is then given by,

$$-m\omega^2\tilde{x}(\omega) + i\omega\gamma\tilde{x}(\omega) + \kappa\tilde{x}(\omega) = \tilde{\xi}(\omega), \tag{1.5}$$

$$\implies \tilde{x}(\omega) = \frac{\tilde{\xi}(\omega)}{-m\omega^2 + i\omega\gamma + \kappa}. \tag{1.6}$$

The power spectrum, $S_x(\omega) = \tilde{x}(\omega)\tilde{x}^*(\omega)$, is found by multiplying both sides of Eq. 1.6 by the complex conjugate,

$$S_x(\omega) = \frac{S_\xi(\omega)}{m^2\omega^4 + \gamma^2\omega^2 - 2m\kappa\omega^2 + \kappa^2}, \tag{1.7}$$

where $S_\xi(\omega)$ is the power spectrum of the noise. Figure 1.4 shows the functional form of Eq. 1.7. From this it can be seen that increasing the size of the particle, and therefore its mass, means the inertia term, $m^2\omega^4$, plays an increasingly important role at lower frequencies. For example, a 10 μm particle is influenced by inertia at around 100 kHz, while a 2 μm particle is diffusive up to 1 MHz. For all experiments in this thesis, the inertial motion is outside the accessible frequency range and therefore is neglected. Also, the $2m\kappa\omega^2$ term can be ignored as is this is much smaller than $\gamma^2\omega^2$. The equation for the power spectrum then becomes,

$$S_x(\omega) = \frac{S_\xi(\omega)/\gamma^2}{\omega^2 + \omega_0^2}. \tag{1.8}$$

Equation 1.8 is a Lorentzian function, where $\omega_0 = \kappa/\gamma$ is the corner frequency marking the transition from trapped to diffusive motion. It is known that $S_\xi(\omega)$ is spectrally flat, i.e., it is white noise, having a constant value for all experimentally accessible frequencies [11]. To find its value, the strategy is to first find the sphere's response to a impulse force, from which the power spectrum of the sphere's velocity can be found while it is experiencing a randomly fluctuating force. The area under the velocity power spectrum is equal the variance of the velocity distribution, which is then related to the thermal energy using the equipartition theorem. First, however, the Langevin equation for a freely diffusing sphere needs to be solved. In the absence of thermal noise,

$$m\frac{\delta^2 x(t)}{\delta t^2} + \gamma\frac{\delta x(t)}{\delta t} = 0. \tag{1.9}$$

This says that the deceleration of the sphere is proportional to the velocity of the sphere. Using a trial solution of $x(t) = x_0 e^{\alpha t}$ gives,

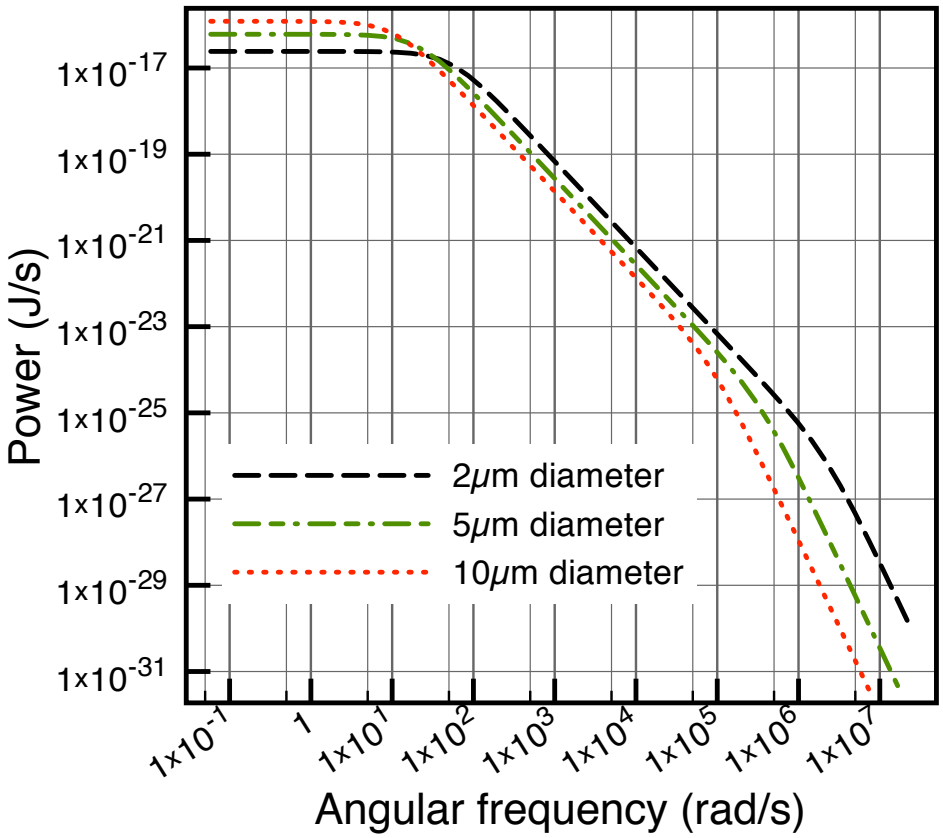

Figure 1.4: Theoretical power spectrums for the motion of various spheres in an optical trap of trap stiffness $\kappa = 1\,\mu\mathrm{Nm}^{-1}$. The low frequency is dominated by the trap and is therefore flat. The intermediate region, between around 10 rad/s and 100 rad/s, is diffusive motion and has a slope of -2. The high frequency is inertial motion which has a slope of -4. The larger the sphere, the sooner the inertia becomes important.

$$\alpha^2 m x(t) + \gamma\alpha x(t) = 0, \tag{1.10}$$

$$\alpha^2 m + \gamma\alpha = 0, \tag{1.11}$$

$$\implies \alpha = -\frac{\gamma}{m}. \tag{1.12}$$

Thus, $x(t) = x_0 e^{-\frac{\gamma}{m}t}$. As the mass is tiny, any motion of the sphere will be exponentially damped. The speed of the damping depends, as may be expected, on the mass and Stokes' drag coefficient of the sphere. Of particular interest is the response to a delta function force as this gives the Green's function, $G(t)$, which can be convolved with any driving force to obtain the trajectory of the sphere. The momentum of the sphere just after the force $f(t)$ (at $t = t'$) is,

$$p = m\left.\frac{\delta x(t)}{\delta t}\right|_{t=t'} = \int_{-\infty}^{t'} f(t)dt = \int_{-\infty}^{t'} \delta(0)dt = 1, \tag{1.13}$$

$$\implies \left.\frac{\delta x(t)}{\delta t}\right|_{t=t'} = -\frac{\gamma}{m} x_0 e^{-\frac{\gamma}{m}t'} = \frac{1}{m}, \tag{1.14}$$

$$\implies x_0 = -\frac{1}{\gamma}. \tag{1.15}$$

So, the Green's function and its time derivative are, respectively,

$$G(t) = -\frac{1}{\gamma} e^{-\frac{\gamma}{m}t}, \text{ and,} \tag{1.16}$$

$$\dot{G}(t) = \frac{1}{m} e^{-\frac{\gamma}{m}t}. \tag{1.17}$$

Given the driving Brownian force, $\xi(t)$, the velocity of the particle is given by the convolution of $\xi(t)$ and $\dot{G}(t)$, from which the velocity power spectrum is calculated:

$$\frac{\delta x(t)}{\delta t} = \xi(t) * \dot{G}(t), \tag{1.18}$$

$$\frac{\delta \tilde{x}(\omega)}{\delta t} = FT(\xi(t) * \dot{G}(t)), \tag{1.19}$$

$$= \tilde{\xi}(\omega)\tilde{\dot{G}}(\omega), \tag{1.20}$$

$$S_{\dot{x}}(\omega) = S_\xi(\omega)\tilde{\dot{G}}(\omega)\tilde{\dot{G}}^*(\omega). \tag{1.21}$$

where $S_{\dot{x}}(\omega)$ is the velocity power spectrum and $S_\xi(\omega)$ is the power spectrum of the noise.

$\tilde{\dot{G}}(\omega)$ is computed as:

$$\tilde{\dot{G}}(\omega) = \mathrm{FT}\left(\frac{1}{m}e^{-\frac{\gamma}{m}t}\right), \tag{1.22}$$

$$= \frac{1}{m(\frac{\gamma}{m} + i\omega)}, \tag{1.23}$$

$$= \frac{1}{\gamma + im\omega}, \tag{1.24}$$

$$\implies S_{\dot{x}}(\omega) = S_{\xi}(\omega)\frac{1}{\gamma^2 + m^2\omega^2}. \tag{1.25}$$

Equation 1.23 relies on the fact that $\dot{G}(t)$ is a single sided exponential (i.e., for $t < 0, \dot{G}(t) = 0$). From the definition of a power spectrum, the area under the power spectrum of a signal is equal to the variance of the signal in the time domain, i.e., in this instance,

$$\int_{-\infty}^{\infty} S_{\dot{x}}(\omega)d\omega = \left\langle \left(\frac{\delta x(t)}{\delta t}\right)^2 \right\rangle = \frac{k_B T}{m}, \tag{1.26}$$

where the angle brackets indicate the time average, T is the temperature and k_B is Boltzmans constant. The value of the velocity variance has been found through the equipartition of energy. By integrating Eq. 1.25, and substituting in Eq. 1.26, the following is obtained:

$$\frac{k_B T}{m} = S_{\xi}(\omega)\int_{-\infty}^{\infty}\frac{1}{\gamma^2 + m^2\omega^2}d\omega. \tag{1.27}$$

As previously noted, $S_{\xi}(\omega)$ is assumed to be spectrally flat and therefore is just a constant for the integration. Rearranging Eq. 1.27 gives an expression for the power spectrum of the thermal fluctuations,

$$S_{\xi}(\omega) = \frac{k_B T}{m} \Big/ \int_{-\infty}^{\infty}\frac{1}{\gamma^2 + m^2\omega^2}d\omega, \tag{1.28}$$

$$= \frac{k_B T}{m} \Big/ \frac{1}{m^2}\left[\frac{m}{\gamma}\tan^{-1}\left(\frac{m\omega}{a}\right)\right]_{-\infty}^{\infty}, \tag{1.29}$$

$$= \frac{k_B T\gamma}{\pi}. \tag{1.30}$$

Equation 1.8 can now be rewritten as,

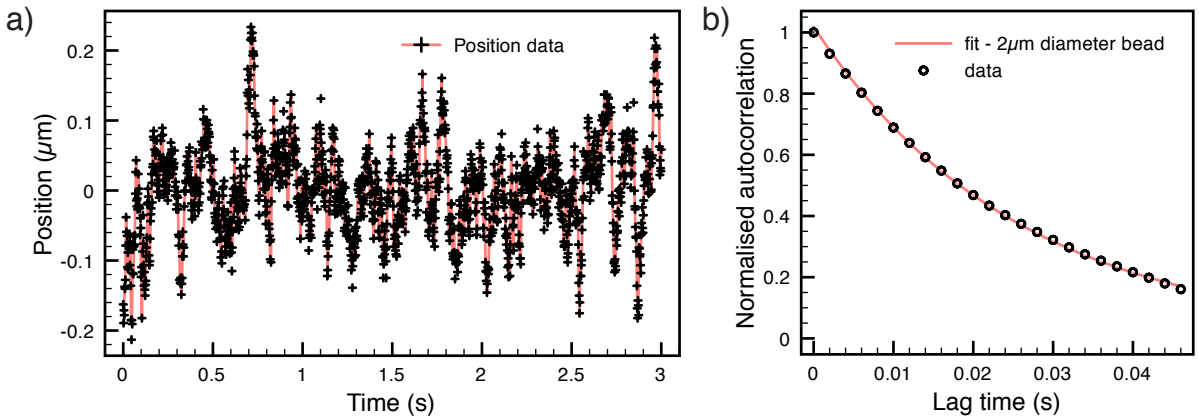

Figure 1.5: a) A three second section of the position trace of a 2 μm particle held in optical tweezers. The particle is seen to fluctuate due to Brownian motion. b) The normalised autocorrelation function, as calculated from 40 s of data.

$$S_x(\omega) = \frac{k_B T}{\pi\gamma} \frac{1}{\omega^2 + \omega_0^2}. \tag{1.31}$$

The Wiener-Khinchin theorem states that the Fourier transform of the autocorrelation is equal to the power spectrum. So, to obtain the position autocorrelation function (PAF), the inverse transform of Eq. 1.31 must be performed. The Fourier transform of a Lorentzian is a (double sided) exponential decay so we have,

$$A_x(\tau) = \mathrm{FT}^{-1}\left(\frac{k_B T}{\pi\gamma} \frac{1}{\omega^2 + \omega_0^2}\right), \tag{1.32}$$

$$= \frac{k_B T}{\kappa} e^{-\omega_0 \tau}. \tag{1.33}$$

Typically, the PAF is divided by the variance of the sphere's trajectory to obtain the normalised position autocorrelation function (NPAF), Fig 1.5,

$$A_x(\tau) = e^{-\omega_0 \tau}. \tag{1.34}$$

The variance is found by applying the equipartition theorem to the energy stored in the trap [12],

$$\frac{1}{2} k_B T = \frac{1}{2} \kappa \langle x^2 \rangle \tag{1.35}$$

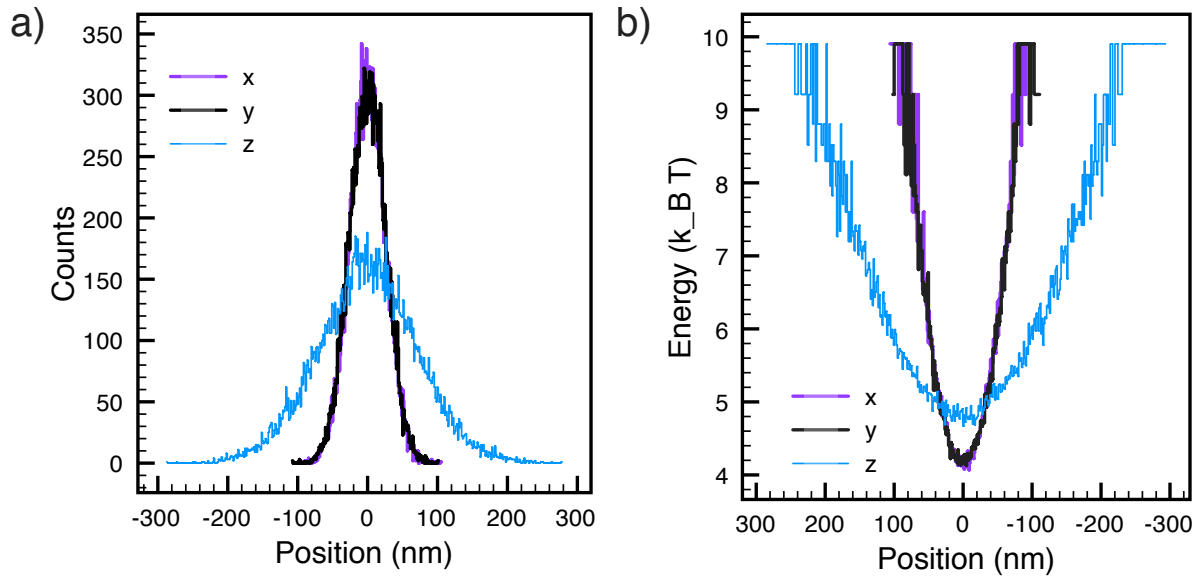

Figure 1.6: a) Position histograms using the same data as Fig. 1.5 for x (purple), y (black) and z (blue). The variance of these plots is related to the trap stiffness. For this experiment the trap stiffness in z is $\kappa_z = 1.6\,\mu\mathrm{Nm}^{-1}$, which is about 4 times less than the stiffness in x and y. b) The corresponding energy potential. That these are parabolic implies that the restoring force is linear.

Therefore, the measurement of the variance of a trapped particle easily gives the trap stiffness, κ. This means that $\gamma = \kappa/\omega_0$, which contains information on interesting and useful parameters like particle size and fluid viscosity, is readily accessible from the auto-correlation function of a trapped particle's trajectory.

The calibration against the equipartition of energy relies on there being a linear restoring force acting to move the trapped particle back towards the trap equilibrium. For a typical optical tweezer, this is the case even for quite large displacements, i.e., the potential in which the particle sits is quadratic. For more elaborate systems, the calibration method is only valid for small displacements [13]. Measurement of the underlying potential is possible by accumulating a histogram of the particle's position, Fig. 1.6 a). The histogram for a single optical trap is a Gaussian distribution, where the skewness, kurtosis and higher order terms are close to zero for a well aligned system. By normalising the histogram, the position probability distribution, $\rho(x, y, z)$, of the particle position is obtained. This is related to the energy potential, $U(x, y, z)$, by,

$$\rho(x, y, z) = \exp[-U(x, y, z)/k_B T]. \tag{1.36}$$

The potential is shown in Fig. 1.6 b). This method is general and can be used to find the potential of any configuration of optical field, so long as the particle has sufficient thermal

energy to explore the regions of interest and assuming a conservative force field [14].

1.2 Optical tweezers: set up

One appeal of optical tweezers is the reasonable simplicity of the required optical system. One needs to focus the trapping laser to create a high field gradient and to view the trapped object with a sufficient magnification to observe the sample. Both of these requirements are satisfied using a high-magnification optical microscope. High magnification objectives have large collection angles, quantified by the Numerical Aperture, ($\mathrm{NA} = \mathrm{n}\sin\theta$, where n is the refractive index of the medium between objective and sample and θ is half the collection angle). To obtain a large NA, oil immersion objectives are used which have $\mathrm{n} \approx 1.5$, giving modern high power objectives NAs of up to 1.4. In addition to the imaging optics it is usually straight forward to incorporate a beam splitter into the optical path, inserted between the infinity corrected objective lens and the microscope tube lens. A collimated laser beam introduced at this point is brought to a tight focus in the focal plane of the sample, creating an optical trap into which any nearby dielectric particle of higher refractive index than the surrounding fluid will be attracted. The size, d, of the focus is given by,

$$d = \frac{1.22\lambda}{\mathrm{NA}}, \tag{1.37}$$

where λ is the wavelength of the trapping laser. The smaller the focal spot, the greater the gradient force. It is interesting to note that if the particle has a lower refractive index than the surrounding fluid, then the optical forces act to repeal it away from the beam focus.

Trapping a micron-sized object in a microscope is a beautiful demonstration of optical momentum, but it is also possible to manipulate the object. Shifting the optical trap in a lateral direction requires a change in angle of the light going into the objective lens. Most simply, this can be achieved using a beam steering mirror that is telescopically imaged onto the back focal plane of the objective lens. Automating this mirror, or other angular beam steering technology, gives the basis of a user interface. Creating two traps with the same microscope can be achieved by introducing a second laser, or two beam splitters and an additional mirror, but three or more traps would become complicated. Rather than use separate optical paths, early tweezers systems followed a time-shared approach where a rapid switching of the beam direction allows each trap to be created in turn. Providing that the return interval of the laser to the same trap is less than the diffusion time ($\backsim \omega_0^{-1}$) of the particle then multiple traps can be sustained. This does affect the

stiffness of the trap which is proportional to the average laser power for the trap.

Ten years after the invention of optical tweezers, a number of groups began exploring alternative approaches based on diffractive optics. Consider the case of the beam steering mirror being replaced by a diffraction grating. Each of the diffraction orders has a different diffraction angle, thereby producing a linear array of optical traps in the sample plane. Alternative grating designs can be calculated to give different configurations of traps. The diffractive optic is in the far-field of the trapping plane and hence these calculated optics are often called "holograms."

Diffraction gratings can either modulate the phase or the amplitude (or both) of light incident upon them. Rather than using a pre-fabricated diffractive optic, the development of programmable Spatial Light Modulators (SLMs) gives an interactive alternative. SLMs are pixellated liquid crystal devices where each pixel can introduce a phase change to the incident light between 0 and 2π. The SLMs are typically addressed using the video port output from a computer and allow rapid (up to 1 kHz [15]) switching between diffractive patterns and hence configuration of optical traps. The computer control of the SLM also lends itself to the development of sophisticated interfaces where the multi-trap capability is reflected in the interface itself.

The relationship between the calculated diffraction pattern and the configuration of traps is a spatial 2D Fourier transform. However, calculation of simple patterns can be performed more quickly. If all that is required is a single optical trap, the required pattern is simply that of a diffraction grating, blazed to concentrate over 95% the diffracted light in the first order. To move the trap in the x direction requires a vertically striped grating, where the closer together the stripes are, the further the trap is displaced from the zero order. To move the trap in y, horizontal stripes are required. To move a trap diagonally, the diffraction grating is the mod(2π) addition of an x and y grating,

$$\phi_{grating}(u, v) = \mathrm{mod}(2\pi)(\alpha u + \beta v), \tag{1.38}$$

where $\phi(u, v)$ is the phase pattern displayed on the SLM (u and v are the horizontal and vertical coordinates of the SLM), and α and β are constants determining the period of the grating. Unlike a simple mirror, an SLM can also be encoded with circular lines, acting as a Fresnel lens to change the wavefront curvature of the laser at the objective lens and shift the trap in an axial direction,

$$\phi_{lens}(u, v) = \mathrm{mod}(2\pi)\left(-\frac{k}{2f}(u^2 + v^2)\right). \tag{1.39}$$

Thus, unlike a mirror, using an SLM programmed with a suitable hologram gives 3D control of trap position where the combined lens and grating phase pattern is given

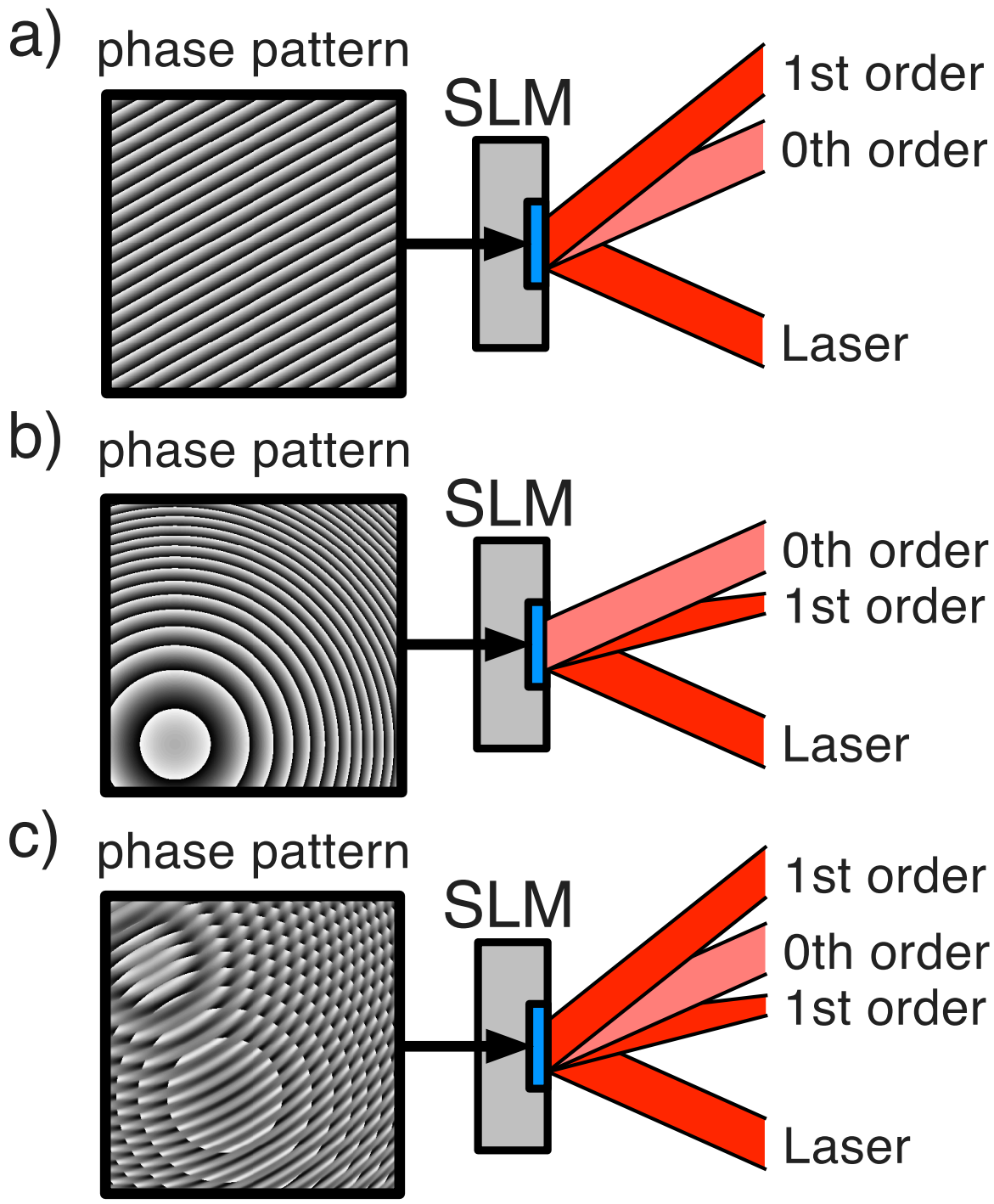

Figure 1.7: a) shows a representation of a blazed grating being displayed on a Spatial Light Modulators (SLM) (black to white represents phase levels $0 - 2\pi$). The laser is incident on the SLM from below and some of the light is reflected directly, into the 0^{th} order, but most is deflected away into the 1^{st} order. In b), a grating is combined with a lens to focus the diffracted 1^{st} order. c) shows the generation of two 1^{st} order beams by the complex addition of these two phase patterns.

by the mod(2π) addition of $\phi_{grating}(u,v)$ and $\phi_{lens}(u,v)$. For multiple traps one could switch rapidly between holograms, however, two or more holograms can be combined into a single design [16]. Combining holograms in this way requires pixel by pixel addition, where each pixel is treated as a complex number (with magnitude, $A_n(u,v)$, corresponding to the relative trap strength and argument equal to the phase of the individual hologram, $\phi_n(u,v)$),

$$\phi_{multi}(u,v) = \arg\left(\sum_{n=1}^{N} A_n(u,v)e^{i\phi_n(u,v)}\right), \tag{1.40}$$

i.e., the required phase of each pixel in the composite hologram, $\phi_{multi}(u,v)$, is the argument of the complex sum of the individual holograms. Thus the design of the holograms required to produce arbitrary configurations of optical traps requires nothing more than the addition of complex arrays of numbers (Fig. 1.7), a task ideally suited to the use of graphics card processors, which can be connected directly to the SLM. Even consumer-grade components can calculate and display the required holograms at video frame rates. The use of spatial light modulators for optical trapping is referred to as "holographic optical tweezers" [17]. A schematic of such a system is shown in Fig. 1.8.

1.3 Optical tweezers: applications

Since their inception, optical tweezers have been used across disciplines in a host of different experiments. In particular the fields of biology, microhydrodynamics and physics have witnessed the benefits of the nanometer positioning and picoNewton force measurement.

In biology [18], perhaps the greatest achievement of optical tweezers to date has been the discovery that biological motors, such as kinesin, move along a protein by taking physical steps. Experimentalists found that by tethering an optically trapped, micron sized bead to the kinesin molecule, the tiny steps could be detected from slight position stepping of the trapped bead. Another biophysical application of optical tweezers involved studying force interactions between T-cells [19]. Optical tweezers have also shown promise in the field of high resolution imaging of delicate biological structures. Here, a particle is held with optical tweezers and translated to the surface. By measuring the position of the particle relative to the trap centre, it is possible to determine where the motion is influenced by the presence of the surface. By mapping out these locations, it is possible to map out the 3D structure of cell walls. This technique, termed photonic force microscopy [20], or optical atomic force microscopy, relies heavily on the shape of the particle (or probe) used, where trapping handles and a sharp tip improve the imaging

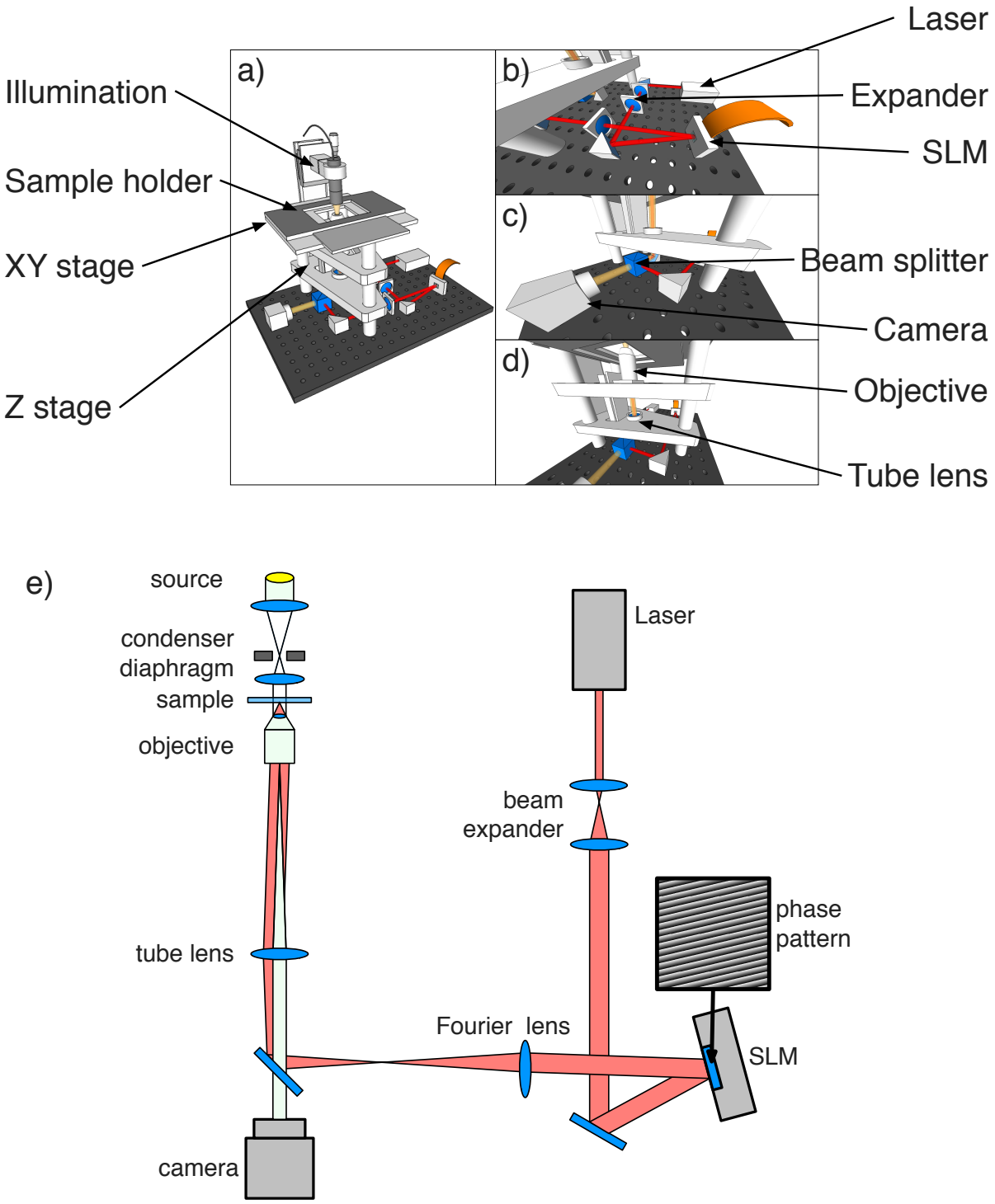

Figure 1.8: A 3D model of an example holographic optical tweezers system. a) shows the inverted microscope structure with positioning stages, sample holder and illumination. b) shows a close up of the laser, beam expander and Spatial Light Modulator (SLM). c) shows details of the the laser being incorporated into the imaging of the microscope via a beam splitter. A fold mirror deflects the beam upwards from underneath the microscope. d) shows the microscope tube lens and objective lens, used to focus the laser and create the optical traps, as well as image the sample. e) shows a two dimensional diagram of the setup.

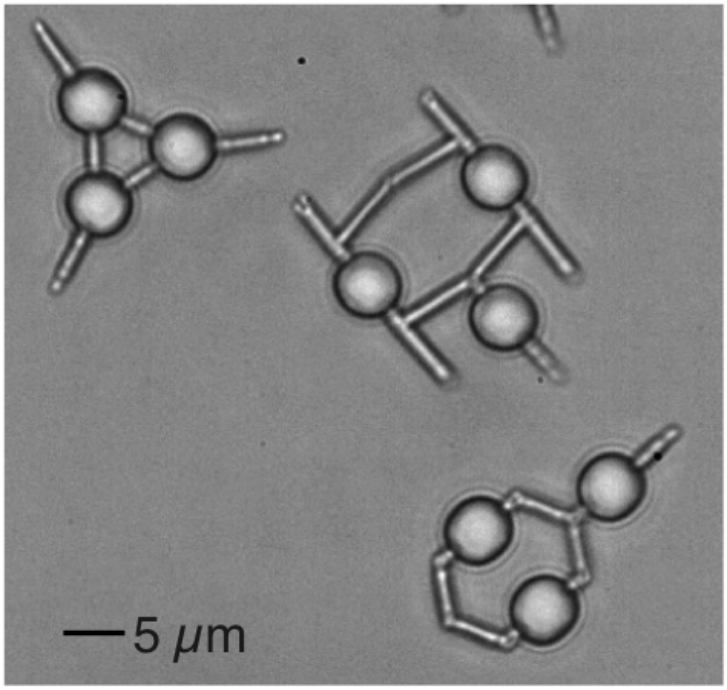

Figure 1.9: Various nanofabricated two photon polymerised probes. The trapping spheres also act as isolated tracking handles due to their symmetry. The tip can be as sharp as 200 nm. Image courtesy of Dr. David Phillips.

speed (as the probe can be more stably trapped) and resolution (as the particle interacts with a smaller portion of the structure). Both of these requirements have been met with certain diatoms [21] (an algae, which, as fortune has it, is naturally probe-shaped) and, more recently, nanofabricated two photon polymerised probes [22, 23, 24] (Fig. 1.9).

Linking biology to mechanical principles has been a major challenge for many years. Owing to the richness of biology, and the complexity of Brownian dynamics (in terms of number of interactions), optical tweezers have played a role mimicking biological features in simplified experimental configurations. For example, the probability that a particle, or molecule, will jump over an energy barrier, given a certain amount of thermal energy had been theoretically predicted by Kramers in 1940 [25], but not experimentally demonstrated until 1999, through the use of optical tweezers [26]. Here, the experiment involved two optical traps positioned close to each other so that a particle could be stably trapped in either, yet there existed a small probability that the particle could jump from one trap to the other. The probability of a transition could be determined directly from the transition rate of the particle between the traps, and agreed with the predicted probability given by the underlying energy potential.

Following on from this work, researchers explored the possibility of changing this probability through cooperative motion of more than one particle [27, 28]. Kotar et al. [29]

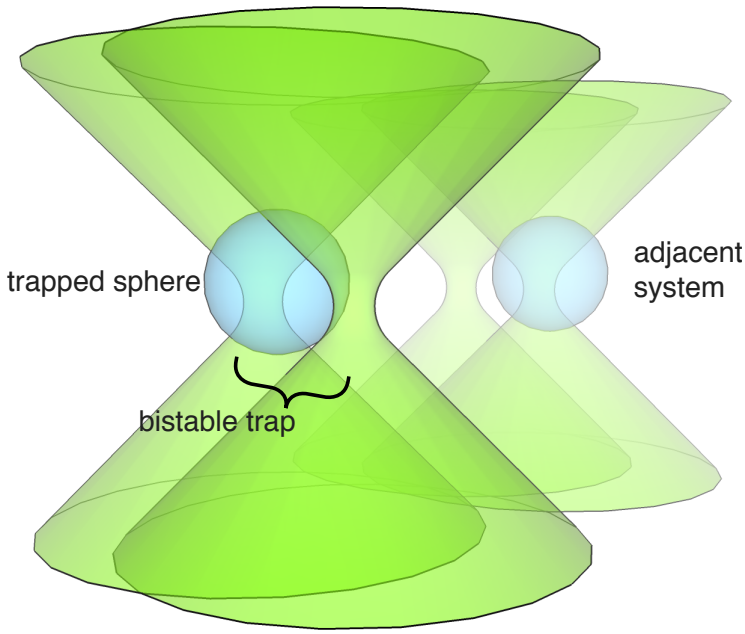

Figure 1.10: An optical tweezer experiment used measure hydrodynamic interactions. Two bistable traps are positioned adjacent to one another, each with a single trapped sphere. If one sphere transitions across the bistable trap, there is an increased probability that the neighbouring sphere will do likewise.

used two sets of switching optical traps, with each set containing one particle. Each particle was able to diffuse with its trap, but triggered a switch of the trap position if it moved near to one edge of the trap, inducing a random oscillation on top of the diffusive motion. As the particles oscillated, an entrained flow influenced the neighbouring particle. This simple set up achieved synchronisation of the two oscillators, and provided an intriguing mechanism by which biological functions might operate. Other synchronisation experiments have been performed, including rotation of optical "light mills" and circulating spheres [30]. The synchronisation relies on there being some sort of external driving force, such as the switching of the position of the traps, or the torque applied to an object. However, in the case of no driving force, synchronisation still was observed, not in the position of the particles, but in their displacements, Fig. 1.10. Experimental evidence of this result is given Chapter 3 of this thesis.

The fluid which gives rise to the hydrodynamic synchronisations is often of interest in its own right [31]. The field of microrheology concerns the study fluid of flows on a micron scale and in microlitre volumes. Such scales are important for biological fluids where small volumes may be all that is available, and microfluidic devices [32] where the small scales lead to a vast increase in the number of reactions that can be performed per minute [33]. Of high importance to biophysists is the viscoelastic properties of the fluid. Optical tweezers provide a procedure to access the viscoelasticity at these crucial

small scales [34]. In the simplest configuration, all that is required is position tracking of a micro-sphere trapped in the fluid. In principle, even the optical trap is not required and particle tracking of a freely diffusing sphere can give measurement of these properties, however Brownian motion means the sphere is likely to diffuse out of the trackable volume. Optical tweezers hold the particle in place meaning that small tracking regions can be used. Particle tracking (in this thesis) has been performed with high speed CMOS cameras which, with an appropriate Region Of Interest (ROI), can record particle positions at over kHz rates. Another tracking technology involves looking at the scattered laser light on a Quadrant PhotoDiode (QPD). This is much faster (MHz rates), although somewhat lacks the flexibility of camera technology, especially for multiple particles. [35, 36].

From an engineering point of view, the behaviour of a fluid at different time scales, or frequencies, is the important quantity [37, 38]. For instance, imagine a sphere held in an optical trap in a viscous fluid. The optical trap is now sinusoidally oscillated, side to side at a particular frequency, ω. The sphere experiences two forces: an oscillatory force from the trap, and the random stochastic forces of Brownian motion. By averaging over many oscillations, the Brownian forces will average out, leaving only the oscillatory force. For a purely viscous fluid, the sphere's trajectory will lag behind the trap position by a phase of $\pi/2$. The amplitude of the sphere's oscillation gives the viscosity of the fluid at *one* frequency, namely the frequency that the trap is being driven at. However, it is possible, due to optical tweezers, to obtain the viscosity of the fluid at *all* (experimentally accessible) frequencies [39]. Frequency dependant fluid properties are described by the complex modulus, $G^*(\omega)$, given by,

$$G^*(\omega) = \frac{\kappa}{6\pi a}\left(\frac{1}{i\omega\tilde{A}_x(\omega)} - 1\right)^{-1} \tag{1.41}$$

where $\tilde{A}_x(\omega)$ is the Fourier transform of the normalised autocorrelation function (here, the autocorrelation is single sided). $G^*(\omega)$ contains both real and imaginary parts, which correspond to the elastic and viscous properties of the fluid, respectively, and can be plotted separately. For optical tweezers, the real (elastic) part is influenced by the trap, giving a constant response across all frequencies. The imaginary part gives the viscosity. A Newtonian fluid (such as water) has a constant viscosity for all frequencies. Other fluids (e.g., paint) have a frequency dependant viscosity. Complex fluids are those with both a elastic and viscous parts (e.g., oil, saliva). Broadly speaking, however, all fluids act like solids if observed at extremely high frequencies, and all solids flow like a fluid if observed at extremely low frequencies, corresponding to very long times [40]. It is therefore apparent that the larger the frequency range accessed by the experiment, the more useful the complex modulus becomes. In optical tweezers, high frequencies are

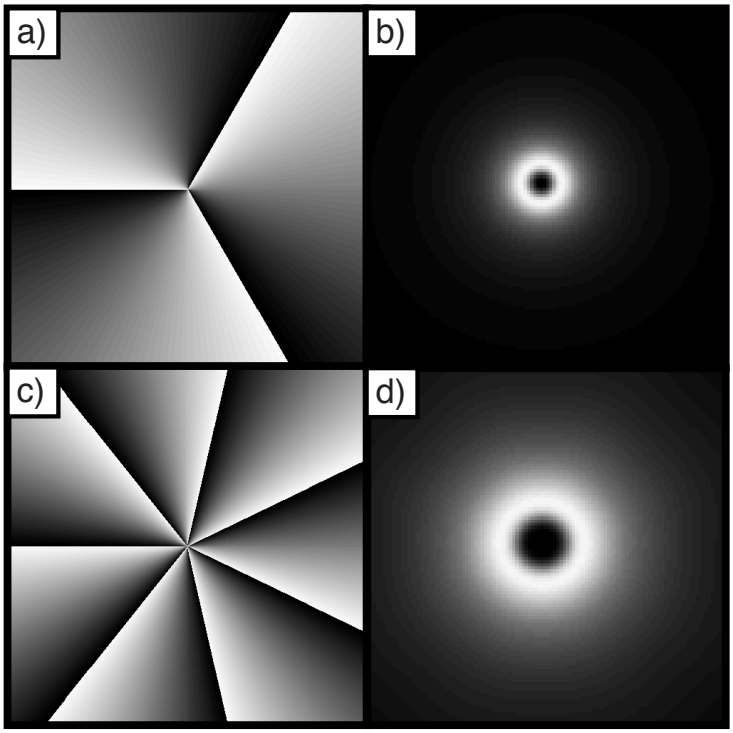

Figure 1.11: Intensity and phase cross sections of beams carrying OAM. a) phase cross section of $\ell = 3$, with white corresponding to 2π, and black corresponding to 0. b) intensity cross section of $\ell = 3$. c) phase cross section of $\ell = -5$. d) intensity cross section of $\ell = -5$.

limited by the acquisition rate of the camera or QPD used. The low frequency limit is given by one over the total length of the the experiment. In some fluids, particularly colloids or biological samples, there is abundant diffusing material which can diffuse into the optical trap alongside the probe sphere [41]. This effectively ends the experiment earlier than may be needed. To mitigate this process, I describe in Chapter 4 an optical procedure to shield the trap from this diffusing debris.

A further application of optical tweezers is the investigation into the fundamental properties of light. As already discussed, the optical trap is a demonstration of the linear momentum of light. However light also has angular momentum. Spin angular momentum is related to the polarisation of the light. Light can either be left or right circularly polarised (or a combination of the two). For pure states (i.e., completely left or right), each photon has $\pm\frac{1}{2}\hbar$ of angular momentum. If circularly polarised light is used to trap a birefringent particle, the particle spins on the beam axis. The particle needs to be birefringent as it effectively is acting like a quarter waveplate, converting the circular polarisation into linear polarisation by introducing a phase shift between the horizontal and vertical components of the circular polarsation. In order to conserve angular momentum, the particle needs to rotate.

In addition to spin angular momentum, light can also have Orbital Angular Momentum (OAM) [42]. OAM in light arises from a helically shaped phase front, i.e., in a cross section of a beam carrying OAM the phase changes by ℓ full cycles around the beam axis (where ℓ is an integer). The orbital angular momentum of the beam is given by $\ell\hbar$. For example, for an $\ell = 1$ beam, the cross sectional phase cycles from $0 - 2\pi$ once around the beam axis. As the beam propagates, the phase front (that is, the surface of all points of the same phase) forms a single helix centred on the beam axis. For an $\ell = 2$ beam, the phase cycles twice from $0 - 2\pi$ around the axis, the phase front is a double helix, and so on. Negative values of ℓ are allowed, and indicate the phase cycling in the opposite direction (e.g. $2\pi - 0$ in the case of $\ell = -1$). The intensity of such beams is that of a dark centre and an annulus of high intensity, Fig. 1.11. The dark centre can be interpreted from the cross-sectional phase pattern - on the beam axis, all phases meet giving destructive interference, and the intensity is zero. When an OAM beam is used in optical tweezers, the trapped particle is drawn into the high intensity annulus whereupon the particle orbits around the beam axis. This relies on the nonconservative scattering force. Effectively, when the trapped sphere is at one angle from the beam axis, the trapping rays are skewed tangentially. Hence, light reflected by the sphere has an preferred tangential direction, which pushes the sphere around the annulus.

An orbital angular momentum carrying probe beam has also been been used to measure the rotation of a macro scale spinning disk, in an angular equivalent to Doppler velocimetry. The disk was illuminated with a superposition of two beams carrying conjugate ℓ values (i.e., one clockwise beam at $+\ell$ and the other anticlockwise at $-\ell$). If the disk rotated clockwise, the $+\ell$ beam was scattered off the disk and increased (blueshifted) in frequency, in a rotational equivalent of the normal Doppler shift. The $-\ell$ beam was correspondingly decreased (redshifted). The two beams together interfere to give a time varying signal, resulting from the sinusoidal beating of two similar frequencies. The frequency of the beat (ω_{beat}) is related to the rotation of the disk (Ω_{rot}) by,

$$\Omega_{rot} = 2\ell\omega_{beat}. \tag{1.42}$$

In Chapter 5, I give results from an equivalent experiment performed on an optical trapped rotating microsphere. As the sphere is close to the diffraction limit of the probe beam, this is an exploration of the fundamental limits of the technique.

1.4 Summary

Optical tweezers are a demonstration of the momentum carried by light. The momentum can either be considered through a wave or particle (photon) description. By tightly focusing a laser beam, the momentum of light can be used to trap micron sized dielectric objects in three dimensions. The motion of such an object can be described by the Langevin equation, which can be used to obtain the position autocorrelation function, characterising the system. Optical tweezers are usually built around an inverted microscope which provides imaging of the microscopic particles, as well as focusing the laser to create the traps. Holographic optical tweezers use a spatial light modulator to efficiently create and position many optical traps making optical tweezers a versatile tool. As such, optical tweezers have been used in biology to measure tiny forces (pN), and map delicate structures. They have been used to mimic biological processes like synchronisation and in the study of complex fluids. Finally, they have been used to explore the interaction of the orbital angular momentum of light with matter.

II
SLM Micrcoscopy

In the previous chapter, I discussed Fourier transforms of time varying signals (for example, the trajectory of a sphere in a optical trap). However, Fourier transforms are also of use in signals that vary in space. In optics, this is important as a lens (as well as free space propagation) performs a Fourier transform. For example, a beam with a Gaussian cross-section, when propagated through a lens, may be focused but remains Gaussian. when a beam with a sinusoidal cross section (in intensity or phase) is propagated through a lens, it becomes two focused beams (Fig. 2.1 (top)), just as a sinusoidal signal corresponds to a positive and negative frequency. In optics, the negative frequency is manifest as a beam travelling in the negative direction, with respect to an origin on the beam axis.

In general, any beam can be Fourier transformed (Fig. 2.1 (middle)). Physically, this transformation relates to the plane wave composition of the beam. Each point in the Fourier transform corresponds to a direction (or angle) that light propagates at from the image plane. In the case of Fig. 2.1 (top) light propagates at two directions from the image, giving two points in the Fourier transform. In Fig. 2.1 (middle), light propagates at a large number of directions, owing to the complexity of the object. The same is true for Fig. 2.1 (bottom), so much so that the finite aperture of the lenses blocks some of these directions, resulting in a cut off in the Fourier transform and limited resolution.

2.1 Microscope image formation

In microscopy, increasing the resolution is an active area of research. In order to achieve high resolution, the number of directions of propagating light collected by the objective lens must be large. This is because small features scatter light at high angles and this scattered light must not be lost in order to image small features. Collecting a lot of angles is primarily achieved by positioning the objective lens close to the sample, Fig. 2.2, however this also leads to aberrations. Objective lenses are therefore composed of many correction lenses in order to compensate for the aberrations. An example is chromatic

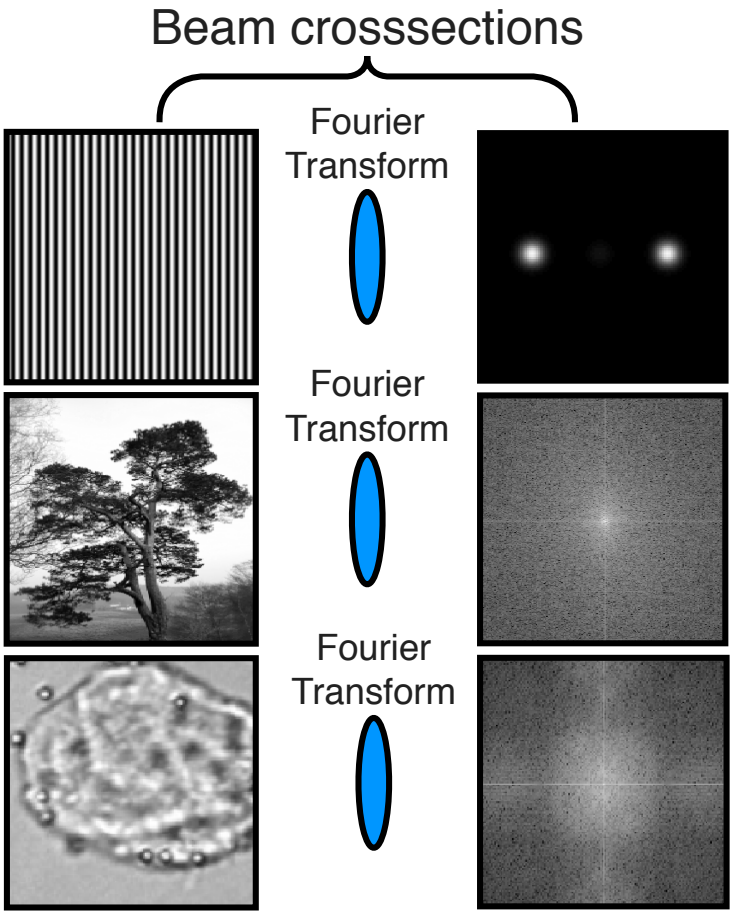

Figure 2.1: Numerical Fourier transforms of different simulated beam cross-sections (each beam is given a uniform phase). The situation is similar to a diffraction grating being placed in a laser beam. Top: a sinusoidal pattern transforms into two focused spots. Middle: a Scots Pine tree has a complicated Fourier spectrum. Bottom: a microscope image and its Fourier transform - note the cut off in the frequency spectrum due to the image being oversampled.

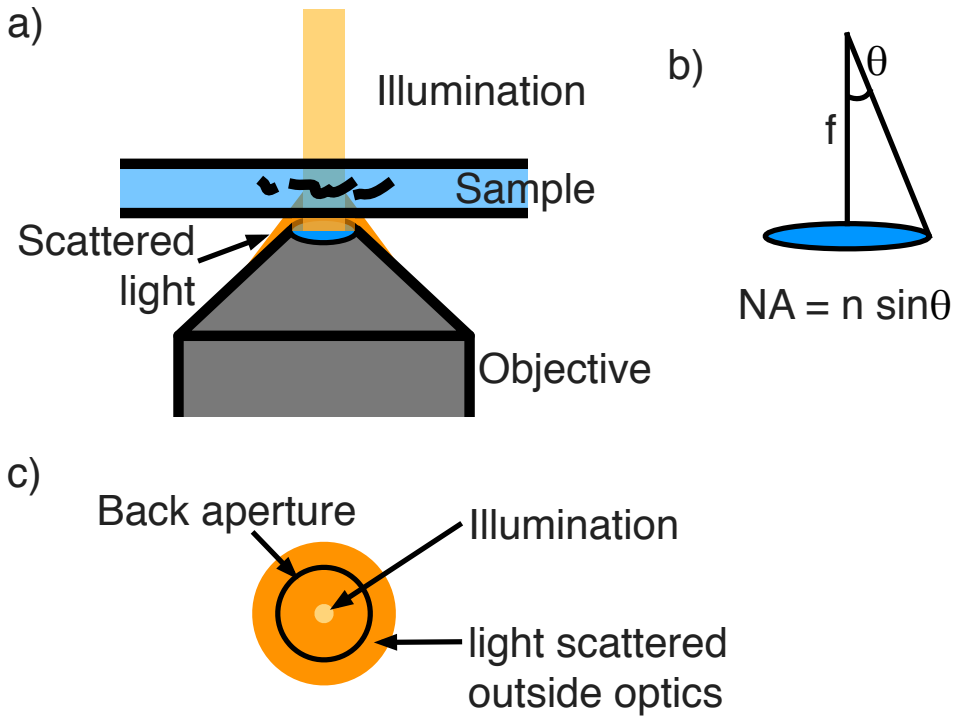

Figure 2.2: a) Schematic of microscope objective lens. A plane wave illuminates a sample (i.e. low NA illumination). The sample scatters the light at various angles. The objective collects as many of these angles as possible by being placed close to the sample. b) The Numerical Aperture (NA) describes the number of angles that an objective can collect (f is the focal length of the lens and n is the refractive index of the medium between the lens and focus). c) The Fourier plane of a microscope image, overlaid with the back aperture of the objective. If the sample is illuminated with a plane wave the back aperture features a bright point in the centre, with the scattered light around this. Light scattered outside the back aperture is not collected by the objective and results in a loss of resolution. Note: the illumination and scattered light are shown in different colours for clarity only.

aberration, where different colours of light are refracted at different angles through a lens and therefore each colour forms an image at different distances. Inside an objective there are combinations of lenses and glasses with different dispersion characteristics which work together to remove chromatic aberrations. Another example is spherical aberration. This is where rays going through the edges of a spherical lens are brought to a focus before the rays going through the centre.

Aberrations lead to a loss of resolution in a different way to the finite aperture, namely that the imaging rays do not all meet at the same point, which leads to blurring of fine details. Both the effect of a finite aperture and aberrations are described by the microscope's Point Spread Function (PSF). Figure 2.3 shows the effect of a finite aperture on the PSF. The PSF can be measured directly by imaging a sub diffraction limit object, but it arises from the circular back aperture of the objective lens. This aperture multiplies

the Fourier transformed light field of the object, blocking high angles. The image is formed by another lens transforming the light back to the image plane. Owing to this Fourier relationship, the image is now convolved with the Fourier transform of the back aperture, as given by the convolution theorem:

$$\mathrm{FT}(\mathrm{A} \times \mathrm{B}) = \mathrm{FT}(\mathrm{A}) * \mathrm{FT}(\mathrm{B}). \tag{2.1}$$

where $*$ denotes the convolution and A and B represent the sample and aperture structure respectively. Assuming no other aberrations, the Fourier transform of the back aperture gives the PSF. The Fourier transform of a circle is an 2D Airy pattern, as shown in Fig. 2.3 (e), therefore, if the back aperture is a circle, the entire object is convolved with an Airy pattern PSF to form the image. In general, all other aberrations contribute to the PSF, and the distance to the first minimum of the PSF gives the resolution.

Defocus is another form of aberration. The effect of defocus depends on the illumination of the sample. For example, if the sample is illuminated with a single plane wave, the depth of field is extended. If the sample is illuminated by a range of plane waves, the depth of field is reduced. Conversely, high NA illumination gives higher lateral resolution, Fig. 2.4. The resolution of the microscope is given by,

$$d = \frac{1.22\lambda}{\mathrm{NA}_{obj} + \mathrm{NA}_{ill}} \tag{2.2}$$

where d is the smallest distance betweens two distinguishable points, λ is the wavelength of light used, and NA_{obj} and NA_{ill} are the NAs of the objective and illumination respectively. If white light is used, λ is typically set at around 500 nm. Microscope illuminations usually allow control of the NA_{ill} with a variable aperture placed in the Fourier plane of the sample. The numerical aperture of the illumination is linked to its spatial coherence. If the NA is high, then light is travelling in many directions and the coherence is low. Conversely high spatial coherence is achieved with low numerical aperture. How an object goes out of focus is described by a 3D PSF. In general, aberrations can be described by a basis set of orthogonal functions known as the Zernike polynomials.

The NA of the objective sets the limit of the resolution, however, contrast is another important feature of a microscope image. Many biological samples are mostly transparent, lacking absorbing pigments. Staining biological samples is a commonly used practice to visualise these features, however, it is also possible to use optical techniques. Despite not absorbing light, biological samples (like cells) will have a different refractive index compared to the surrounding medium. This means the cells change the optical path length and introduce a phase shift to the light in the image. A camera (or a human eye) can only detect intensity variations, meaning the phase variations are invisible. Phase

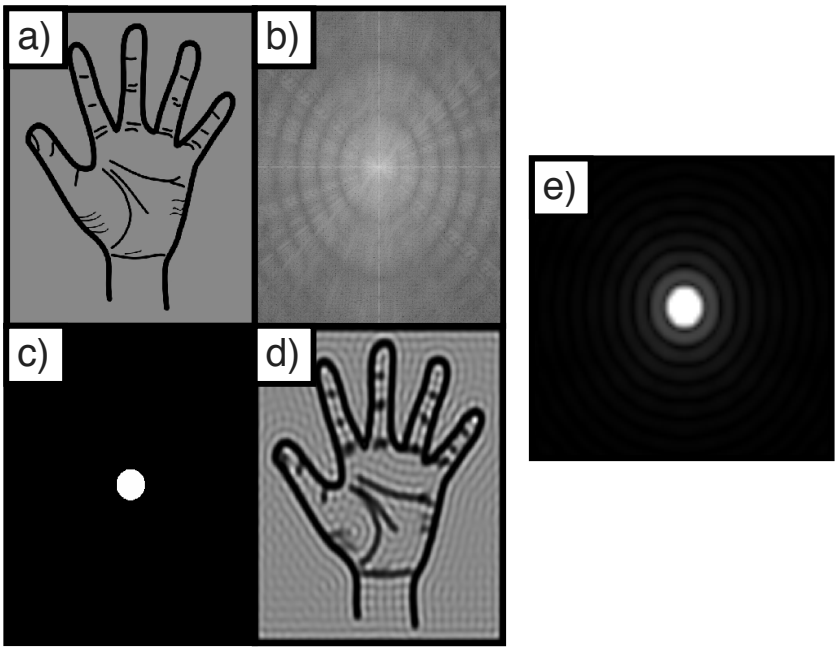

Figure 2.3: The effective of a finite aperture on an image. a) shows a test image. b), the Fourier transform of the test image. c) shows the back aperture of the objective which multiplies b), blocking high spatial frequencies, d) is the resulting image which is given by the convolution of the object in a) and the PSF (shown in e)).

contrast microscopy is an optical technique which converts the phase changes into intensity changes. This is done by modifying the back aperture of the objective so that the illumination light is phase shifted by $\frac{\pi}{2}$. When the image is formed, the illumination light interferes with the scattered light, and, because of the phase shift, the resulting intensity is sensitive to phase changes from the sample. To further increase contrast, the illumination light is attenuated by 50%. The phase change should only be applied to the illumination light, hence low NA illumination can be used as this focusses to a small area on the back aperture (meaning that phase shift of scattered light is minimised). This leads to a large depth of field, and loss of resolution (by Eq. 2.2). To avoid this, Zerinke phase contrast was developed. This involves illuminating the sample with a narrow hoop (rather than a filled disk). The phase shift given by the objective's back aperture then occurs only for a corresponding hoop. This allows phase contrast to work with a shorter depth of field and higher axial resolution, although the hoop introduces a halo artefact to the phase objects.

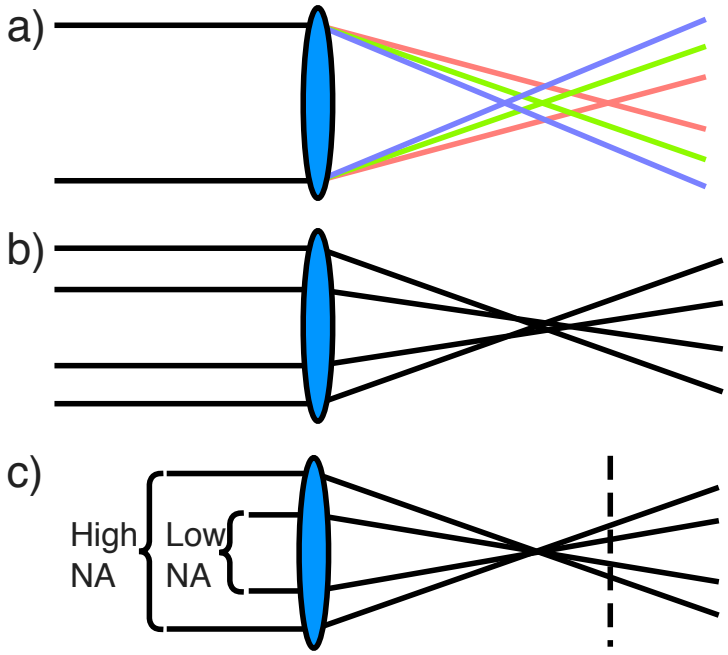

Figure 2.4: Ray optical diagrams of different aberrations. a) Chromatic aberration is where different colours of light are focused differently by a lens. This can be corrected by an achromatic lens. b) Spherical aberration is where rays going through different positions of the lens get focused at different distances. c) shows the effect different Numerical Apertures (NAs) have on defocus. High NA images go out of focus faster than low NA, meaning the depth of field is reduced, but the lateral resolution is increased. The Depth of field scales with the square of the NA, while resolution is linear with NA.

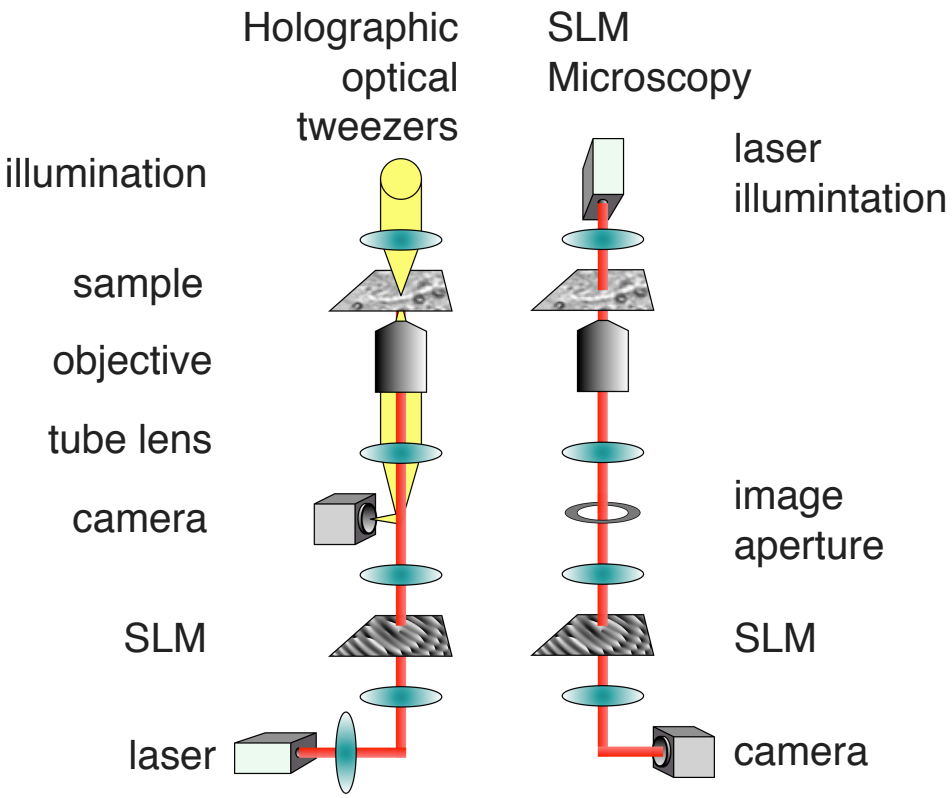

Figure 2.5: A comparison of holographic optical tweezers with SLM microscopy. In SLM microscopy, the white light illumination is replaced with a monochromatic source such as a laser. Also, the camera is moved to after the SLM, where it images multiple diffracted images. The image aperture is used to restrict the field of view so that many images can be displayed side by side on the same camera chip. Also, because SLMs have a finite aperture, care must be taken in imaging the back aperture on to the SLM to avoid loss of resolution.

2.2 SLM microscopy

That modification of the spatial frequencies of a sample gives useful imaging modes is not limited to phase contrast. In fact, there are numerous modifications, all of which are designed to meet a specific challenge in microscopy. Recently, spatial light modulators have been used to give unprecedented control of the spatial frequencies of a microscope image, in terms of complexity and reconfigurability. In an SLM microscope, each spatial frequency can be phase shifted by up to a full wavelength [43]. If combined with a grating, each spatial frequency can also be attenuated by any desired amount. For example, phase contrast can be emulated by setting the pixels corresponding to the illumination light on the SLM to $\frac{\pi}{2}$. This can either be a central spot, or a hoop as in Zernike phase contrast.

The experimental configuration of an SLM microscope is similar that of holographic optical tweezers, with many components in identical locations, Fig. 2.5. The SLM is placed

in the image plane of back aperture (i.e., the Fourier plane of the sample). In holographic optical tweezers, the SLM is used to display a diffraction grating and therefore create many focus beams in the sample. In SLM microscopy, the system is effectively run in reverse: the diffraction pattern of the sample is in turn diffracted off the SLM to create many images (Fig. 2.6). Just as in optical tweezers, the images can be at different focal depths, or be holographically shaped to give different point spread functions [44].

The illumination source in an SLM microscope is required to be monochromic. This is because different wavelengths will diffract from the SLM at different angles. However, a small temporal bandwidth is desired as speckle is a problem for high temporal coherence (as is the case of laser speckle). If a laser is to be used for illumination, a rotating diffuser is used to destroy the temporal coherence by averaging over many speckles. So long as the rotation rate is faster than the image acquisition rate then evenly illuminated images are obtained. In this case, the diffuser is placed at the position of the source in Fig. 2.6. Another approach is to use a high power LED and a closely matched bandpass filter. A bandwidth of around $5 - 10\,\mathrm{nm}$ is suitable for the diffraction angles used in SLM microscopy. The filter can be placed at any point between the SLM and the camera.

The spatial coherence is also an important consideration for the illumination of the sample in SLM microscopy. Köhler illumination (Fig. 2.6) gives control of this, as well as giving even illumination of the sample. Köhler illumination works by imaging the Fourier transform of the source on to the sample, which means the source is completely out of focus. The area illuminated is controlled by the field diaphragm. It is important to illuminate only the region of interest as otherwise light scattered from outside the region can show up in the image. Prior to illuminating the sample, the source is imaged onto the condenser diaphragm which is used to control the NA of the illumination and, therefore, the spatial coherence.

The imaging system after the sample consists of an objective and tube lens. This is used to form an intermediate image, in which is placed an aperture to restrict the field of view. This is necessary to ensure the diffracted images do not overlap on the camera chip. In some instances, only one diffracted image is required, in which case (owing to less than 100% diffraction efficiency of the SLM) the zero must be blocked by a beam stop. This allows the full camera chip to be used to record one image. The size of the image can always be increased by optical magnification (i.e., a longer focal length of lens l_2 in Fig. 2.6). To increase the field of view, however, requires either a higher diffraction angle from the SLM, or a longer focal length of lens l_1. Importantly, increasing the focal length of l_1 magnifies the size of the back aperture on the SLM. This should be done provided the SLM is not overfilled as clipping of the back aperture results in a loss of resolution and a distorted point spread function.

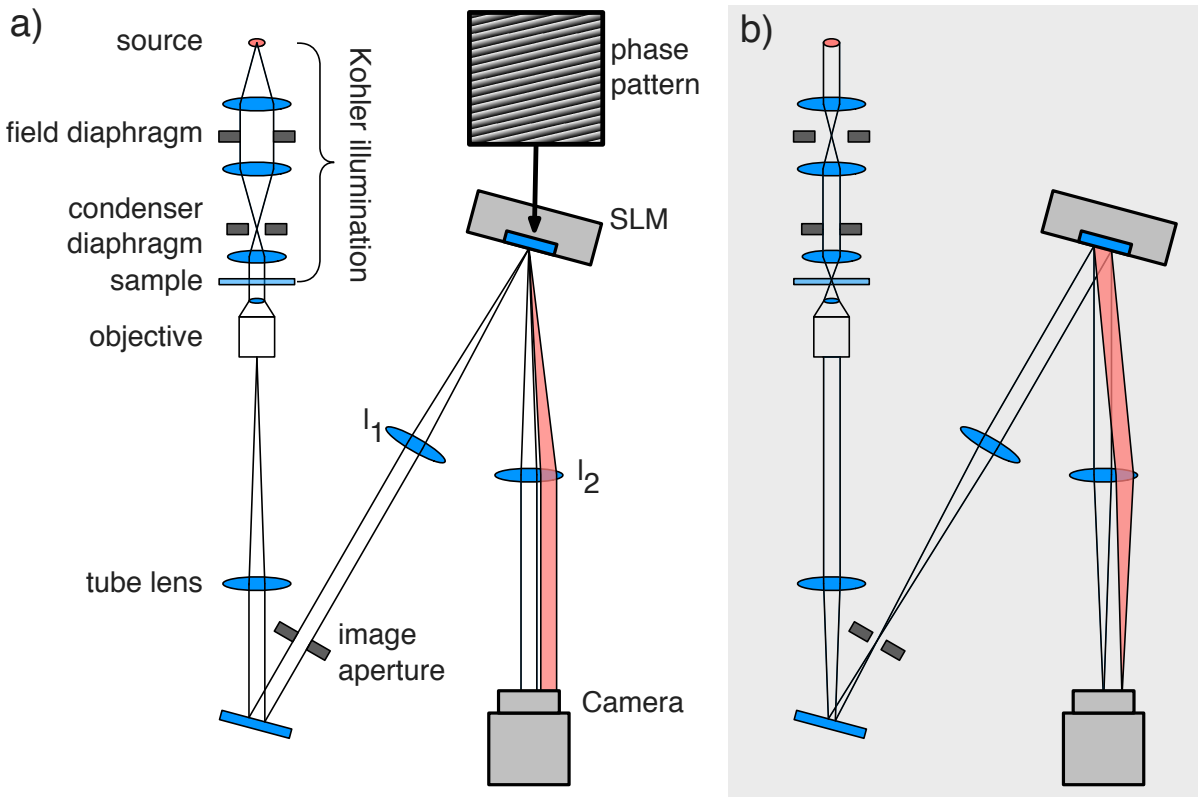

Figure 2.6: The optical layout of an SLM microscope. a) and b) show the same system, but rays are traced for conjugated planes. The SLM is placed in the Fourier plane of the sample where it diffracts the image at an angle (shown in red). Köhler illumination is used to give even illumination of the sample. The image aperture is used to restrict the field of view so that many images can be displayed side by side on the same camera chip. Also, because SLMs have a finite aperture, care must be taken when imaging the back aperture on to the SLM to avoid clipping and a loss of resolution.

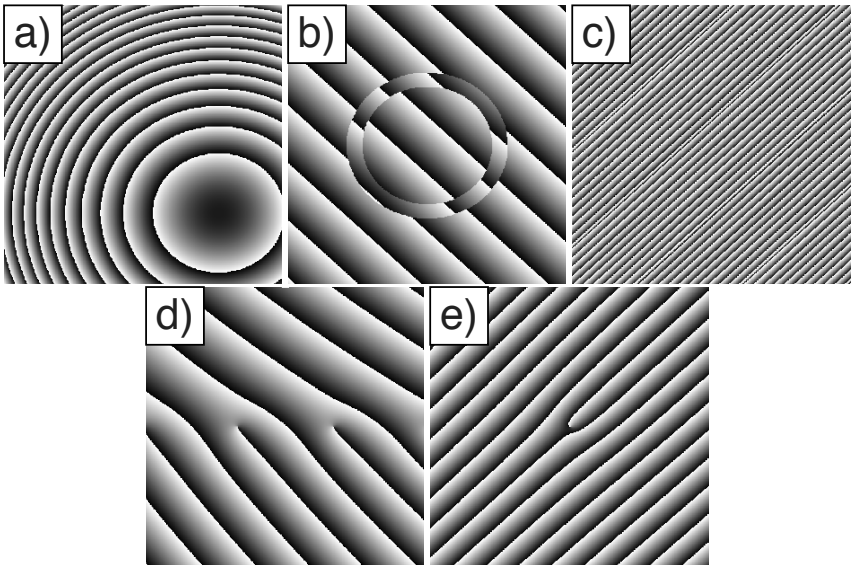

Figure 2.7: Examples of Fouier filters used in SLM micrscopy. a) shows a lens and a grating combined to give an off axis image, focused at a new focal plane in the sample. The others are: b) Zernike phase contrast, c) DIC, d) DHPSF, e) Spiral phase contrast.

2.3 Examples of SLM Microscopy

By inserting an SLM into the imaging path, additional aberrations can be introduced to the image. Fortunately, these can be compensated for by a fixed pattern applied to the SLM. Other aberrations from lenses or even the sample can be corrected by the SLM and additional focusing (Fig. 2.7 (a)) can also be performed [45].

Both the $\frac{\pi}{2}$ phase shift and 50% attenuation of the illumination light in phase contrast microscopy can be replicated by an SLM (Fig. 2.7 (b)). Normally, special phase contrast objectives need to be used which have an in built phase shift hoop. This means that the system is quite inflexible as the illumination source must image exactly on to that hoop. In an SLM microscope, the phase shifting hoop is reconfigurable, meaning even regular objectives can be converted to phase contrast mode. Insightfully, phase contrast has been performed without a hoop-shaped illumination, but rather a "random dot" distribution of illumination sources. In this case, an SLM was used in the illumination to create a small number of random different angles which illuminate the sample. After the sample, each of these angles corresponds to a position in the Fourier plane, where second SLM phase shifts the illumination light. Because the structure of the illumination is random, the halo artefact of Zernike phase contrast is removed [46].

Spatial Light Interference Microscopy (SLIM) takes advantage of an SLM's ability to provide a 2π phase shift [47, 48]. In this case, the microscope is set up in Zernike phase contrast mode, but with an SLM positioned in the Fourier plane. The hoop-shaped

illumination is imaged on to a corresponding hoop on the SLM where the phase shift is initially set at 0. An image is recorded on a digital camera, then the phase shift is increased to $\frac{\pi}{2}$, and another image is recorded. In total, four images are recorded at phase shifts of 0, $\frac{\pi}{2}$, π, and $\frac{3\pi}{2}$. From these images it is possible to calculate the optical path length and, ultimately, the thickness of the sample.

If, instead of phase shifting the illumination light, this light is completely blocked, darkfield microscopy is effected. Darkfield acts light a high pass filter, giving very good contrast for weakly scattering objects like nanoparticles. Darkfield images can be produced either with a physical beam stop in the Fourier plane, or with an SLM displaying a diffraction grating everywhere *except* for the illumination.

Differential Interference Microscopy (DIC) is another commonly used imaging technique which can be replicated with an SLM [49]. In traditional DIC, two Wollaston prisms are used to create two illumination beams, one of which is phase shifted by $\frac{\pi}{2}$. The two beams pass through the sample slightly offset to one another. The beams are then overlapped with another pair of Wollaston prisms to form the image where each point in the image is given by the interference of the two beams. As the beams have passed through slightly different points of the sample, any phase difference between the beams affects the interference. The effect is that phase gradients of the sample show up as intensity gradients in the image, giving a pseudo-relief effect. SLM microscopy can reproduce the relief effect without the need for Wollaston prisms (Fig. 2.7 (c)). Instead, the sample is illuminated with somewhat coherent light (NA of around 0.5), and the SLM, positioned in the Fourier plane, diffracts *two* images at angles which slightly differ from one another. The phase for one of these gratings is shifted by $\frac{\pi}{2}$. Owing to the coherence of the illumination, the resulting image is the coherent sum of the two diffracted images, giving the same relief effect to phase objects. The flexibility of SLMs means the displacement angle and the shear displacement can be tuned to achieve optimal images depending on the sample and imaging properties.

SLMs have been used to prototype altogether new forms of microscopy. One such example is Spiral Phase Contrast [50, 51], which is used for edge enhancement of phase or amplitude objects. In this mode, coherent light (low NA) is used to illuminate the sample. The SLM is again placed in the Fourier plane of the sample, but this time displays a spiral phase pattern, i.e., the phase increases from $0-2\pi$ in one rotation around the centre of the SLM (Fig. 2.7 (e)). This pattern is usually used in the generation of ($\ell = 1$) Laguerre-Gaussian laser modes. Here, however, it is the scattered light which obtains the spiral phase structure. For most points in the image, there will be destructive interference because as much light has been phase shifted by π as has not. Only at points which have scattered light inhomogeneously will there be constructive interference. These

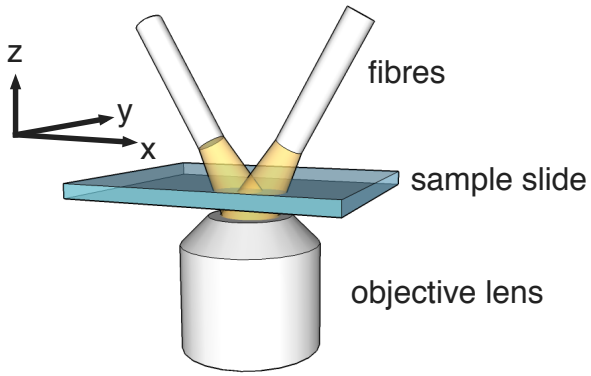

Figure 2.8: The axes defined for stereo microscopy.

points correspond to steep step changes in phase or amplitude in the sample. (E.g., a prism shaped object will only scatter light to one side of the back aperture, therefore the phase shift does not cancel with light on the opposite side, and there will be constructive interference). The edge enhancement provided by spiral phase contrast has now been transferred from SLM microscopy to regular, white light, microscopy by a refractive spiral phase plate which is not as severely effected by dispersion.

The Double Helix Point Spread Function (DSPSF) is another form of microscopy initially prototyped on an SLM [52] (Fig. 2.7 (d)). Here, each point in the sample is convolved with a three dimensional "Double Helix," which results in a point like object appearing as two lobes of intensity which rotate around one another as the point moves through the focal plane [53]. From image analysis of the two lobes, the z position above or below the focal plane (as well as the (x, y) position) can be determined. In the initial work, a series of fork dislocation are displayed on the SLM, where the separation and number of the forks can be experimentally tuned. Again, a refractive white light alternative has been developed for use in a wide range of microscopes. The DHPSF has been used in the super-localisation imaging to determine the full 3D distribution of fluoresent molecular emitters.

Obtaining 3D position information for 2D images has a number of solutions, each with advantages and disadvantages. The DHPSF, for example, works over the full field of view, though has a limited z range (i.e., one rotation of the double helix), as well as giving distorted images. Holographic microscopy can be used to localise 3D objects, although requires a large amount of computational load to calculate the images from a recorded diffraction pattern. If the object to be imaged is known, a series of images can be recorded of the image at different focal depths. Then, as the object moves in z, a pattern matching algorithm can be used to determine how far above or below the focal plane the object is.

In addition to these methods, stereo microscopy has been developed. Stereo mi-

croscopy works by utilising two different viewing angles of the sample to triangulate the position of an object. Stereo microscopy is a old idea, originally implemented with two eye pieces. In the new version, high speed cameras and two illumination sources are used [54, 55]. Effectively, the set up couples the x position of an object to its z position, leaving the y position untouched, Fig. 2.8. As there are two images, it is possible to decouple the x and z position to obtain the 3D positions. The two viewing angles can be separated by colour, or with a pair of prisms in the Fourier plane. By replacing the prisms with an SLM, addition benefits can be achieved, such as autofocusing, and darkfield-stereo. These features are discussed in more detail in Part II of this thesis, where I describe the development of a compact SLM microscope capable of emulating many of the above examples of SLM microscopy, and in particular, stereo microscopy.

2.4 Summary

SLMs in microscopy prove useful as they can modify the point spread function, which governs the resolution of the image formed by a microscope. Owing to the Fourier transform performed by lenses, placing an SLM in the Fourier plane of a sample gives direct access to the spatial frequencies. By modulating these frequencies, many traditional microscopy techniques can be emulated, and new ones can be developed. SLM microscopy is limited to a monochromic light source, as well as a reduced field of view. However, owing to the flexibility of SLMs, innovative forms of microscopy can be tried out quickly and easily. SLM microscopes are able to perform numerous forms of microscopy at the same time, offering unique advantages over traditional microscopy, as well as being dynamically reconfigurable, capable of responding to the changes in the sample in order to maintain optimal images.

Part I

Holographic Optical Tweezers

III
Synchronisation of stochastic oscillators

Transition events are ubiquitous in physics, chemistry and biology [25, 56], where a system fluctuates between states. The states are typically separated by an energy barrier which is large compared with the average energy of the system. If the system is perturbed sufficiently, then it will be able to overcome the barrier and change state. The extra energy needed to overcome the barrier also needs a means of dissipation in order for the system to relax into the new state. In colloidal science, the solvent fluid provides the required perturbations to overcome a barrier in the form of Brownian motion. At the same time, the low Reynolds number environment ensures any motion is damped, Chapter 1. Optical tweezers can provide an energy landscape whereby a colloidal particle experiences an energy barrier existing between two spatially separated optical traps. It has been shown that, given carefully controlled experimental conditions, it is possible for the particle to randomly hop between the traps, i.e., the potential of the system is bistable [26, 29, 27]. There are other techniques to achieve bistable traps, including a single beam aerosol trap [57].

Not only do solvent fluids (at the small length scales of colloidal particles and biological marcomolecules) play this twofold role of constantly providing a fluctuating force and viscous dissipation of energy, they also display long range hydrodynamic correlations that inevitably couple the dynamics of suspended objects. For example, two colloidal particles in independent optical traps display strong correlations in their Brownian motions [58]. Whether the same hydrodynamic interaction could result in some degree of correlation in the hopping dynamics of nearby bistable systems is still an open and important question [59, 60, 61, 62, 63]. For instance, understanding how hydrodynamics can bias activated jumps over energy barriers can have a potential impact on the study of the slow dynamics of structural rearrangements in colloidal glasses and gels.

In this work we investigate two colloidal spheres, independently trapped in separate

bistable optical potentials. We demonstrate the experimental result that the two particles hop simultaneously more frequently when crossing the barrier in the same rather than opposite directions. We show that the difference between the number of co-hops and counter-hops reduces as the inverse separation between the two systems, showing that the strength of the phenomenon is first order in the hydrodynamic coupling.

In this chapter I acknowledge contributions from Dr Arran Curran who built the optical tweezers and wrote hologram and camera control software. This work was published in 2012 in Physical Review Letters [64].

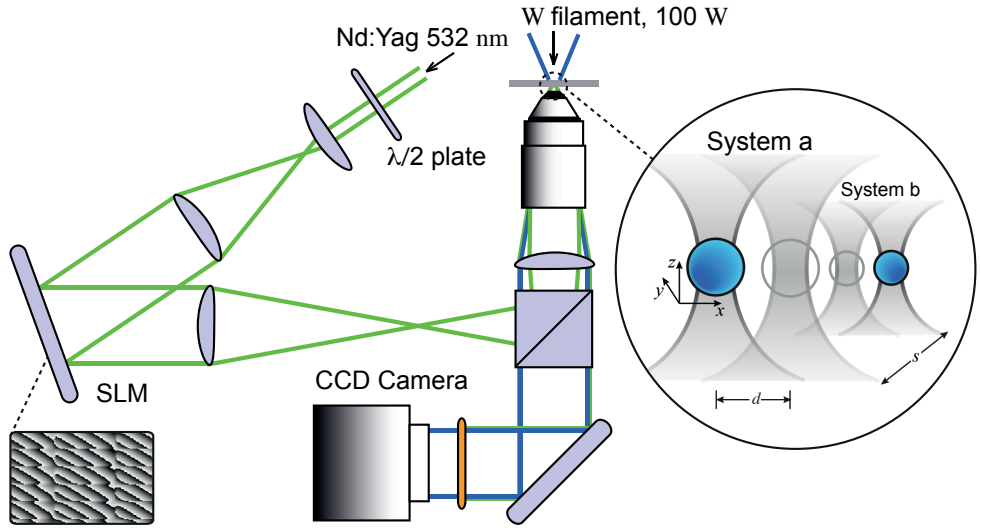

Figure 3.1: Holographic optical tweezers. A spatial light modulator is used to generate multiple traps at the focal plane of the ×100 oil-immersion microscope objective. Silica spheres are trapped with a frequency-doubled Nd:Yag laser, 5 μm above the cover slip. Left inset shows the hologram used to landscape two side by side bistable potentials. A schematic of the two optically trapped spheres in independent bistable potentials is inset on the right.

3.1 Procedure

The bistable optical landscape is achieved holographically, where a phase pattern is generated by a gratings and lenses algorithm and displayed on a Spatial Light Modulator (SLM) [65, 66]. Holograms are imaged at the back aperture of a Carl Zeiss ×100 1.3 NA oil-immersion microscope objective and focused into a multispot array located at the focal plane (Fig. 3.1). Each bistable potential is constructed by having two individual focal

spots placed in close proximity, such that a surmountable energy barrier forms between the two traps. We create two bistable potentials separated by a distance s, which is also controlled holographically.

Our samples are prepared with silica spheres (of radius, $a = 0.4\,\mu$m, Bangs Laboratories) in deionized, distilled water. When preparing our samples we add a weak saline solution just before sealing so that any free debris is immobilised on the cover slip due to the reduced Debye length [67]. This process is limited by the sedimentation of the particles on to the coverslip, which allows enough time to capture the two spheres required for the experiment. Sample cells are constructed with a single concave microscope slide (GX Optical, concave depth = $500\,\mu$m) and a square cover slip (thickness number 1.5), sealed with UV-curing optical adhesive. Using a few mW of frequency-doubled Nd:Yag laser light (532 nm), the trap stiffness in each trap is set at $\kappa \sim 2\,\mu\mathrm{Nm}^{-1}$. A fast camera (Prosilica GC650), operating at a frame rate of 1.37 kHz is used to track the position of the spheres in the $x - y$ plane.

As the particles are smaller than the typical $2\,\mu$m diameter bead used in many optical tweezer experiments, a modification of the centre of mass algorithm described in Ref. [35] was developed. Here, the term "mass" refers to how much weighting each pixel is given, which is equal to its intensity. If the particle to be tracked is small, any threshold applied to the image (in order to remove background pixels) results in only a few pixels being above the threshold. This means a small displacement can move a pixel above the threshold, giving a overly large contribution to the centre of mass algorithm. For small particles, this leads to certain configurations of pixels being on, meaning certain positions are more likely to be measured than others and, consequently, the histogram appears to have multiple peaks. In the case of small particles, rather than applying a threshold it is more appropriate to subtract a background value, then coerce any negative pixel values to zero. This means that if the value of an edge pixel goes just above the background value, its contribution to the centre of mass is small, and a more precise measurement of the position is obtained. For each separation, s, time sequences of the spheres' centre of mass, $x(t)$ and $y(t)$, are extracted in blocks of 10^5 frames (73 seconds) and accumulated for a total time period of 36 minutes, significantly longer than the average between hops, which is of order one second.

Care is taken to maintain symmetric bistable potentials by adjusting the optical intensities of each trap. For the results presented here, a sequence of data is recorded, then analysed in terms of the position histogram. If one side of the bistable potential has been occupied by the sphere more so than the other, then a proportion of that difference is used to automatically adjust the power of the two traps, Fig. 3.2. The gain of this closed loop control was manually calibrated, and gave more consistent potentials compared to

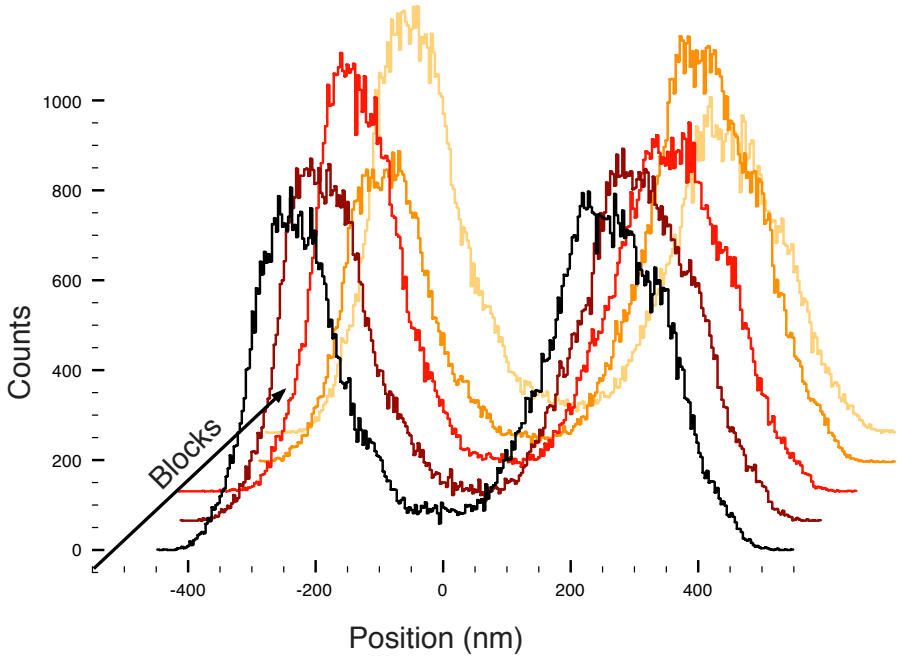

Figure 3.2: Histograms of a sphere in a bistable optical trap. The position is recorded in sequences of 100,000 frames (73 seconds). After each sequence, the intensity of the trap is adjusted to maintain a balanced potential. Five consequent sequences are shown.

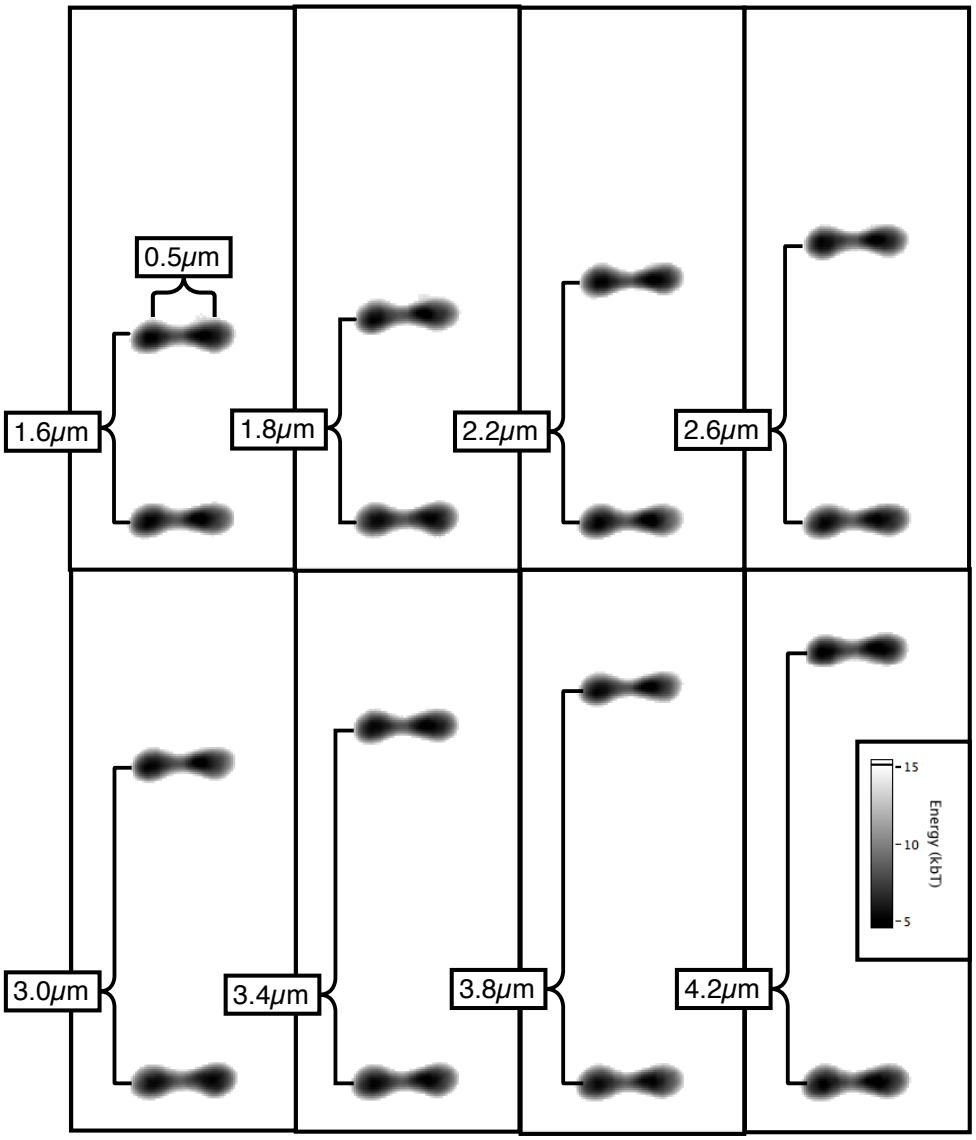

Figure 3.3: Optical potential landscapes experienced by two 800 nm silica spheres. Potential energy distributions are recovered from particle trajectories, $x(t)$ and $y(t)$, as described in the text. The data is binned into bins of size 20 nm^2

no feedback which suffered from drift leading to unbalancing of the potential. This automated balancing also meant the whole experiment could be automated (i.e., balance traps, record 10^5, (repeat), increase the distance between the two systems, balance, ...). Stilgoe *et al.* have recently given a report on the complexity of creating optical potentials using two optical traps, where they identified a third central trapping position for larger particles [68].

3.2 Analysis

Since the sampling rate is much greater than the corner frequency in the power spectrum of Brownian fluctuations, $f_c \sim 40\,\mathrm{Hz}$, the normalised histogram of particle positions $\rho(x, y)$ provides a direct measurement of the Boltzmann distribution, $\rho(x, y) = Z^{-1} \exp[-U(x, y)/k_B T]$, where k_B, T and Z are respectively the Boltzmann constant, the temperature of the surrounding fluid and the normalisation constant. By inverting $\rho(x, y)$ we can directly access the underlying optical potential in units of $k_B T$ (Fig. 3.3 and 3.4 (b, d)).

The obtained potentials shown in Fig. 3.3 are for all separations, s, confirming that the optical landscapes of each system are not significantly changed as they approach. It is worth noting that, although the optical landscape is made of two optical traps whose centers are separated by 800 nm, the separation between the minima of the obtained bistable potential is only $d \sim 500\,\mathrm{nm}$. This is due to the sphere experiencing restoring forces from both optical traps, leading to an offset in the equilibrium position in each individual trap and shortening the hopping distance.

Figure 3.4 (a, c) shows a 10 s sample trace of particle position on the x-axis (the axis along which hopping occurs) taken at large separation, $s = 3.6\,\mu\mathrm{m}$. The corresponding potentials are given in Fig. 3.4 (b, d). A single particle power spectrum is shown in Fig. 3.4 (e) for the shortest separation. Two separated timescales are visible, a low frequency component describing the hopping dynamics and a high frequency component describing the fluctuations around the local minima. For an isolated hopping system, the power spectrum, $\hat{x}(\nu)$, of the particle's x position will be a double Lorentzian spectrum, where the first term is the standard spectrum for a bead of friction coefficient $\gamma = 6\pi\eta a$ (where $\eta = 1\,\mathrm{mPas}$ is taken as the viscosity) in an optical trap of strength κ, and thus, a corner frequency given by $f_c = \kappa/2\pi\gamma$. The second term describes hopping events over a distance d and an average hopping rate (f_h), found by first ascertaining the correlation function of the hops. If the hops occur between two states, $d/2$ and $-d/2$ (Fig. 3.5), $x(t)x(t+\tau)$ takes a value of $d^2/4$ when an even number of hops, k, have occurred between t and $t+\tau$. This has a probability found through the Poisson distribution:

$$Prob\left(x(t)x(t+\tau) = \frac{d^2}{4}\right) = \sum_{k=0,2,4\ldots}^{\infty} \frac{(f_h\tau)^k e^{-f_h\tau}}{k!}. \tag{3.1}$$

Similarly, the probability of $x(t)x(t+\tau)$ having a value of $-d^2/4$ is given when there are a odd number of hops between t and $t+\tau$,

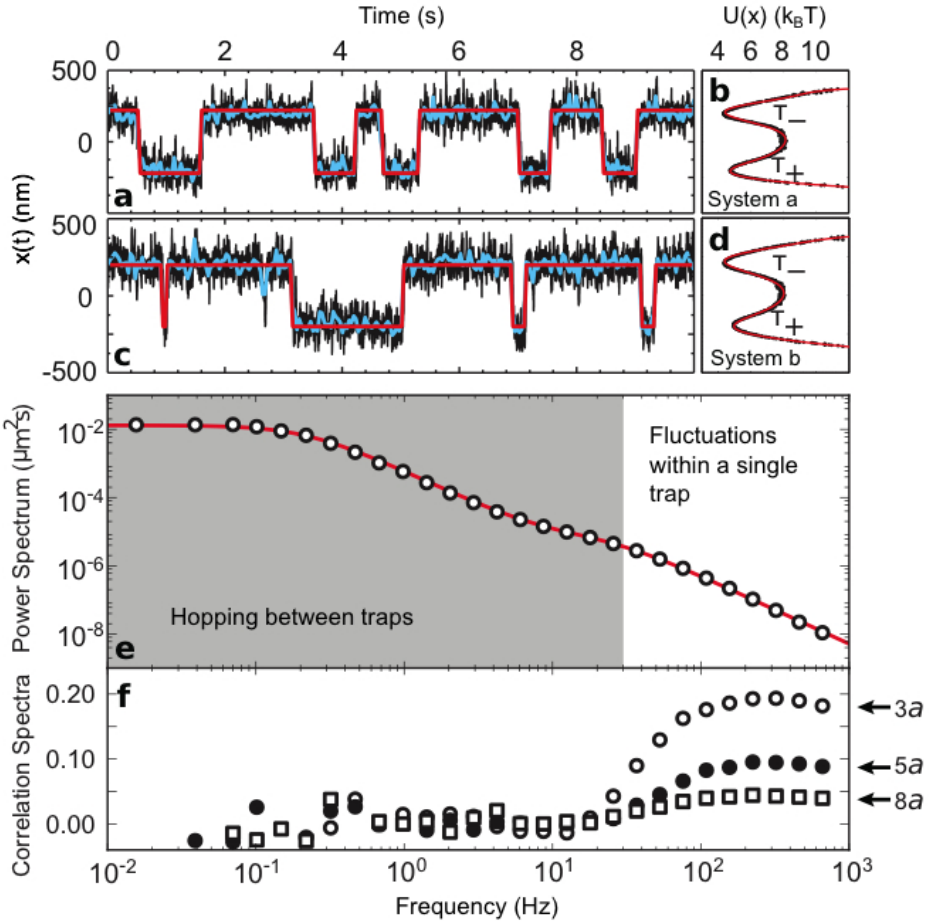

Figure 3.4: (a, c) 10 s sample of the spheres' position along the x-axis (black line) for each system separated by $s = 3.6\,\mu$m. The block filtered (blue line) and digitised traces (red line) are also shown. (b, d) Corresponding potentials (black ∘) with fitted polynomials (red line). (e) Single particle power spectrum along with a double Lorentzian fit as discussed in the text. (f) Correlation spectra for three separations evidencing hydrodynamic correlations in the high frequency region.

$$Prob\left(x(t)x(t+\tau) = -\frac{d^2}{4}\right) = \sum_{k=1,3,5\ldots}^{\infty} \frac{(f_h\tau)^k e^{-f_h\tau}}{k!}. \tag{3.2}$$

The hopping frequency can be anticipated using Kramers' theory [25], $f_h = \omega_0 \exp[-\Delta U/k_B T]$, where ΔU is the height of the potential barrier and the prefactor $\omega_0 = m_0\sqrt{\kappa_i \kappa_s}$ depends on the particle mobility, $m_0 = 1/\gamma$, and on the curvatures of the underlying potential at the stationary points, $\kappa_{i,s} = |\partial^2 U/\partial x^2|_{x=x_{i,s}}$. The expectation value of $x(t)x(t+\tau)$ is then,

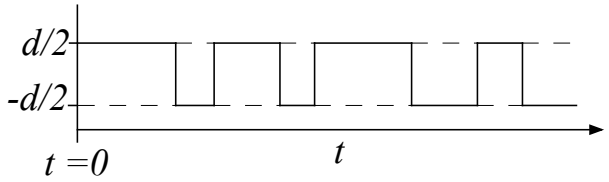

Figure 3.5: The notation used for deriving the hopping contribution to the power spectrum, Eq. 3.7. The motion of the particle is course grained such that only two states are possible, $d/2$ and $-d/2$. The average waiting time between hops is $1/f_h$. The correlation between t and a later time, $t+\tau$, is found by considering the probability of an even or odd number of hops between these times.

$$\langle x(t)x(t+\tau)\rangle = \frac{d^2}{4}\left(\sum_{k=1,3,5\ldots}^{\infty}\frac{(f_h\tau)^k e^{-f_h\tau}}{k!} - \sum_{k=0,2,4\ldots}^{\infty}\frac{(f_h\tau)^k e^{-f_h\tau}}{k!}\right), \tag{3.3}$$

$$= \frac{d^2}{4}e^{-f_h\tau}\left(1 - f_h\tau + \frac{(f_h\tau)^2}{2!} - \frac{(f_h\tau)^3}{3!} + \ldots\right), \tag{3.4}$$

$$= \frac{d^2}{4}e^{-2f_h\tau}. \tag{3.5}$$

Using the Wiener–Khinchin theorem, we can find the hopping fluctuation's contribution to the power spectrum,

$$\mathrm{FT}(\langle x(t)x(t+\tau)\rangle)(\nu) = \frac{d^2}{4\pi}\frac{2f_h}{\nu^2+(2f_h)^2}, \tag{3.6}$$

which is a Lorentzian. Including the term for Brownian fluctuations, the power spectrum becomes,

$$\langle\hat{x}^*(\nu)\hat{x}(\nu)\rangle = \frac{k_BT}{\pi\kappa}\frac{f_c}{\nu^2+f_c^2} + \frac{d^2}{4\pi}\frac{2f_h}{\nu^2+(2f_h)^2}. \tag{3.7}$$

Knowing the temperature, viscosity and particle radius means that all remaining parameters can be directly evaluated from the features of the stationary points in the obtained potential energy. The resulting curve is shown as a solid line in Fig. 3.4 (e) and fits the measured power spectrum well. Searching for hydrodynamic correlations we plot in Fig. 3.4 (f) correlation spectra $\langle\hat{x}_a^*(\nu)\hat{x}_b(\nu)\rangle$ normalised by the average single particle power spectra $(1/2)\sum_{\alpha=a,b}\langle\hat{x}_\alpha^*(\nu)\hat{x}_\alpha(\nu)\rangle$. A marked positive correlation at high frequencies gets larger as the two systems approach. This is the well known phenomenon by which the mobility of rigid motions is higher than that for relative motions so that at short times the particles tend to move collectively [58]. However, at low frequencies dominated by hopping dynamics, no sign of correlation is observable even when the two systems are

close together.

Despite the lack of any obvious sign of collective motion in the low frequency correlations spectrum (Fig. 3.4 (f)), further analysis of our data reveals a more subtle correlation. Rather than averaging the correlation over all points, we examine only the instances where both particles hop at the same time, either in the same direction or opposite direction. To examine these instances we first need to define what is a hop, and what is not. This is important as high frequency motion at the saddle point can lead to multiple crossings for each hop. Three possible criteria were looked at: 1) a Schmitt trigger, where a hop is counted if the bead moves past the mid point of the traps and then past a second threshold, 2) a gate time set so that each hop has a prescribed duration, during which time further hops are ignored, 3) a low pass filter, to filter out the high frequency motion.

A Schmitt trigger reduces the number of hops to only those trajectories from one side of the bistable potential to positions well inside the other. Therefore, the chance of a return hop immediately after could be reduced as the bead has to undergo a sizeable displacement (if the trigger is set too large). We want to allow all time intervals to have equal chance of containing a hop to be consistent with Poission statistics. Also, setting the value of the Schmitt trigger is somewhat arbitrary. On its own, a Schmitt triggered hop lasts only one frame, so coincident hops are unlikely. For these reasons, the Schmitt trigger was not used.

A gate time could be used to both reduce the high frequency hops and allow for more coincident hops to occur by looking for a hop in the other system during the gate, Fig. 3.6. The disadvantage is that an even or odd number of crossings of the saddle point could happen during the gate time, meaning the direction of the hop is ambiguous. Allowing a gate time of G frames, the probability of K coincideny hops between in system b for each individual hop in system a is found via the Bionomial distribution:

$$Prob(K) = \binom{2G-1}{K} \left(\frac{\delta t}{\tau_b}\right)^K \left[1 - \left(\frac{\delta t}{\tau_b}\right)\right]^{2G-1-K}, \tag{3.8}$$

where τ_b is the mean time between hops for system b, i.e., there are $2G-1$ chances of a coincident hop in system b for every individual hop in system a, each with a probability $\delta t/\tau_b$. A gate time means there exists a probability of more than one coincident hop occurring per individual hop. In fact, K could be any number from 0 to $2G-1$. The expectation value of Equation 3.8 is given by:

$$\langle K \rangle = \frac{\delta t}{\tau_b}(2G-1). \tag{3.9}$$

This is the expected number of coincident hops between systems a and b per individual hop in system a. To compute the total number of expected coincident hops, $\langle N \rangle$, in an

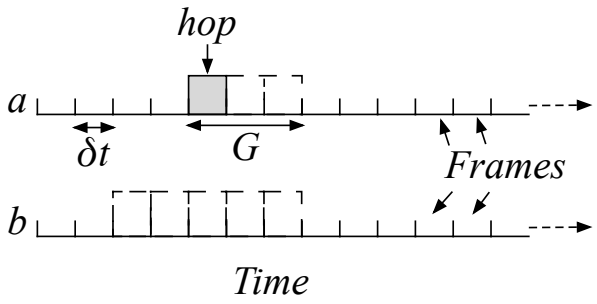

Figure 3.6: Identification of coincidence hops. A hop is identified in system a as the frame in which the position of the particle crosses the saddle point in the potential. A gate time, G, can then be applied such that a coincident hop is identified if a second hop occurs within either system a's or system b's gate time, a total of $2G-1$ frames. The above figure shows an example with $G=3$ frames.

experiment, we need to multiply by the number of hops in system a:

$$\langle N\rangle = \frac{T_{tot}\delta t}{\tau_a\tau_b}(2G-1), \tag{3.10}$$

where the total time of the experiment is T_{tot}, given by δt multiplied by the number of frames. As can be seen, the longer the gate time, the greater the number coincident hops. We shall use the simplest case of $G=1$, and the above expression simplifies to,

$$\langle N\rangle = \frac{T_{tot}\delta t}{\tau_a\tau_b} \tag{3.11}$$

A low pass filter provides a better approach to defining a hop. The position time series can be blocked (coarse grained) into 45 frames (Fig. 3.4 (a, c) blue line). This acts as a low pass filter with a cutoff frequency of 31 Hz, higher than the trap corner frequency, filtering out the fast dynamics of fluctuations during a hop, Fig. 3.7. This gives hops which are independent of each other, and increases dt so that the number of coincident hops increases. Our definition of a hop is then the bead crossing the saddle point after the data has been blocked. A coincident hop is a corresponding hop in the neighbouring system in the same block. We define p hops to be coincident hops in the same direction, and n hops to be coincident hops in the opposite direction.

The blocked data is then digitised into a two state variable $\bar{x}(t) \in -1, +1$, denoting the left and right states of the bistable potential (Fig. 3.4 (a, c) red line). For each system we then extract a time series of hop events from $-1 \to +1$ and $+1 \to -1$. This data represents a cumulative acquisition of 36 minutes at 1370 Hz, with around $15,000$ transition events. The distributions of intervals between hops are fitted with an exponential decay, yielding the characteristic dwell time for each state. These measured

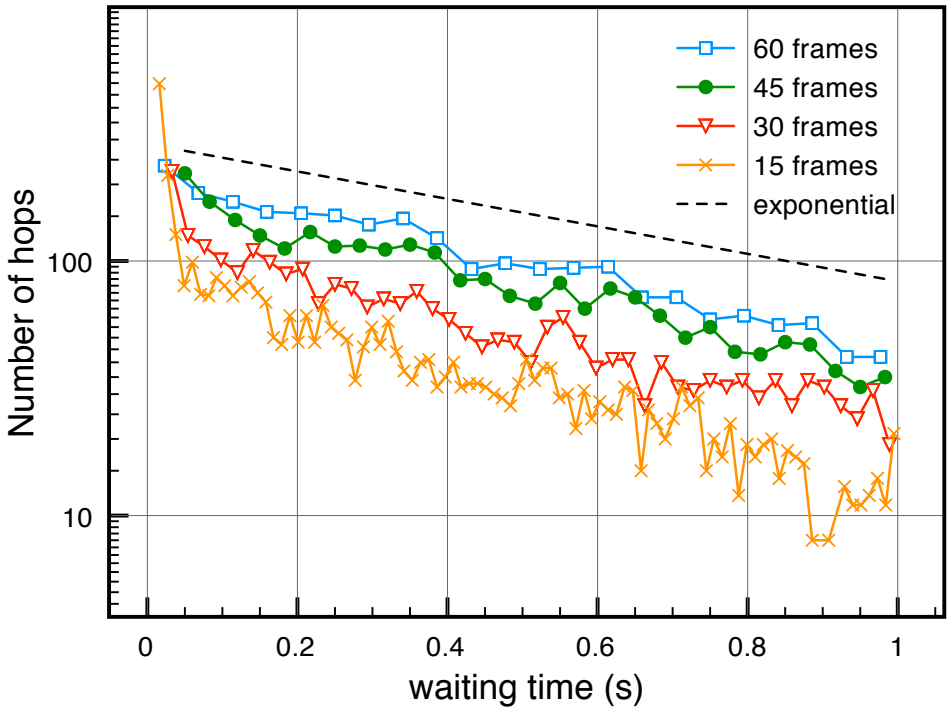

Figure 3.7: The effect of various blocking lengths on the histogram of dwell times for an individual hopping system. The histogram is binned such that each bin corresponds to one block. Independent hops would give an exponential decay, the form of which is shown with a dashed line. Short blocking lengths give non-exponential decays. This is due to high frequency fluctuations occurring as the particle makes a transition. We chose a blocking length of 45 fames.

dwell times are consistent with Kramers' formula applied to the shape of the underlying potential. Each bistable potential is fitted with an eighth order polynomial (Fig. 3.4 (b, d) red line), the second derivative of which gives the Kramers' prefactor term, ω_0, when evaluated at the stationary points. Numerical results of ω_k^{-1} are given in the third column of Table 3.1. The dwell times are measured from $x(t)$, the mean of which are given in the second column. The probability distribution of the dwell times are fitted with an exponential decay giving the first column in Table 3.1.

	Fit	Mean	ω_k^{-1}
System a	0.54	0.57	0.46
	0.66	0.68	0.62
System b	0.48	0.50	0.37
	0.74	0.73	0.61

Table 3.1: Characteristic dwell times for each individual potential obtained by exponential fitting to the probability distributions of the states' dwell times, along with the mean value of raw dwell times and from Kramers formula. All numbers are in units of s.

Each transition event is assigned a duration of one blocked sequence of frames, $\delta t = 33\,\text{ms}$, such that, for each frame, δt, there is a probability $\delta t f_h$ of a hop occurring, where f_h is the mean hopping rate in that system. Given two such randomly hopping systems, we expect that there would be a certain number of coincident hops, $\langle N \rangle$, by chance alone, Fig. 3.6.

For two uncoupled stochastic oscillators we expect an equal probability for symmetric and antisymmetric simultaneous hops ($p = n$). Figure 3.8 (a) shows the measured probabilities of p and n coincidences occurring over a range of system separations. With the two systems placed in close proximity to each other ($s \sim 2a$) the probability of observing a p coincidence is significantly greater than observing a n coincidence (error bars calculated from the standard deviation of the Binomial distribution, $\sqrt{N/4}$. At increasing separations, both p and n coincidence probabilities approach 0.5 ruling out the possibility that the synchronisation could be ascribed to asymmetries in the optical landscapes and external vibrations. We note that the total number of observed coincidences, $(p+n)/\langle N \rangle$, is unchanged with separation (Fig. 3.8 (b)). Coming back to Kramers' formula for single particle hopping rate, we notice that particle mobility appears as a prefactor to an energetic activation term. We may then conjecture that the rates of symmetric hops and antisymmetric hops have a similar form with an activation term and a prefactor that would also depend respectively on the collective and relative mobilities [69, 70, 71]. Moreover, the splitting between p and n seems to decay with distance as is the case for hydrodynamic splitting between collective and relative mobilities as shown by the $0.5 \pm (3/4)(a/s)$ lines

in Fig. 3.8 (a).

3.3 Conclusion

In conclusion, the thermally activated jumps of two 800 nm silica spheres in neighbouring bistable optical landscapes are shown to be coupled via hydrodynamic interactions. Due to the higher mobility of collective motions, when two systems are in close proximity, there is a higher probability of observing a symmetric hop whilst antisymmetric hops are less common. We argue that the experimental environment studied here provides an idealised representation of interacting stochastic oscillations that occur in nature. It will be interesting to extend the present study to a larger ensemble of bistable systems. For example, looking for the emergence of more complex, cooperatively rearranging regions could aid the understanding of the role of hydrodynamic interactions in the glassy dynamics of concentrated colloidal suspensions [72].

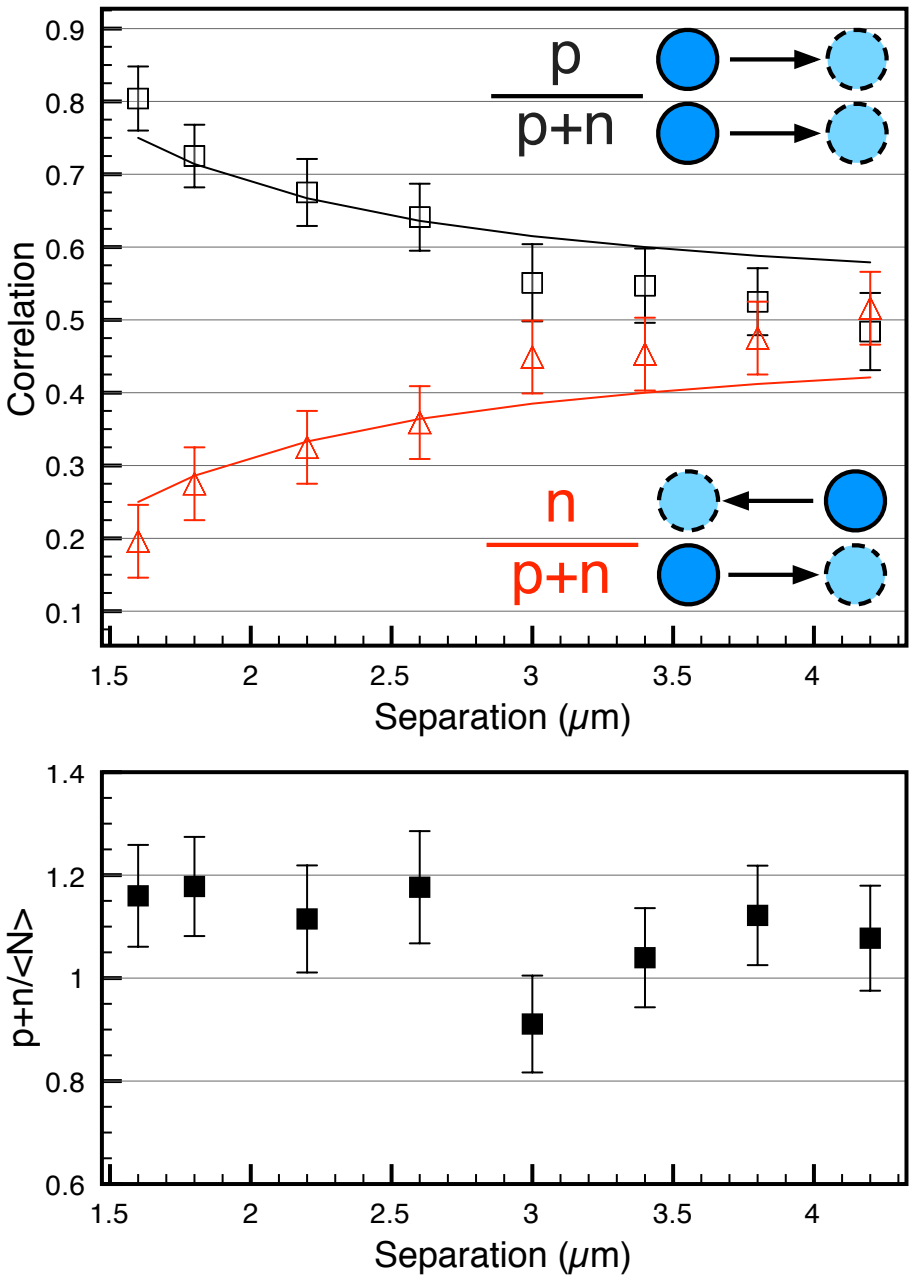

Figure 3.8: (a) Probability of coincidences over a range of system separations, s. p and n coincidences are defined by the inset. Coincident events are counted as described in the text and presented as black □ for p and red △ for n. Data is normalised by $p+n$. The solid lines represent the splitting in p and n assuming a linear dependence on hydrodynamic coupling with a strength of $3a/4s$. (b) The total counted coincidences at each system separation normalised by the expected number, $\langle N \rangle$, (Eq. 3.11) with an error of $\pm\sqrt{p+n}/\langle N \rangle$.

IV
Optical shield

The viscosity of a fluid can be measured by tracking the motion of a suspended micron-sized particle trapped by optical tweezers. However, when the number of particles is high, additional particles entering the trap compromise the tracking procedure and degrade the accuracy of the measurement.

In a typical optical tweezers (OT) set up, the gradient force created by tightly focused lasers traps particles [5] of a colloidal solution. OT have been used in a host of experiments across many disciplines as varied as biology [18], micro fabrication [73], and colloidal science [28]. In each of these areas there is, to varying degrees, a requirement to control freely diffusing particles of the colloid. For example, Hoogenboom *et al.* [73] spatially separated particles in a reservoir, from which they were transported to a substrate using OT, thus demonstrating a technique for micro fabrication. Another application of OT is microrheology [74], where it is possible to measure the viscoelasticity of the surrounding fluid by monitoring the Brownian motion of trapped particles [12, 37]. This technique is relevant to microfluidics [32], and biology, where changes in viscosity arise from biological processes [75].

In microrheology, it is necessary to limit the number of freely diffusing particles in the sample where the measurement is taking place, otherwise, these particles can diffuse into the trap and compromise the tracking procedure. Long measurements are needed for good statistics. Local heating of the sample can also create convection currents which draws additional particles to the optical trap [76]. Controlling the number of particles or contaminants is not always easy, especially when measurements are made in turbid environments.

The duration of an experiment depends on the time scales of interest. In the case of simple, Newtonian fluids (i.e., fluid with a constant viscosity), the size of the particle (along with temperature) determines the diffusion rate. The diffusion, D, is defined by the Mean Square Displacement (MSD) of a particle's trajectory, MSD $= Dt$. For a non-Newtonian fluid the same equation is used, but now D becomes a function of time. Each

point in the MSD is made up of the average of many displacements within a single trajectory. For example, if we record a trajectory for 10 s, we have 10 independent measurements of 1 s displacements (provided the acquisition is faster than 1 Hz). These displacements are averaged to obtain the 1 s lag-time point of the MSD. For errors around 1%, we need of order 1000 independent measurements (the error in mean is given by $\sigma/\sqrt{N}$). Continuing the above example, if the acquisition frequency is much faster than 1 Hz then there are many 1 s displacements (e.g. from 0.1 s to 1.1 s) however these displacements are no longer independent. These points can still be used, however, care must be taken when prescribing errors to the averaged data. In a simulation with 10^6 random steps, an average error of 10% for a lag-time of 10^4 steps was found [39]. This suggests that calculating these additional (non-independent) displacements does not improve the error of the measurement. ei In this chapter, I present a method of optically shielding the region of the sample where the measurement is taking place. Holographic OT [17] use spatial light modulators (SLMs) to manipulate many trapped objects independently. In addition they can be used to create unusual beams, e.g., those with azimuthal phase structure. Here, a Laguerre-Gaussian (LG) beam [42] is used to create an additional annular ring of light around the trap. With an azimuthal index of $\ell = 40$, the numerical aperture (NA) is effectively reduced so that the scattering forces are stronger than the gradient force. We find that particles in the ring are propelled in the beam propagation direction, away from the trap. There are many ways to make a ring of intensity (for example, the Gerchberg Saxton approach [77]), however, LG beams are ideal because they have zero on axis intensity along the entire length of the beam. Previous work has been done using LG beams, arrays of Airy beams and inverted axicon beams to clear paths through turbid samples [41, 78]. Here, we choose the simplicity of encoding the trap and an LG shield beam on the same SLM and find a considerable increase in the length of time we were able to successfully measure viscosity.

For this work, I acknowledge contributions from Dr Manlio Tassieri for help interpreting the results. This work led to a 2012 publication in Optics Express [79]

4.1 Measuring viscosity with optical tweezers

In a viscous fluid, the thermal fluctuations cause displacement of a trapped particle away from the centre of the potential well created by OT. The motion of the particle can be modelled as a thermally driven, over damped oscillator in a potential well, given in one dimension by,

$$E(x) = \frac{1}{2}\kappa\langle(x)^2\rangle, \tag{4.1}$$

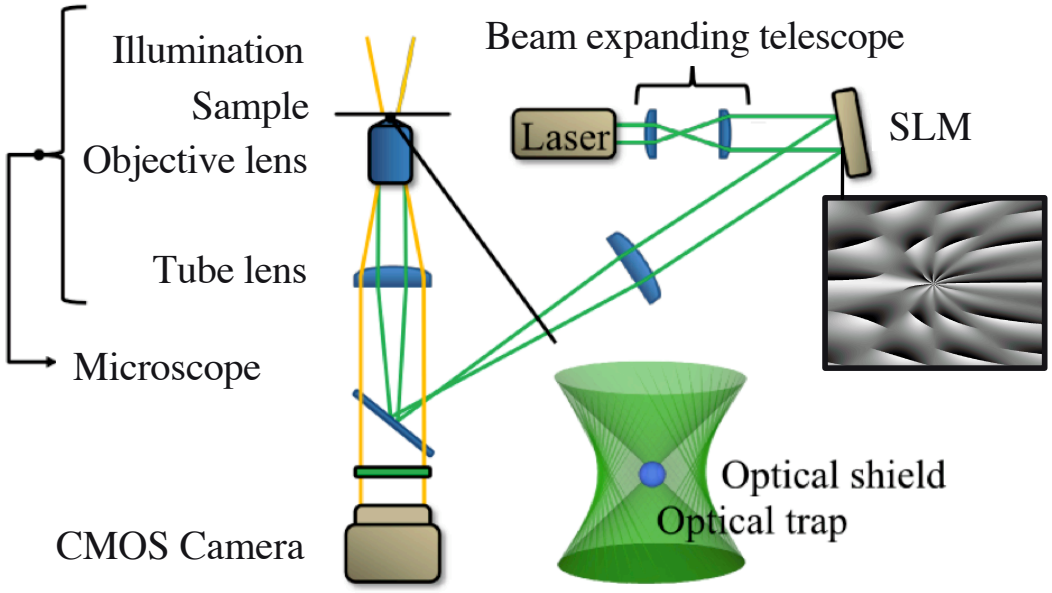

Figure 4.1: Holographic optical tweezers. Laser beam is diffracted by the SLM which is imaged onto the back aperture of the microscope objective. A diffraction pattern (represented on the right) is displayed on the SLM to create a trapping beam surrounded by a LG beam (inset shows a not to scale illustration of this arrangement, with a particle placed in the trapping beam). The trapping plane is imaged onto a high speed camera.

where κ is the trap stiffness and x is the particle position from the centre of the trap. The trap stiffness depends on factors such as laser power and the refractive index difference between fluid and particle. The restoring force exerted by the OT on the particle is expressed as $F = -\nabla E(x) = -\kappa x$, which is linearly proportional to the bead position for displacements smaller than ~ 0.8 times the bead radius, a [6]. The trap stiffness, κ, can be calculated from the equipartition principle, i.e., $\frac{1}{2}k_BT = \frac{1}{2}\kappa\langle x^2\rangle$, where k_B is the Boltzmann constant, T is the temperature and $\langle x^2\rangle$ is the time–independent variance of the bead position from the trap centre. For a Newtonian fluid, the particle's motion can be described by means of a Langevin equation [74, 38], with the inertia term typically being neglected for frequencies up to MHz, as described in Chapter 1. At thermal equilibrium, the Langevin equation can be solved in terms of the normalised position autocorrelation function [34], giving,

$$A(\tau) \rightarrow \exp\left(-\omega_c\tau\right), \tag{4.2}$$

where $\omega_c = \kappa/(6\pi\eta a)$ is the characteristic relaxation rate of the system. Once κ and a are known, this can be used to determine viscosity, $\eta = \kappa/(6\pi a\omega_c)$, Fig. 4.2. Note that

Eq. (4.1) and Eq. (4.2) are applicable for each Cartesian axis provided that the potential is quadratic. Other methods using optical tweezers to measure viscosity exist, however, as we are testing a new procedure using a Newtonian fluid, Eq. (4.2) is the most appropriate for our purposes.

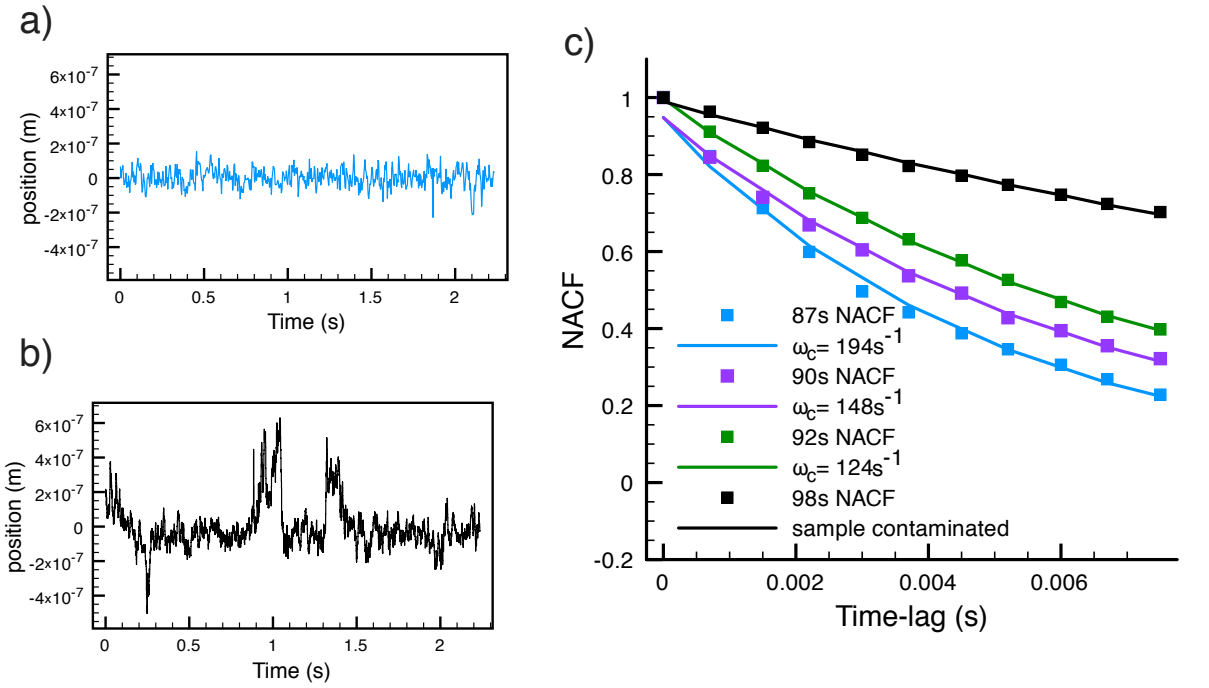

Figure 4.2: a) shows the position trace of a block of 2.2 s data of a particle held in optical tweezers. The acquisition rate is 1.34 kHz. b) Later in the same experiment, with errors in the tracking due to contamination of the trap. c) shows the normalised autocorrelation function (NACF) calculated from 2.2 s blocks of data. As this is a relatively small amount of data, only the first few points are calculated, and a single exponential is fitted. ω_c, the decay rate, is calculated from the fit and used to calculate viscosity as described in the text. The black shows the erroneous measurement corresponding to sample contamination.

Measuring viscosity with optical tweezers has also been done through rotation of the particle [80, 37]. Rotation has the advantage of being less affected by nearby surfaces. To make the particle spin, it is usual to use birefringent spheres such as vaterite or calcite crystals and a circularly polarised trapping beam. The particle then acts like a quarter wave plate, converting some of the light's circular polarisation into linear. Circular polarisation is associated with spin angular momentum, a quantity which must be conserved by the rotation of the particle. Fortunately, the change in polarisation of the light can be measured and the rotation of the particle can be inferred from this, meaning no involved particle tracking is required.

Another method to determine viscosity is by observing phase lag whilst applying a

periodic force [75]. This periodic force can be applied quickly, meaning large areas of a sample can be mapped. The disadvantage is that the fluid properties are only probed at one frequency (i.e., the frequency of the periodic force), compared with a Brownian force which has power across the frequency spectrum.

Relying soley on Brownian motion does give the response for all frequencies, but low frequencies (corresponding to large motions) take a long time to be explored. Moreover, the presence of an optical trap acts as a cut off to low frequency motion. Wideband microrheology has been developed to access a broader frequency range, where high frequencies and low frequencies are pieced together from motion inside an optical trap and the relaxation of the particle back to equilibrium during stepping motion, respectively [81].

Broadband microrheology is another technique, and shares some similarities with wideband microrheology. Instead of flipping the trap position, a near instantaneous flow is applied to the trapped sphere. The frequency response is given by the combination of diffusion within a stationary setting and the response to the applied flow [38]. It is worth noting that neither of these approaches give a direct measurement of the creep compliance of the fluid, which requires an instantaneous, constant force to be applied to the fluid. The compliance is useful as it is directly converted to the viscoelastic properties of the fluid [82]. In the case of wideband microrheology, the force is approximately proportional to the displacement from the trap centre. In broadband microrheology, a constant flow is applied, which only corresponds to constant force in the case of a Newtonian fluid.

To obtain the viscoelastic response over the full experimentally accessible frequency range, a data analysis procedure has been developed, which involves interpolating the autocorrelation of a trapped bead [39]. This procedure involves two steps, first the autocorrelation is calculated from experimental position data. As is the case for the MSD, the long lag times in the autocorrelation are more susceptible to noise, on account of them having fewer independent measurements. The result is that, at long lag-time, the autocorrelation has oscillation artefacts due to long time correlations which, owing to the finite length of the experiment, have not averaged to zero. The simplest approach to removing these points is to logarithmically sample the autocorrelation, then interpolate the samples points. This approach was used successfully in various bioengineering applications [83, 84, 85].

4.2 Experiment

The OT system (Fig. 4.1) is built around a Zeiss inverted microscope using a 100×, 1.3 NA, objective lens. The optical fields are created using a 532 nm laser (Laser Quantum Ltd., excel). The beam is expanded through a telescope, then incident on a SLM

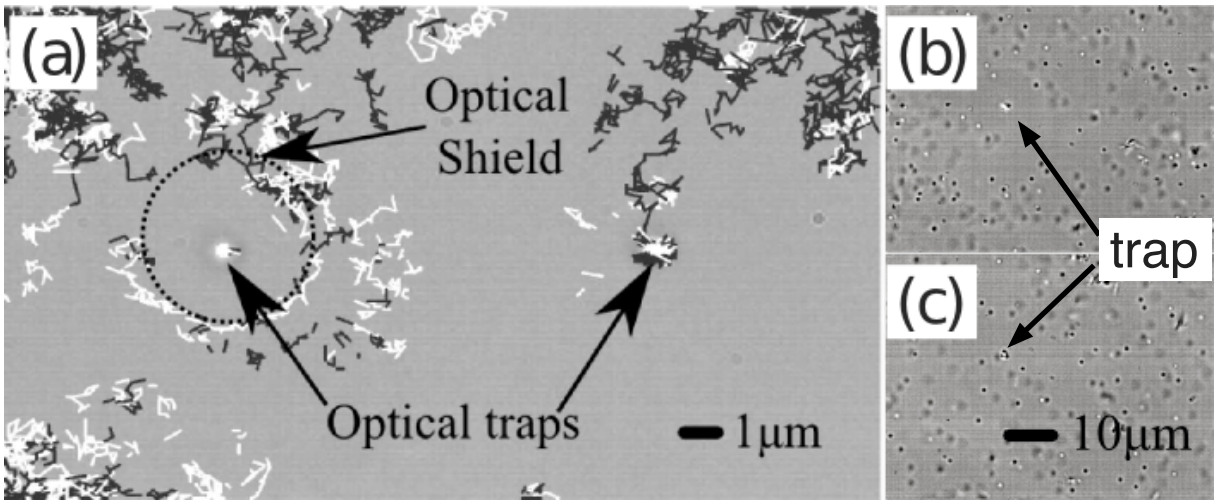

Figure 4.3: (a) Tracked particle trajectories superimposed on an image of the experiment. White lines indicate particles in or just above the focal plane, which appear brighter in the image compared to the background. Dark lines indicate particles below the focal plane, which appear darker. The tracks appear and disappear as particles go in and out of focus. On the left is an optical trap surrounded by a optical shield, on the right is an unshielded trap. The tracks of the freely diffusing particles can be seen to enter the right hand, unshielded trap, whereas the optical shield around the left hand trap prevents such an event. (b) and (c) are images of the sample at the time of the measurements with and without a shield respectively.

(Hamamatsu X8267). Using software written in National Instruments LabVIEW [66], a phase modulation is calculated by summing a grating (for diffraction angle) and lens (for defocus). It is also possible to create LG beams simply by adding a phase modulation that is proportional to the azimuthal angle around the centre of the beam. The optical shield used here consists of such a beam with $\ell = 40$, which focuses to a ring around $4\,\mu$m in diameter, and Rayleigh range $\sim 3\,\mu$m. The diffracted beams then pass through a 4f imaging system, such that the SLM is imaged onto the back focal plane of the objective lens. The objective lens tightly focuses the beams creating optical fields inside the sample, Fig. 4.3. The sample is a microscope slide with a concave recess, prepared with a solution of spherical silica particles ($a = 0.4\,\mu$m, Bangs Laboratories) in de-ionised, distilled water and sealed with a coverslip and secured with UV curing glue. These particles tend to sediment just above the coverslip, however, we observed that thermal energy is sufficient for these particles to diffuse up to $\sim 20\,\mu$m above the coverslip. Within this layer, the concentration of spheres was much higher than a typical OT sample, Fig. 4.3 b) and c). The trapping plane is then imaged on to a high speed CMOS camera (Prosilica GC650). Using a centre of mass algorithm and reduced region of interest, we can track particle positions at 1.34 kHz, sufficient to measure the autocorrelation time of the trapped particle [35].

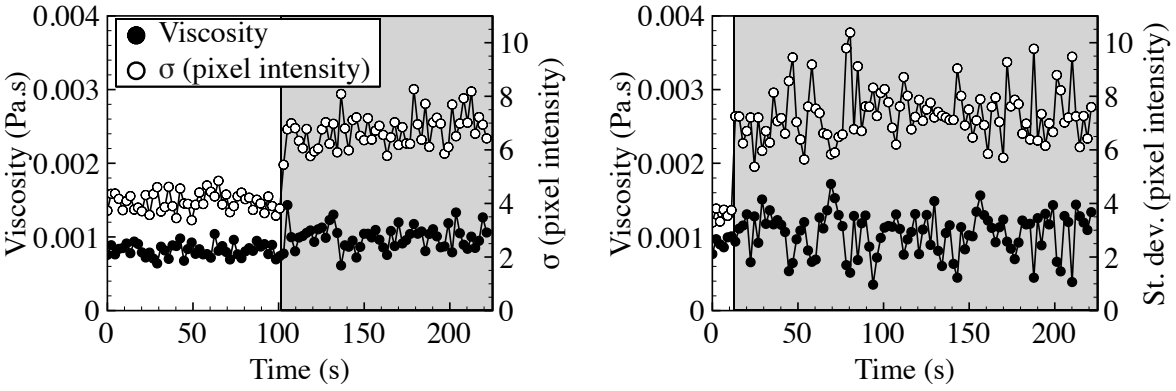

Figure 4.4: Two examples of viscosity measurements (• points, on the left y-axis) against time, together with the standard deviation, σ, of pixel intensity (∘ points, on the right y-axis). The left plot shows results taken with the shield on. Here, after around 100 seconds, the standard deviation of pixel intensity jumps to a higher value, indicating the arrival of another particle in the optical trap. The measurement of viscosity can also be seen to be altered, though not as considerably. The right plot shows results where no shield is used. The viscosity is expected to be 0.89 mPa.s.

The experiment is automated to take 250 measurements with a shield, then the system is reconfigured to take 250 measurements without a shield. Each measurement involves tracking a trapped particle for approximately 3 minutes 40 seconds, i.e., 3×10^5 data points taken at 1.34 kHz. In the configuration with a shield, ~ 50 mW of laser radiation is used with the optical power of the shield weighted approximately twice that of the power in the trap. Without a shield, the laser power is reduced to give a similar trap strength.

In both configurations, an optical trap is created 5 μm above the coverslip in a sample of highly concentrated particles (Fig. 4.3(b) and (c)). The software then waits for a particle to diffuse into the trap. This event can be identified computationally by analysing images recorded by the camera of a small region featuring the trap. Initially there may be no particle inside the trap, so the average intensity of the brightest pixel is equal to that of the background, with only camera noise contributing to fluctuations. The standard deviation of the brightest pixel value is then small. When a particle diffuses into the empty trap, this standard deviation increases (Fig. 4.4) as the vibrations of the particle significantly change the brightness of the image. Therefore, we use this criterion (standard deviation of brightest pixel) to identify the presence of a particle. If the standard deviation increases further (typically because two or more particles have diffused into the trap) the trap is switched off, and the software waits 30 seconds before restarting. If the particle meets the criterion, then, in the case using a shield, the shield is switched on. In the case

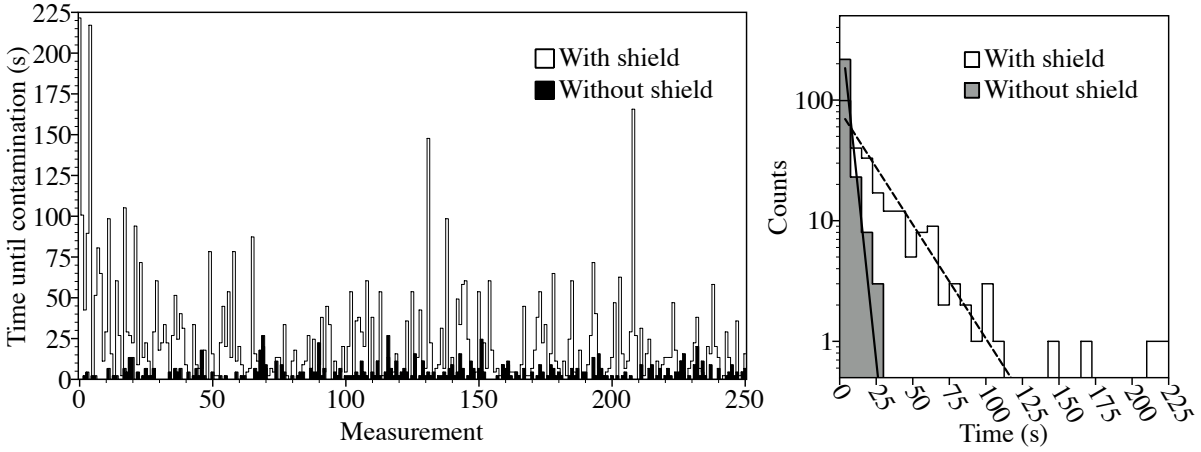

Figure 4.5: Left: the length of time of successfully measuring viscosity in 500 attempts. 250 white bars indicate the use of an optical shield, whereas the 250 black bars indicated no shield was used. Right: A histogram showing the number of times the arrival of a particle in the optical trap occurred in time bins of length 7.5 seconds. The exponential fits are calculated from the mean time until contamination.

without a shield, no change is made to the hologram. 3×10^5 position data and pixel intensities are saved to file for later analysis. The trap then switches off for 30 seconds and the experiment repeats, allowing many measurements to be taken with different particles. Figure 4.3(a) shows tracks of diffusing particles, two of which are trapped in optical traps. The left hand of these traps is surrounded by an optical shield which is seen to deflect material from the trap.

4.2.1 Results

In order to obtain time-resolved viscosity information, the 3×10^5 position data are divided into 100 blocks, each 2.2 seconds (Fig. 4.4). Assuming a temperature of 25°C, we calculate the trap stiffness to be around $1.3\,\mu\mathrm{Nm}^{-1}$. For each block, an autocorrelation is calculated, yielding the characteristic decay rate of around $\omega_c = 200\,\mathrm{s}^{-1}$. In our case, 2.2 seconds of data gives a measured fluctuation in the decay rate of 12% causing our calculation of viscosity to also fluctuate. The uncertainty in particle size (in our case 10%) gives a systematic error in the viscosity measurement. We found an average viscosity of $(0.88 \pm 0.10)\,\mathrm{mPa.s}$ with shield, and $(0.88 \pm 0.24)\,\mathrm{mPa.s}$ without shield, where standard deviation is larger in the case without a shield as more of the data is excluded due to the arrival of contaminating particles. These results are in good agreement with each other, and the expected value of 0.89 mPa.s. This result assures that the presence of the shield does not effect the measurement of viscosity.

We determine the arrival time of a contaminating particle as the time when the standard deviation of the maximum pixel intensity exceeds a predetermined level. Figure 4.5 (left) is a bar chart detailing the arrival time for every measurement. Figure 4.5 (right) is a histogram of these arrival times, showing an improvement in the length of time the trap stayed clear of other particles when the shield is used. The mean arrival times with and without a shield are 23 seconds and 3.8 seconds respectively. The effect of a contaminating particle typically increases the viscosity measurement by $\sim 25\%$.

4.3 Discussion

If the particles are more difficult to trap than standard dielectric spheres, the scattering force provided by the optical shield is greater, and the shield should prove more effective. If the scattering force on a particle is less than the particle's weight, the particle will not be cleared from the region. This can be overcome with increased laser power or, if possible, reducing the size of particles used. Focusing the shield and trap 5 μm above the coverslip helped prevent particles entering the trap from below, and is far enough from the coverslip that hydrodynamic influences are small. Using 532 nm laser light helps reduce the effect of laser heating on the sample [76]. Reference [41] outlines some difficulties of using LG beams to clear paths through turbid media. The experimental requirements differ in this work as only a small volume around the trap is required to be kept clear, rather than a continuous path. We also have no requirement to clear the area inside the annulus, which is arranged to be clear at the start of the experiment.

In conclusion, we have shown that introducing an LG beam centred around an optical trap reduces the probability that freely diffusing material will enter that trap. We have devised a procedure for detecting such an event and find nearly an order of magnitude increase in arrival time of contaminates compared to standard procedures. We use the approach to measure viscosity in a turbid sample and obtain the expected value. With the simplicity of generating the LG beam with holographic OT, we foresee that this approach may assist measurements in samples which involve a plethora of diffusing material.

V
Rotational Doppler velocimetry

Beyond the straight-forward use of the Doppler shift in the measurement of the linear velocity of an approaching particle, it is also possible to exploit the Doppler shift to measure its transverse velocity, v. Key to this latter application is that an illuminating beam diffusely scatters from the translating object. Any light scattered away from the angle of reflection undergoes a change in its transverse momentum. Scattered light detected at such an angle has a frequency shift determined by the transverse velocity of the scattering surface. For example, if the particle is illuminated at incident angle α and viewed at normal incidence (as shown in Fig. 5.2a), then the Doppler shift is reduced from the linear case and is given by $\Delta\omega = \sin\alpha\ k_o v$, where $k_o = 2\pi/\lambda$. If two beams are incident at $\pm\alpha$, the Doppler shifts are in opposite directions and interference between the two beams gives an intensity modulation in the back-scattered light of $\omega_{mod} = 2|\Delta\omega| = 2\sin|\alpha|\ k_o v$. This technique is commonly referred to as Doppler velocimetry [86].

A rotational analogue to Doppler velocimetry was recently demonstrated for light scattered from a spinning disc [87] and also considered for a particle moving through a structured light field [88]. In addition to spin angular momentum (which has also been used to probe rotation [89]), light beams can also carry an Orbital Angular Momentum (OAM) [42]. The helical phase fronts result in a Poynting vector that is skewed with respect to the beam axis by an angle $\beta = \sin^{-1}(\ell/k_o r)$, where r is the radius from the beam axis [90]. In an analogous way to the translational Doppler shift, an OAM beam experiences a frequency shift when scattered from a rotating surface. In the rotational case, the difference in illumination and viewing angles arises from the skewed Poynting vector around the beam axis (see Fig. 5.2b). This means that any light scattered back along the beam axis from a rotating object will be shifted in frequency by,

$$\begin{aligned} \Delta\omega &= \sin\beta\ k_o v \\ &= \ell\Omega\ , \end{aligned} \tag{5.1}$$

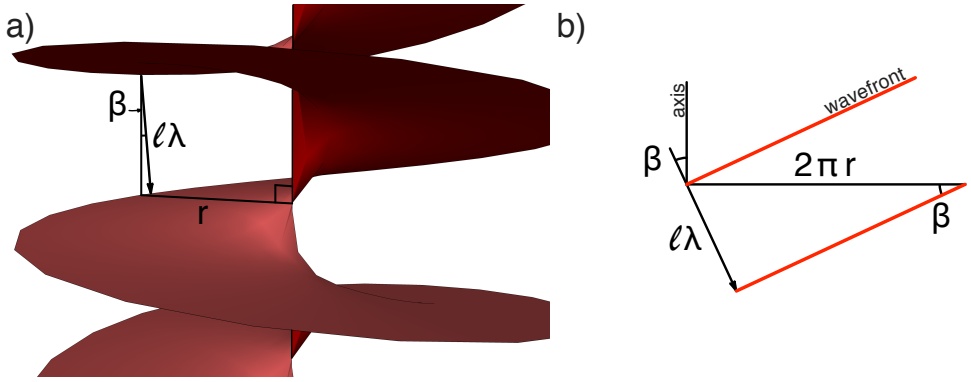

Figure 5.1: a) The angle β is the angle between the normal to the wavefront and the beam axis, shown here for the case of $\ell = 1$. The distance between wavefronts along this direction is $\ell\lambda$. b) Radial unwrapping of the wavefront shows that $\sin\beta = \ell\lambda/2\pi r$.

where $v = \Omega r$. This is the same expression that describes the frequency shift when a helically-phased beam is rotated about its own axis [91, 92]. Similarly to doppler velocimetry, if two beams are used with opposite values of ℓ, the frequency shifts are in opposite directions and the two components interfere to give an intensity modulation in the on-axis scattered light of,

$$\begin{aligned} \omega_{mod} &= 2|\Delta\omega| \\ &= 2|\ell|\Omega \ . \end{aligned} \tag{5.2}$$

In this chapter I demonstrate the rotational Doppler shift from micron-sized birefringent calcite particles trapped and spinning in a circularly polarised optical trap [93]. We are exploring the fundamental limits of the technique, as the particle size is of the same scale as the diffraction limited beam waist. In this case the rotational Doppler effect arises from anisotropy in particle shape as well as surface roughness. The particle is also subject to Brownian motion, making the measurement of the effect more challenging. Nevertheless, by taking these factors into account, I show that illumination of the particle with two beams of opposite OAM can be used to unambiguously recover information on the particle's rotation rate. This measurement is independent of intensity fluctuations arising from linear motions and is performed using just a single photodetector, making it applicable to the measurement of high angular velocities.

My individual contribution to this work was writing the data acquisition software, development of the experiment procedure, building and designing the OAM attachment to the optical tweezer system, taking data and interpreting the results. Dr David Phillips and Dr Graham Gibson contributed to interpretation of results, data acquisition, analysis,

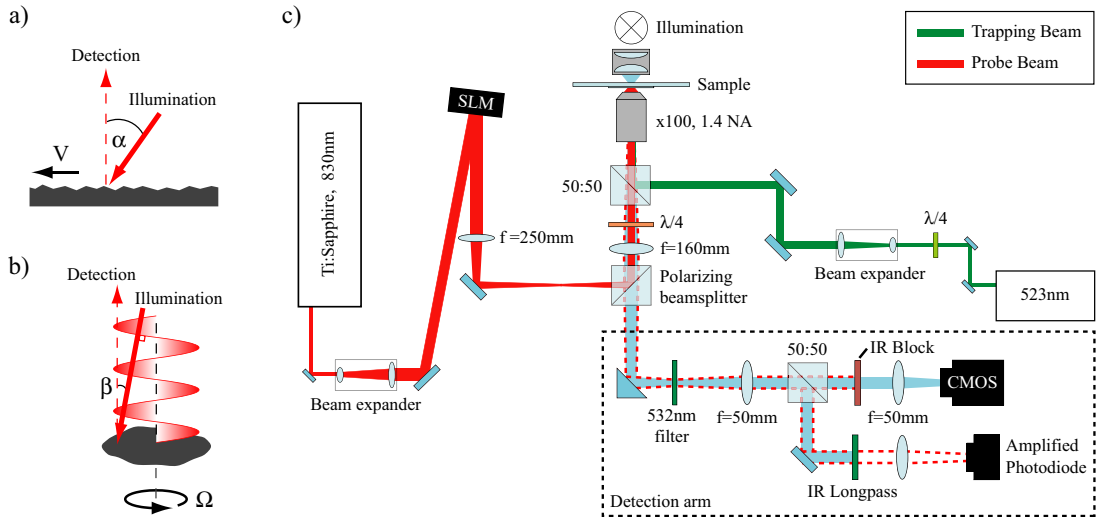

Figure 5.2: a) Transverse Doppler effect. The frequency shift of the back-scattered light is determined by the transverse velocity of the scattering surface and angle between the illumination and detection axis. b) Rotational Doppler effect. Helical phase fronts of a beam containing OAM result in a difference in the illumination and detection angles. Here the frequency shift is determined by the rotational velocity of the object and the OAM mode. c) Experimental setup. The system is adapted from that described in [35]. A solid state laser (Laser Quantum, Opus) provides a trapping beam, which is circularly polarised using a quarter waveplate. A titanium sapphire laser (M^2, SolsTiS) provides a probe beam. The probe beam is shaped using an SLM (Boulder Nonlinear Systems, XY-Series), and focussed into the sample to the same plane as the calcite particle, with the optical axis collinear with the rotation axis of the particle. In the detection arm a high-speed CMOS camera (Dalsa Genie, HM1024) is used to observe the trapped particle and an amplified silicon photodetector (Thorlabs, PDA36A-EC) monitors the intensity modulation of probe beam light that is back-scattered from the particle (shown in dashed red). A 532 nm block filter and an IR long pass filter prevents any unwanted light from reaching the photodetector.

and helped build the experiment. Prof. S. Barnett developed the analytical model of the experiment.

5.1 Apparatus

Figure 5.2 shows a schematic of the experiment. It consists of an inverted microscope integrated with a single beam circularly polarised optical tweezers (shown in green) to trap and spin birefringent calcite particles. A probe beam (shown in red) is also coupled into the microscope. The probe beam is shaped holographically [94] into two overlapping beams carrying opposite handedness of OAM. These interfere to produce a "petal" shaped intensity pattern, where the number of petals (and therefore rotational symmetry) is given

by $2|\ell|$ [95]. Figure 5.3a shows example of the intensity cross section through these patterns for different values of ℓ. Light from the probe beam is scattered from the rotating particle back onto the optical axis, collected by the objective lens and imaged onto a photodetector.

A laser power of 50 mW was sufficient to optically trap and to spin a micron-sized calcite particle at a rate between 20 and 30 Hz. When trapped, the particle experiences an optical torque from the circularly polarized trapping beam, hydrodynamic drag from the surrounding fluid, and a stochastic torque due to Brownian motion. The balance of these effects results in the particle rotation rate fluctuating a small amount about its mean value. We independently measured the rotation rate of the particle by tracking its orientation from a sequence of high-speed camera images (10,000 images recorded at 2786 Hz, sample images shown in Fig. 5.3b), using the methods described in [96]. This method of video particle tracking converts the 8-bit images obtained from the camera in to a binary image through thresholding. The centre of mass of these pixels gives the position of the particle. The orientation of the particle is calculated from the inertia tensor. Both terms "mass," and "inertia," are meant analogously, and are simply calculated from the intensity of the pixels in the image of the object. The eigenvectors of this tensor are parallel to the principal axes of the particle. The mean rotation rate was calculated from the average time for one cycle (based on 100 cycles). These cycles occurred at 25.6 Hz, and found to vary by a standard deviation of 1.1 Hz owing to stochastic effects. These calculations were preformed by Dr David Phillips.

The particle was then illuminated with the probe beam, the total optical power of which was reduced to a level such that it had a negligible effect on the rotation rate, estimated to be less than 1 mW reaching the sample. The calcite particle was raised by approximately 20 μm above the sample bottom to reduce the amount of probe beam light scattered from the coverglass to the detector. Figure 5.3c shows a segment of the time varying signal measured by the photodetector for an $\ell = \pm 1$ probe beam. 30 data runs, each consisting of 20,000 measurements at a sampling rate of 20 kHz, were recorded for $\ell = 0$, $\ell = \pm 1$, $\ell = \pm 2$ and $\ell = \pm 3$. In each case the data was Fourier transformed to produce a power spectrum, with the average power spectrum for each mode ℓ shown in Fig. 5.4.

5.2 Results

The average power spectra show growth in peaks corresponding to $2|\ell|\Omega$ (marked with arrows), as found for the case of light scattered from a spinning disk [87]. The power spectra also feature frequencies other than that of the rotational Doppler modulation frequency, because the photodetector signal is not purely sinusoidal. There are no other

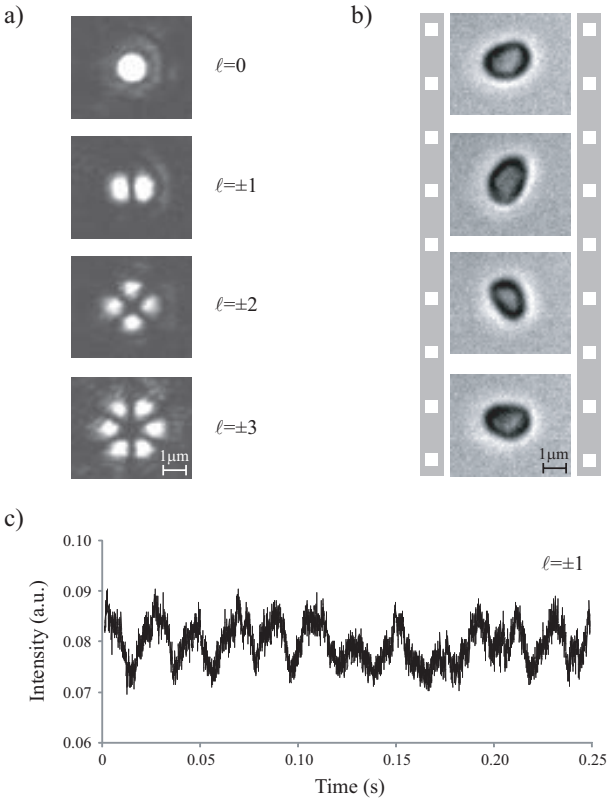

Figure 5.3: a) "Petal" shaped intensity patterns of the probe beams when focussed on the coverglass. b) Selected images of the calcite particle rotating in the optical trap. c) A small segment of the time varying signal measured by the photodetector for an $\ell = \pm 1$ probe beam. The beat frequency at $2|\ell|\Omega$ can be seen (period $\sim 0.02\,\mathrm{s}$), along with noise introduced by Brownian motion.

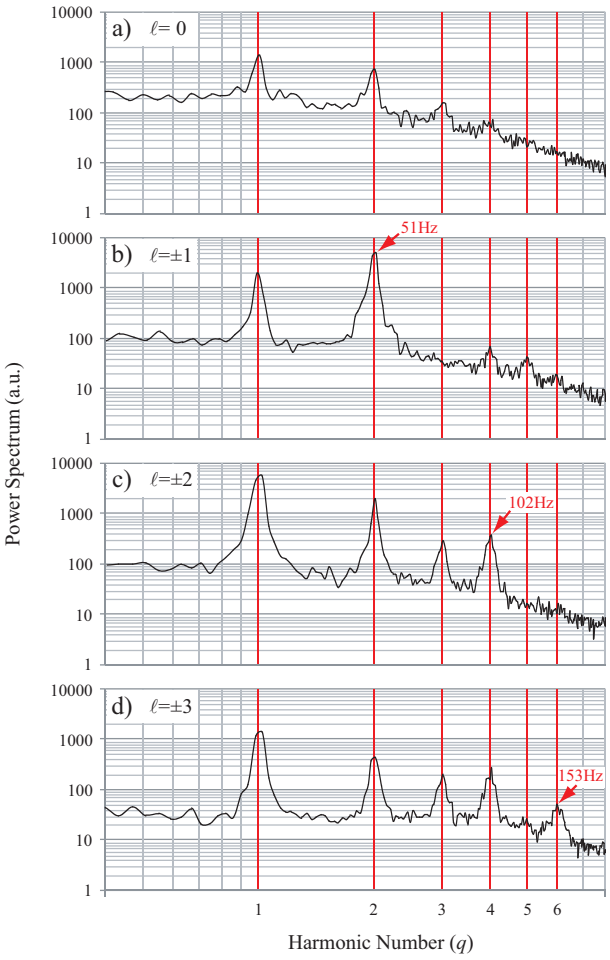

Figure 5.4: Power spectra for probe beams consisting of $\ell = 0$, ± 1, ± 2 and ± 3. The fundamental rotation frequencies for a), b), c) and d) are 23.9, 25.3, 25.5 and 25.5 Hz respectively, which compares well with the rotation rate determined using video tracking. Arrows indicate frequencies of $2|\ell|$ times the fundamental. The high on-axis intensity of the $\ell = 0$ probe beam results in a slight reduction in the rotation rate of the particle.

resonant signals present, i.e., all pronounced peaks in the power spectra are harmonics of the particle's fundamental rotation rate, due to the fact that our system is heavily over damped. However, it is the scaling of the harmonic at $2|\ell|\Omega$ with the OAM content of the probe beam that provides a signature of rotational motion.

Periodic time varying intensity modulations can be interpreted in two equivalent ways: in the time domain, intensity modulation is a consequence of the scattering object rotating through a light field of spatially varying intensity; in the frequency domain, intensity modulation can be interpreted as a beat frequency due to the interference of light beams of different frequency. The presence of harmonics at frequencies other than $2|\ell|\Omega$ (and in particular the presence of the lower harmonics we observe) is predicted by considering the situation in the time domain (a model developed by Prof. Stephen Barnet). This takes into account the influence of alignment, the particle's geometry and how it scatters light in the presence of Brownian motion.

First consider a particle rotating about a fixed axis. We take the particle rotation axis as the origin, which is not necessarily perfectly coincident with the centre of the illuminating light. We can expand the complex amplitude of the light illuminating the particle, u, as a Fourier series in cylindrical coordinates: $u(r,\phi) = \sum_{n=0}^{\infty} u_n(r)e^{in\phi}$, where r is the radial coordinate, ϕ is angular coordinate, and n the mode number of the expansion. The particle will scatter this light in a spatially dependent manner. We can express the scattered field as $s(r,\phi,t) = u(r,\phi)f(r,\varphi(t))$, where f is a function that depends upon the properties of the scatterer, such as its geometry and reflectivity. Function f also encodes the orientation of the particle at time t, which is given by $\varphi(t) = \phi_0 - \Omega t + \theta(t)$. Here ϕ_0 is the initial orientation of the particle, Ω is the average angular velocity as above, and $\theta(t)$ is a zero-average fluctuating angle, driven by Brownian motion. We can also expand f as a Fourier series in cylindrical coordinates, $f(r,\phi_0 - \Omega t + \theta t) = \sum_{m=0}^{\infty} f_m(r)e^{im[\phi_0 - \Omega t + \theta(t)]}$, where m is the mode number of the expansion. The measured photocurrent, $i(t)$, is proportional to the intensity of the backscattered light integrated over the on-axis detector area A (here we assume $A(r) = 1$ for a radius r less than the radius of the detector, and 0 otherwise). Therefore, the expected frequency spectrum, $S_\ell(\nu)$, of the detector signal for light scattered by a particle illuminated with a probe beam of dominant modes $\pm\ell$, can be found from the Fourier transform of the autocorrelation function of $i(t)$, using a simple diffusion model for Brownian motion [97]. This results in

$$S_\ell(\nu) = 2T\sum_{q=0}^{\infty} |G(\ell,q)|^2 \left[\frac{2Dq^2}{(q\Omega-\nu)^2 + D^2q^4}\right], \tag{5.3}$$

where ν is the angular frequency of the power spectrum, T is the length of the measure-

ment, D is the rotational diffusion coefficient of the particle, and q is the azimuthal mode number of each expansion (equivalent to the harmonic number in Fig. 5.4). Equation 5.3 indicates that we can expect peaks in the power spectrum at harmonics of the rotation rate, as observed. $G(\ell, q)$ contains information about the angular Fourier components of the scatterer f, and of the illuminating beam u. It encodes the weighting of each harmonic: the greater the overlap integral between angular Fourier components of f and u, the greater the power in harmonics of those modes. Therefore, as would be expected, the shape of both the light field and the particle itself play a role in determining the spectra. By illuminating with beams carrying defined OAM modes ($\pm\ell$), we effectively boost the overlap integral between the particle and the light field at mode $|\ell|$. It is because of this that we observe a significant increase in the power in peaks at $2|\ell|\Omega$, shown in Figure 5.4. Any small aberrations in the illuminating probe beam, or slight misalignments between the rotation axis of the particle and the optical axis of the probe beam, act to broaden the Fourier components of u (when decomposed about an origin taken as the particle's rotation axis), and result in a spread of power into nearby harmonics. As the size of each peak is governed by the overlap integral of u and f, even a small amount of optical power into neighbouring modes can result in large peaks if the Fourier components of f at this mode have a large amplitude.

The analytical model also captures the effect of Brownian motion on the measured spectra, given by the Lorentzian term in square brackets in Eq. 5.3. As the particle rotates, it experiences a stochastic Brownian torque causing the rotation rate to fluctuate with a characteristic variance. These fluctuations cause a spread in each peak of the power spectrum, an effect that becomes increasingly severe for higher frequency harmonics, as can be seen from Eq. 5.3. The Lorentzian term modulates the shape of each harmonic so that the width increases as $\sim q^2$, and hence the height decreases as $\sim q^{-2}$. We clearly observe this effect in our measured spectra in Fig. 5.4. Therefore, even if power is spread symmetrically into adjacent harmonics, the resultant spectral density of the peaks is asymmetric, resulting in the magnitude of harmonics higher than $2|\ell|\Omega$ rapidly falling off. In our experiment, increasing ℓ also increases the diameter of the petal pattern, therefore reducing the overlap integral with the particle, and hence the power in the rotational Doppler shift peak.

The presence of the additional harmonics in the power spectra can also be understood in the frequency domain: a spread in the OAM mode content will result in a different Doppler shift for each mode, as each is incident from a different angle (see Eq. 5.3). Interference between all combinations of these frequencies results in the harmonics in the power spectrum.

5.3 Discussion

In summary, I have shown that it is possible to observe the rotational Doppler effect for a microscopic calcite particle spinning in an optical trap. As the OAM mode of the probe beam is increased, a significant increase in power in the harmonic at $2|\ell|\Omega$ was observed, corresponding to the rotational Doppler effect. It is the scaling of the harmonic at $2|\ell|\Omega$ with the OAM content of the probe beam that provides a signature of rotational motion. Also, how additional harmonics in the power spectra arise from any small misalignments between the beam and rotation axes, and the geometry of the particle itself has been shown. The measurement was performed on a particle of five orders of magnitude smaller in size than that used in the recent discovery of the rotational Doppler shift from a macroscale spinning disk [87]. The work shows the method to be robust to Brownian noise, and allows us to distinguish the rotation of the particle from the fluctuations arising from linear motions.

As these measurements are performed using a photodetector, the technique may also be important in discerning the high-frequency motion (beyond video tracking rates) of particles that are trapped at low pressure where translational resonances are also present, a field attracting significant interest due to its applications to mesoscale preparation of quantum state objects [98].

Part II

SLM Microscopy

VI
Image multiplexing

Optical microscopes are indispensable equipment in a range of laboratories [99]. Spatial Light Modulators (SLMs) offer remarkable control over a given light field. The combination of these instruments has led to the creation forms of new types of microscopy, and may well give rise to the next generation of microscopes [100]. SLMs (positioned in the Fourier plane of a sample) bring a flexibility to optical microscopy which would be difficult to realise with traditional techniques [43, 49, 45, 51, 101, 102, 103]. In this chapter, I build an SLM microscope which is compatible with various filters, such as spiral phase contrast [51], double-helix point spread functions [52], Spatial Light Interference Microscopy (SLIM) [48, 47], depth of field multiplexing [45, 104] and Gabor filters [105] amongst others [106, 107, 108].

Not only can different filters be applied without changing any hardware, but several filters can be applied at the same time to give multiple modalities simultaneously, offering a unique advantage over any traditional optical element.

In this chapter I acknowledge contributions from Dr Graham Gibson who designed and built the electronics for the system, as well as machining mechanical parts. This work was part of a publication in Optics Express [44].

6.1 Design

The inverted microscope design, Figs. 6.1 and 6.2, is similar to that of my groups recent work developing a compact optical tweezer system [109]. Focussing is achieved by moving the objective lens on a motorised stage (LS-50-M, ASI) which is mounted vertically within the aluminium frame of the microscope. Similarly, translation of the microscope sample is achieved using a motorised X-Y stage (MS-2000, ASI). Both these stages are controlled with the ASI MS-2000-WK Multi-Axis Stage Controller. High power red LEDs (LUXEON Rebel) coupled through the condenser using a short length of acrylic fibre (core diameter = 1.5 mm) provide the illumination. A critical illumination condenser

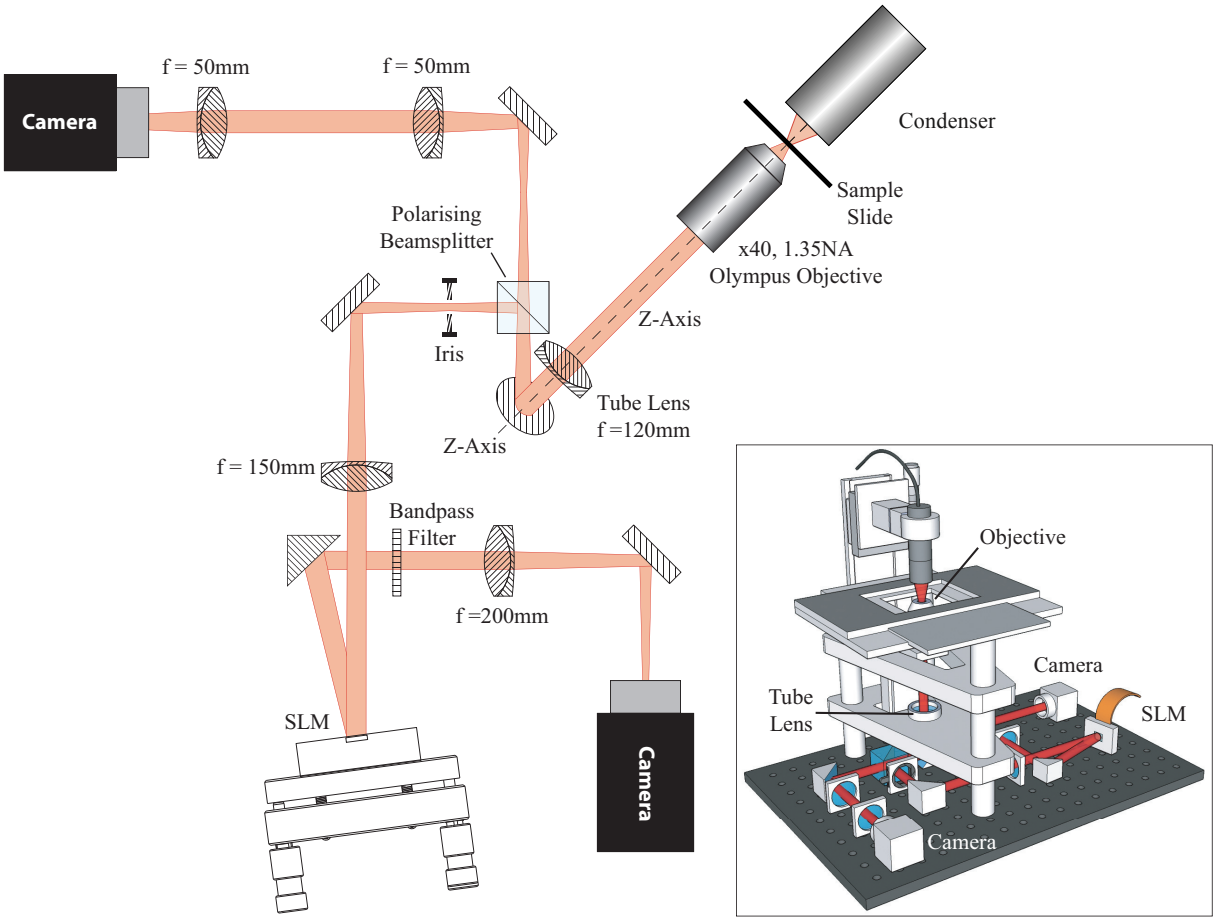

Figure 6.1: The configuration of our SLM microscope. Shown at 45° is the z-axis with the inverted microscope and illumination. The polarising beamsplitter is used so that the vertical polarisation of the light goes through the intermediate image iris and on to the SLM, where the Fourier filter is displayed. There is then a 10 nm bandpass filter so that dispersion is kept to a minimum in the sample images recorded by the camera. The horizontally polarised light forms the full image of the sample on the wide angle camera. Inset shows a 3D drawing of the system.

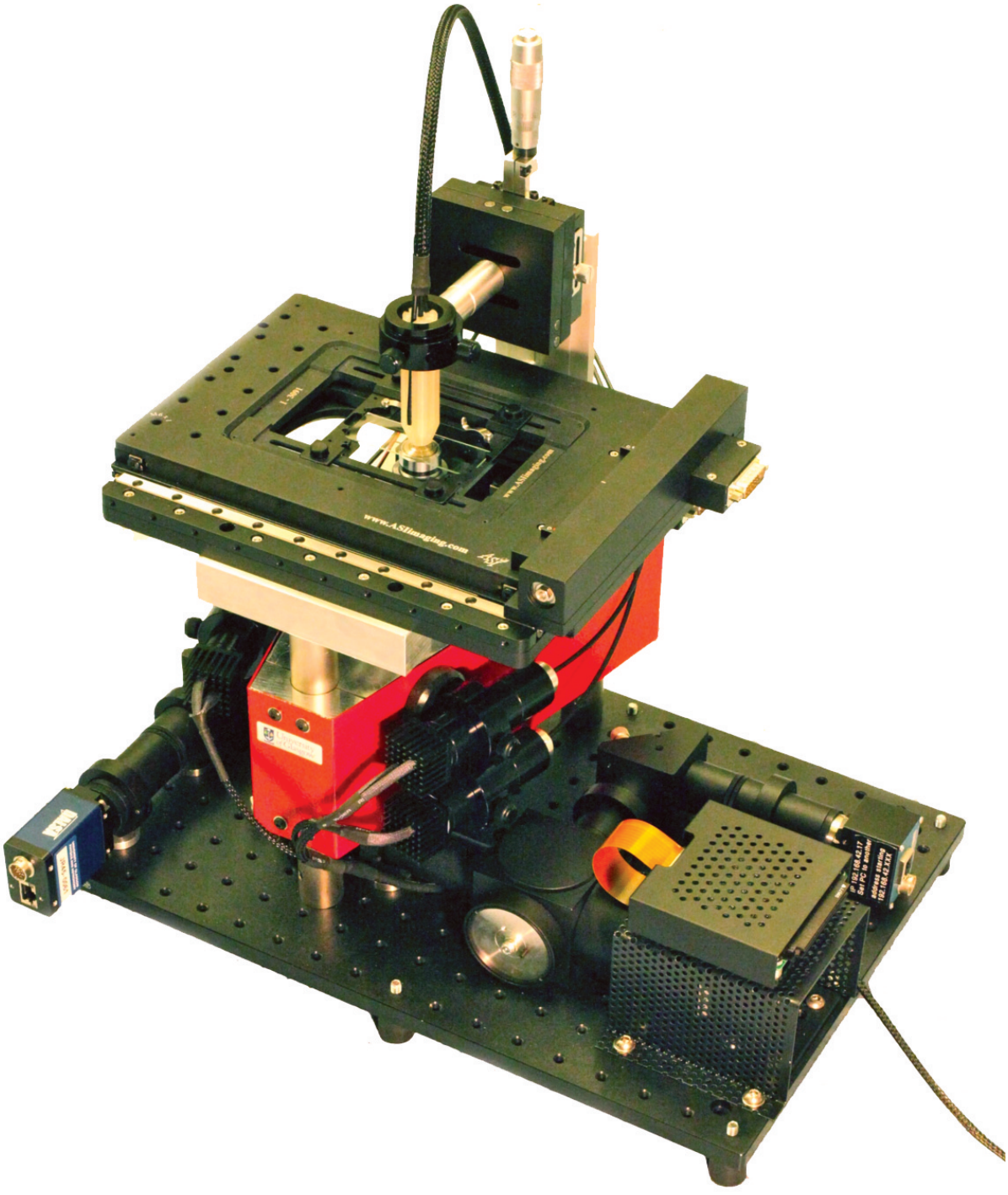

Figure 6.2: Photograph of the system. Visible is the optical fibre illumination, motorised stage, SLM and CMOS cameras. The footprint of the system is 45 cm × 30 cm, and the height is approximately 35 cm.

provides a uniform illumination of the sample. The output face of the fibre is imaged on to the sample, with a variable aperture to give brightness and spatial coherence control.

A polarising beamsplitter (PBS) splits the light between two arms, one containing a camera for wide field viewing of the sample and the other arm containing the SLM (Boulder Nonlinear Systems, X-Y Series (512×512 pixels)). The reflected light from the PBS is the correct polarisation for the SLM. In order to avoid problems with dispersion when illuminating the SLM using an LED, a bandpass interference filter (636 nm, 10 nm) is placed in the optical path after the SLM. The light diffracted from the SLM is imaged on to a second CMOS camera (Dalsa Genie, HM1020) which has a large sensor area, capable of imaging all diffracted images simultaneously. The overall optical configuration is similar to that of holographic optical tweezers [17, 4], where the diffraction from the SLM creates multiple, laterally displaced trapping beams. Here, the SLM now produces displaced images and, just as the trapping beams can be of different beam types, the images can correspond to different Fourier filter functions.

6.2 SLM Fourier filters

Fourier filtering is a common technique applied to images to enhance desired information of a sample object [111]. The role of the SLM in our system is to generate different imaging modalities by modulating both the phase and amplitude of the light in the Fourier plane. For example, Fig. 6.3 shows the image intensity as a function of defocus whilst displaying a darkfield filter, an annular filter or a cubic filter on the SLM. The annular filter is useful as it gives an extended depth of field [112], while the cubic filter produces an Airy point spread function [113]. For each of the following patterns, I use a grating to diffract an image far enough from the zero order (undiffracted) image so that the diffracted image does not overlap with zero order image. For this to be possible, intermediate image iris needs to be partially closed so that the cone angle of each diffracted image is less than the diffraction angle given by the SLM. As with holographic optical tweezers, where the effective pixel size of the SLM sets an upper limit to the field of view over which traps can be positioned [13], the SLM resolution sets the maximum field of view of the images not to overlap in the camera plane.

As previously reported [66], the ideal phase pattern to be displayed on the SLM for a particular imaging mode, ϕ_m, is given by,

$$\phi_m = \arg[e^{i(\alpha u + \beta v + \phi_{filter})}], \tag{6.1}$$

where u and v are, respectively, the vertical and horizontal distances from the centre of

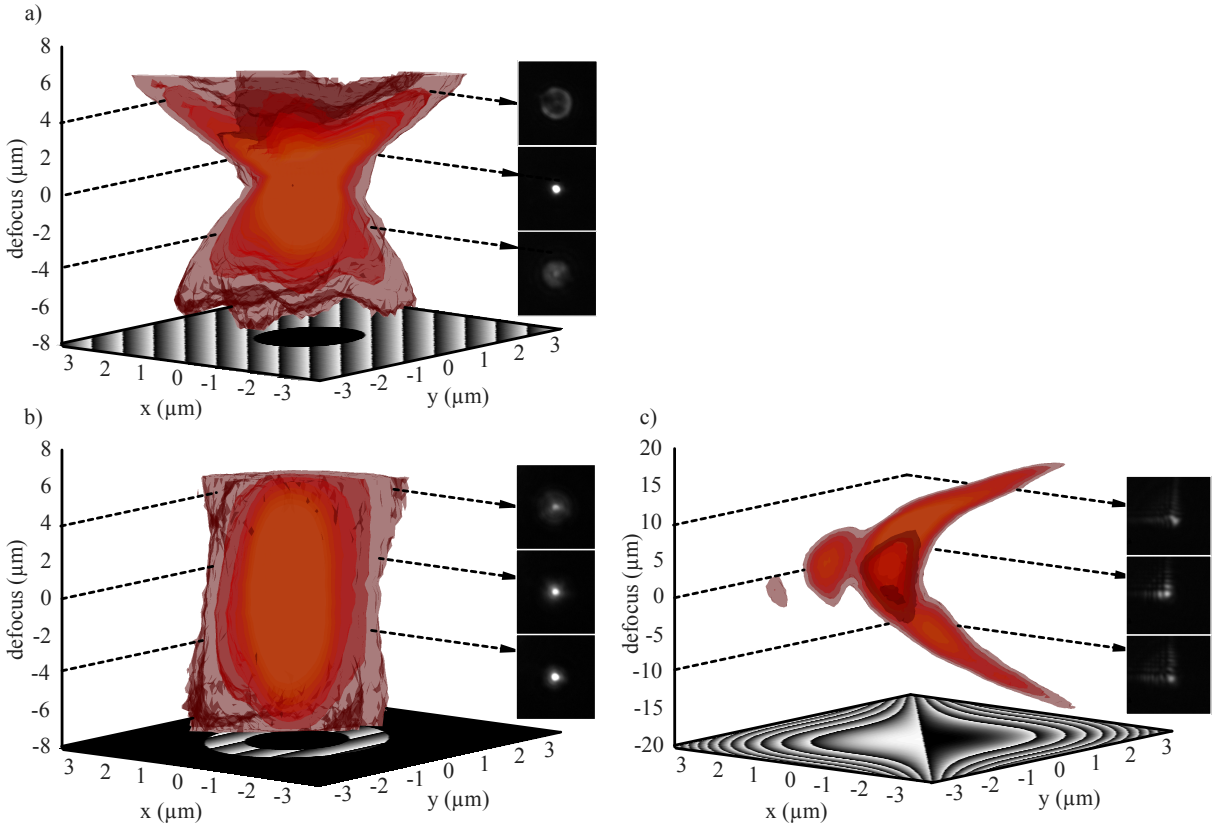

Figure 6.3: Illustrative intensity distributions of a 5 μm silica particle in water. The particle is stuck to the coverslip and is moved through the focus of the microscope. A series of images were recorded at 0.5 μm spacing in the axial direction, then four intensity isosurfaces were interpolated from the data (shown in shades of red). In the $x - y$ plane of each plot is an illustrative phase hologram used to Fourier filter the image. A darkfield filter has been used in (a), an annulus filter has been used in (b) and a cubic filter has been used in (c). The annular filter extends the depth of field of the imaging system. The cubic filter also extends the depth of field but in addition introduces a curved intensity profile. All these point spread functions were introduced by the SLM. Plotted with software developed by Dr Neal Radwell [110].

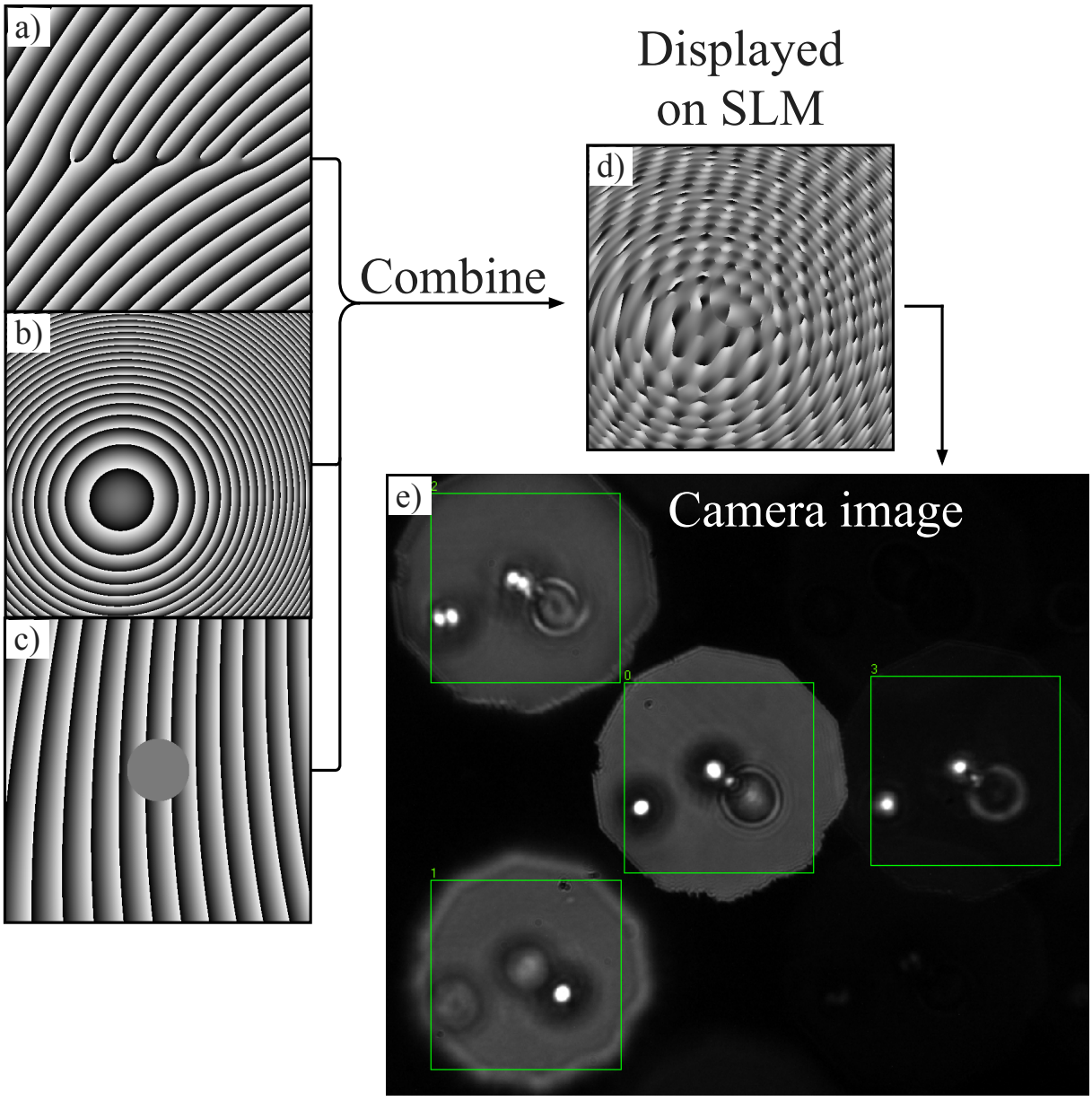

Figure 6.4: Shown here are results from combining the Fourier filters as described in the text while imaging three 5 μm silica spheres suspended in optical adhesive. (a) - (c) Shows individual phase patterns for three imaging modes, namely, double-helix point spread function, defocus and darkfield, respectively. Aberration correction has been incorporated with these filters and each also includes a grating to diffract the image. The greyscale corresponds to $0-2\pi$ phase changes. (d) The SLM display, showing the combined filter as described by Equation 6.2. (e) The resulting image detected by the camera. Subregions of the image are extracted, each 220×220 pixels. The subregions correspond to each filter; top left: double helix, bottom left: defocus, right: darkfield, centre: undiffracted zero order image.

the SLM, α and β are constants which define the angle of diffraction and ϕ_{filter} is the phase of the filter function. There are a wide range of different filter types ranging from simple implementations of defocus [45] and darkfield to more elaborate phase contrast techniques [48, 114, 46] and vortex phase masks [51].

One advantage of the SLM implementation is that it is possible to diffract several image modalities at different angles by combining their phase patterns. Several images can be produced simultaneously by the complex addition of individual kinoforms, the argument of which gives the combined kinoform and the simultaneous images,

$$\phi_{combined} = \arg\left[\sum_{m=1}^{M} R_m e^{i\phi_m}\right], \tag{6.2}$$

where m is the imaging mode produced by the SLM, M is the number of diffracted images, and ${R_m}^2$ is the relative intensity of the image. The potential interference between overlapping images is minimised by suppression of ghost diffraction orders by directing unwanted light into the zero order [16]. That is, as the combined phase pattern is a complex function, some of the amplitudes may be zero. As the SLM is a phase only object, such amplitude modulation is only achievable by greying out those areas - effectively reducing the diffraction efficiency by sending the light from these regions to the zero order. This multi-modal approach is made possible by the availability of large camera sensor arrays capable of working over a large dynamic range inherently arising from the different filter types. The design of the SLM filter to produce these images is exactly the approach used in holographic optical tweezers to produce multiple trapping beams, where each beam type can be different. Figure 6.4 shows a set of multi modal images.

Other approachs do exist for the calculation of the combined phase pattern, such as simply randomly assigning each pixel on the SLM to one individual pattern [115]. This method is computationally efficient but has been reported to suffer from a quadratic decrease in diffraction efficiency as M increases. Another approach is the weighted Gerchberg-Saxton algorithm. This is an iterative computer algorithm which finds a phase only hologram to display on the SLM that creates the diffracted image. This approach may not be suitable for phase contrast techniques, but works well for brightfield images, and even defocus [45].

A possible drawback of a microscope incorporating an SLM in the optical path is that the SLM itself introduces aberrations as it is not optically flat. However, this can be corrected for with a corresponding phase pattern displayed on the SLM. Not only can aberrations be corrected by the SLM itself, but also other aberrations in the optical train or even within a sample. I do this by manually tuning coefficients of Zerinke polynomials whilst imaging a known object, typically a $2\,\mu$m silica bead. By adjusting the focus

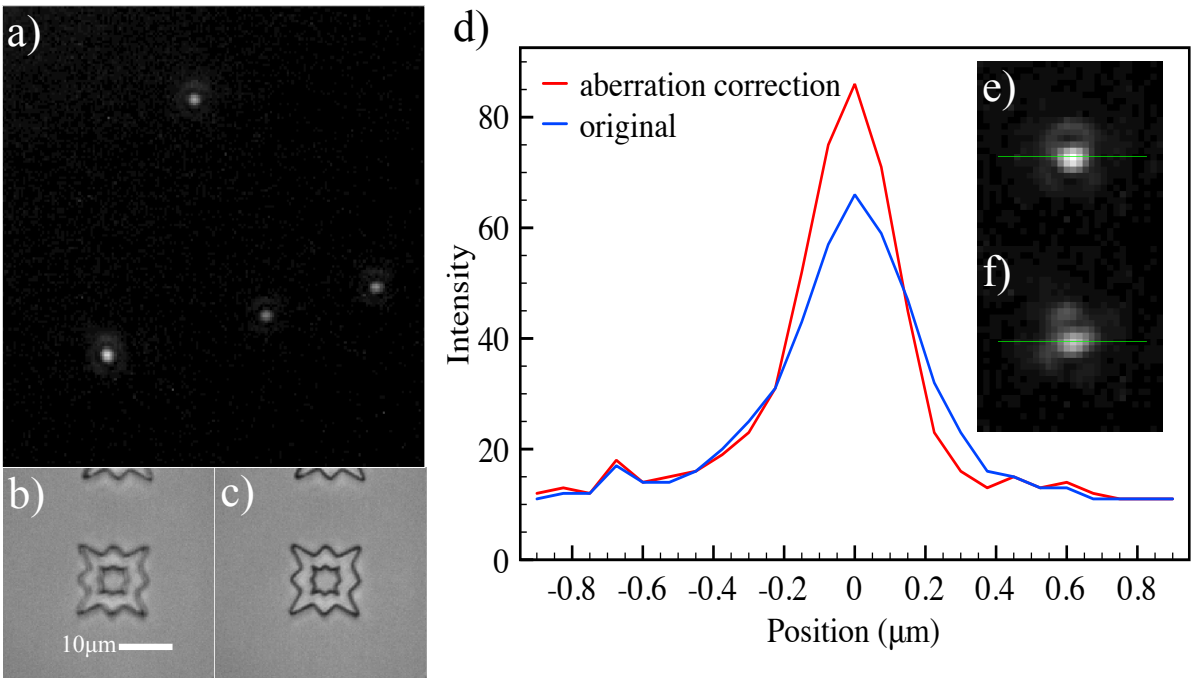

Figure 6.5: (a) A darkfield image of a dry sample of 200 nm diameter gold particles stuck to a coverslip. (b) and (c) show images of a two photon polymerised star shape in water, where (b) has had no aberration correction, while (c) has had aberration correction. (d) is a cross section throughout the point spread function of the microscope, obtained by imaging a 200 nm gold particle in darkfield. Aberration correction is seen to improve contrast by 30%. The insets in (d) show contrast enhanced lateral point spread functions where (e) is aberration corrected and (f) uncorrected. A horizontal line indicates the cross sections in (d).

of the microscope and iterating the coefficients, I was able to dramatically improve the image and remove the worst of the system's aberration [116]. Figure 6.5 gives details of the aberration correction. Whilst it was possible to correct the system aberrations, imaging an unknown object through a dynamic aberrating layer would require some kind of reference, such as a focused laser spot in the object plane. The system could then be used as a SLM-based Shack-Hartman wavefront sensor [117].

6.3 User interface

I developed a user interface to control the microscope, Fig. 6.6. This software was written in National Instruments LabVIEW. The software was designed to be easy to use by non experts. The interface consists of two main tab structures, one for displaying images and the other for choosing various settings. The images tab structure contains thee tabs, one for the wide field and two for the SLM camera. The wide field tab simply

displays the images obtained by the camera in that arm of the microscope. The SLM camera has two options. Either the full camera image can be displayed, or subimages can be extracted and displayed individually.

The full image is useful for setting the positions of the subimages. Up to 4 subimages can be set, although it is usual for one of those subimages to record the zero order image. Once the subimages have been set, they can be extracted so that SLM settings for each of these images can be selected. For each subimage, there is drop down menu where the user can select which imaging mode is required. The preset options are: Brightfield, Darkfield, Phase Contrast, Spiral Contrast, Spiral Shadow, Stereo, Cubic, DHPSF and DIC. A settings button, which when pressed, brings up a new window which contains relevant settings for that image mode. For example, the additional settings for spiral contrast are: Centre (sets the position of the fork relative to the centre of the SLM), Attenuation (sets the fraction the on axis light is attenuated by), Illumination spot (sets the area of the SLM to attenuate), and ℓ index (which sets the number the of azimuthal index of the filter, usually $\ell = 1$). There is also a control for the relative intensity and defocus of that subimage. The SLM camera has a large dynamic range, and, since some imaging modes are inherently dimmer than others (for example darkfield), there is a control to rescale the pixel values for display purposes. This means that different subimages can be set to a particular dynamic range for optimal images.

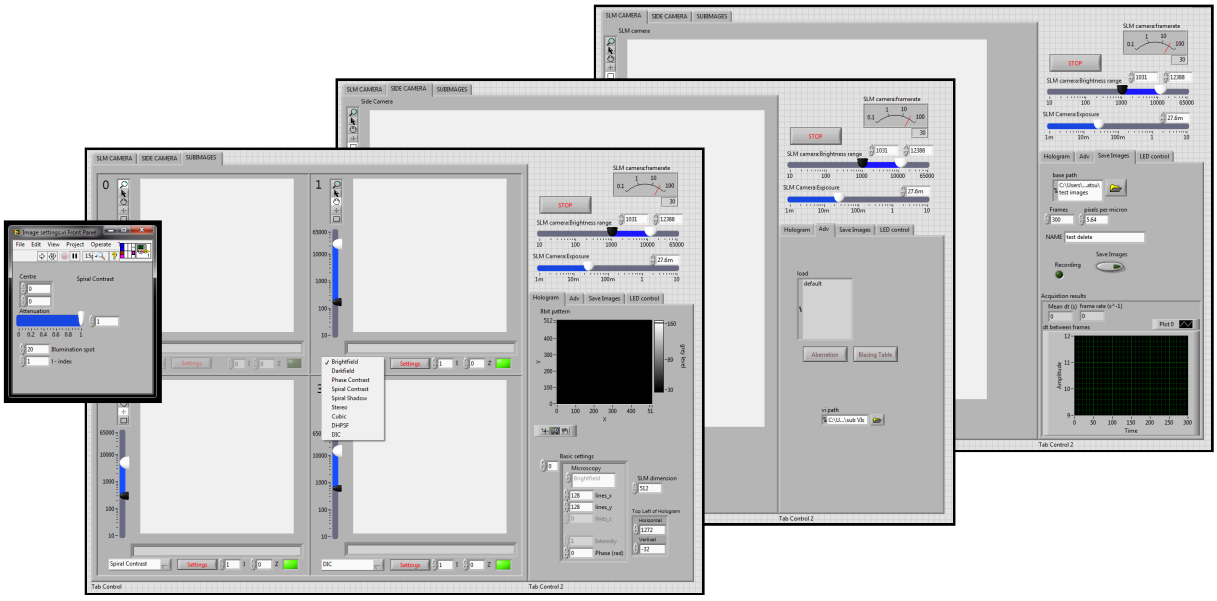

Figure 6.6: Screen shots of the SLM microscope user interface showing various tab controls. In the subimages tab, there is a drop down menu for each diffracted image containing a list of preset filter types. There is then a settings button which opens a window in which relevant settings for that filter can be adjusted. Various camera controls are also present (such as exposure time).

The second tab structure has additional settings and functions which are applied to all the diffracted orders. In the Hologram tab, there is a display of the 8-bit pattern which is displayed on the SLM. There are also Basic settings, which controls the position of each diffracted image, as well as the overall phase of the diffracted image. Once initialised, these settings rarely need changing. Further Hologram settings include the size of the SLM dimension (in pixels). In our system, a 512×512 pixel SLM is used. As the SLM is addressed as a second monitor, the position of the SLM display relative to the primary monitor needs to be set. In the Adv. tab, more advanced settings can be adjusted. These include the Aberration, and Blazing Table. The aberration settings consist of adjusting the coefficients of Zernike polynomials (such as spherical aberration, astigmatism, and so on). This correction is applied globally to the SLM. The Blazing Table (also called a look up table) sets the mapping of 8-bit values to phase shifts on the SLM. Manual tuning of this can be helpful in controlling the amount of light is various orders. The Save Images tab allows the user to quickly save a number of images to a specified location on the hard disk. It does this by first storing the images in RAM to obtain the maximum acquisition rate. There is also an LED control tab, used to set the power of the LED light source.

6.4 Commercialisation

The intellectual property for system described above was transferred to Boulder Nonlinear Systems, Ltd (BNS). As part of the exchange, I spent two months at BNS in Colorado, USA. This was done as a secondment from my PhD and was funded by the Scottish Universities Physics Alliance (SUPA). The outcomes of the visit were comparison images betweens our SLM microscope and a commercial microscope, along with a new version of the microscope control software. I also delivered a user manual for the SLM microscope.

VII
Holographic stereo microscopy

Independently of the development of the SLM microscopy, Bowman *et al.* reported a new approach to stereo microscopy [54]. Normally, a stereo microscope comprises of two objective lenses and a single light source. In the new approach, a single objective lens was used with two light sources illuminating the sample at two distinct directions. The images from these direction were separated with a bi-prism in the Fourier plane. This has also been achieved with two different colours of illumination [118]. More recently, the bi-prism was replaced by an SLM, albeit with a conventional light source [55]. In this chapter, I use an alternative illumination for the SLM microscope, which consists of three acrylic fibres positioned 2 mm from the sample: one on axis, and two at $\pm 30^\circ$ for stereoscopic operation. The SLM acts as the bi-prism to create a stereo microscope that is also capable of darkfield and defocus in conjunction with stereo microscopy. This new technique improves 3D visualisation, extends the depth of field and could allow stereo microscopy to be used for more weakly scattering objects.

In this chapter, I acknowledge the contribution of Dr R. Bowman for help in design of the stereo apparatus. The design of the holograms and the measurements are my own work. This work is part of a publication in Optics Express [44].

The stereo microscopy approach uses a single microscope objective lens and a custom illumination consisting of two optical fibres at an angle around 30° to the optical axis, yielding two views of the sample. This method enables the three dimensional tracking of particles without the need for complex beam steering optics or the requirement for pre-recorded template images. It is also easily scaled to track multiple particles simultaneously, and has been employed to track the motion of non-spherical particles in a novel form of scanning probe microscopy [22].

The two images are from different angles of illumination and, just as binocular vision gives humans depth perception, depth information can be obtained from the images. A particle moving in the z direction will move from left to right in one image and from right to left in the other. It is simple then to attain the z displacement, δz, as,

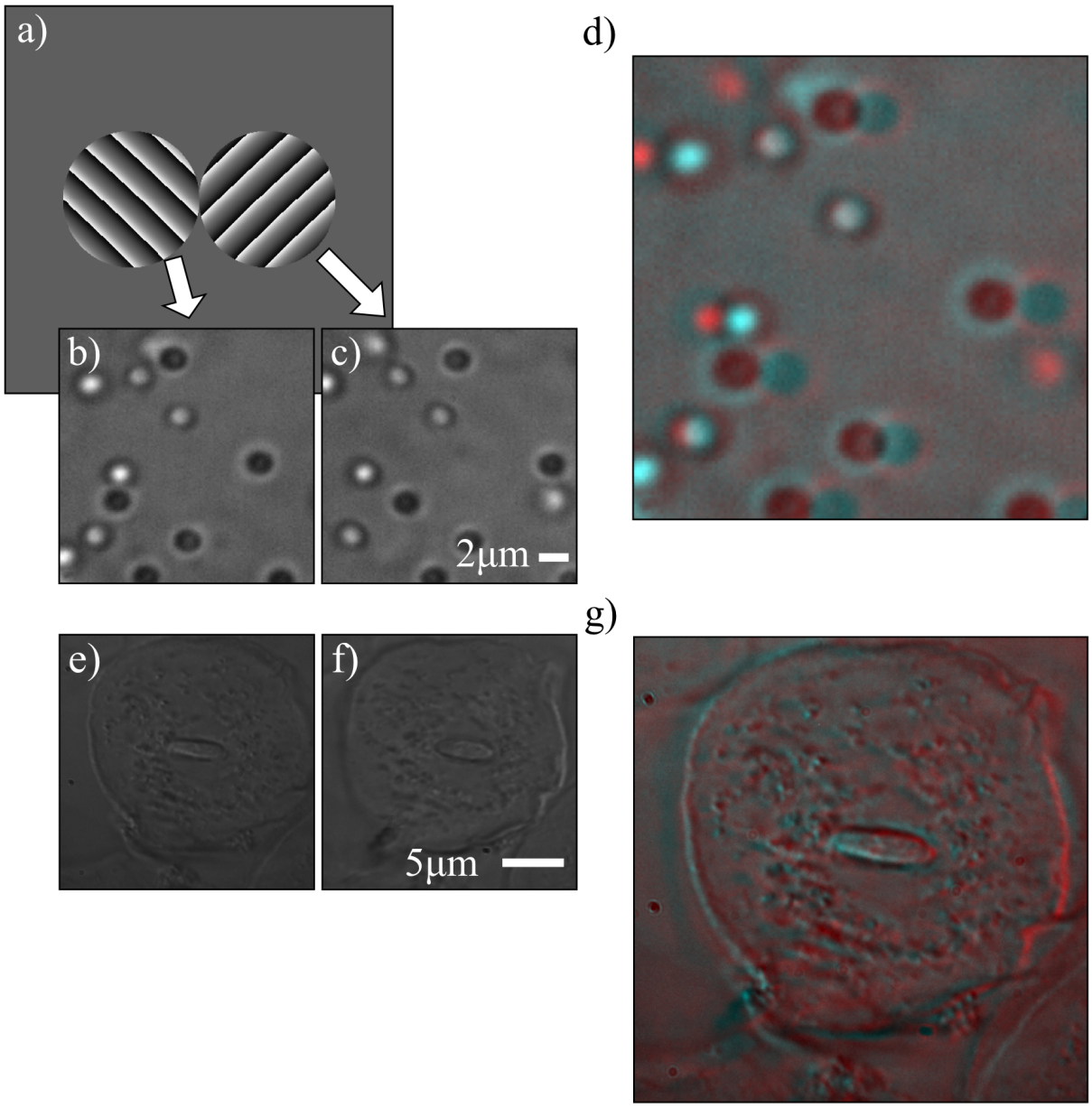

Figure 7.1: 3D position coordinates can be obtained using the software's particle tracking capabilities. (a) An image of the SLM display where the greyscale represents $0 - 2\pi$ phase change. Two apertures can be seen corresponding to the two views of the sample, each with a different grating so that the images from these angles don't overlap in the image plane. (b) and (c) The different images extracted from an image recorded on the CMOS camera. The images are of the same object, 2 μm polystyrene spheres undergoing Brownian motion in water. (d) Stereo visualisation of particle positions. The images (b) and (c) are colour coded and overlapped. With 3D stereo glasses, the user can visualise the scene with depth perception. Images (e) and (f) are of the same cheek epithelial cell nucleus as viewed with the stereo microscope. Viewing the sample from two directions affords additional geometric information about the cell structure. g) shows the e) and f) colour coded and overlapped for stereo visualisation.

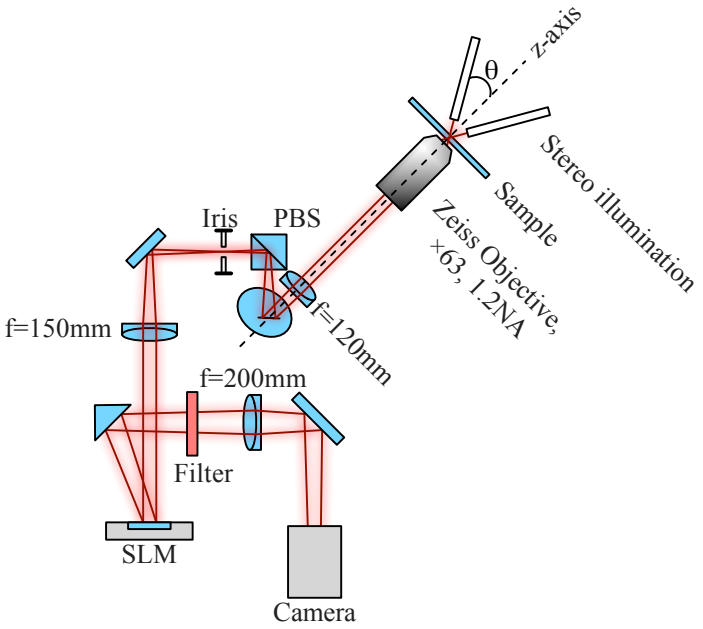

Figure 7.2: Set up of our holographic stereo microscope. The two red lines represent the optical fields from the two light sources. The SLM introduces an angular deflection between these two fields.

$$\delta z = \frac{\delta x}{2\tan\theta}, \tag{7.1}$$

where δx is the difference in the x position of the particle in the two images and θ is the angle of the optical fibres to the vertical axis (i.e., the fibres are separated by 2θ).

Illuminating at two angles corresponds to two positions in the Fourier plane and around these positions is the scattered light from the particles in the sample. For each of these light fields, a wedge prism deflects the light so that they do not overlap in the image plane. Also, a twin circular aperture needs to be placed just in front of the prisms in order to restrict high angled scattering from one view contributing to the image for the other view. In [55], Hasler *et al.* an SLM was used to create stereo images with just a single, on axis, illumination. As discussed by the authors, this approach leads to an inversion of the image for some samples owing to the division of the scattered field in the Fourier plane. By using two light sources there are effectively two separate light fields which, in the Fourier plane, only overlap at high spatial frequencies. By blocking these areas with the twin circular aperture images can be obtained which are suitable for particle tracking and free from inversion, albeit with a high frequency cutoff.

The twin aperture needs to be designed for a particular magnification or illumination angle, θ, as these set the position of the light fields in the Fourier plane. With the use of an SLM here, the stereo microscope is made more flexible, see Fig. 7.1. With no

mechanical change to the system described in Section 6.1, the SLM can be used in place of the twin apertures and prisms. The size and position of the apertures on the SLM are now reconfigurable, meaning it is possible to switch between microscope objectives and have corresponding SLM phase patterns ready to compensate for the new position and size of light fields for each view. It is also possible to experiment with different angles of illumination and adjust the SLM display accordingly, which may be more suited to particular applications. The approach works well for particle tracking spheres, but it's also possible to image extended objects, Figs. 7.1(e) and 7.1(f). Viewing from two different directions can give additional information of the shape of the structure, however, the large separation angle between the two views means 3D visualisation of such objects is difficult (if the images were to be colour coded and overlapped).

7.1 Holographic stereo microscopy and holographic lenses

As a demonstration of the flexibility of the system, holographic stereo microscopy is combined with holographic lenses and darkfield imaging. Images of a 5 μm silica bead viewed with stereo illumination and an objective 100×, NA = 1.3 (Zeiss) are shown in Figs. 7.3(a) and 7.3(b). With stereo microscopy, particle tracking accuracy and precision is limited by the defocusing of the tracked object: the more the particle moves away from the focal plane, the less reliably can its position can be measured. Adjusting the focus of the objective lens to keep the particle in focus during a measurement is not always desirable. Adjusting the focus holographically has the advantage of having no mechanical movements, as well as maintaining the parallax displacement if separate lenses are aligned to the axis of each view. This means the image can be focussed without causing a lateral shift, i.e., the measured x position in each view is unchanged. The range of this technique is now limited by the field of view, rather than the depth of focus of the microscope. In Fig. 7.4, the improvement to the accuracy of the z position measurement as a function of distance from the focal plane is shown. Without the lens correction, the tracking error increases quickly outside of the depth of focus of the microscope [54]. However, with the application of holographic lens correction, the error falls to a mean of 5.5 nm across a 50 μm range.

This stereo visualisation approach has parallels with human vision, where each eye has its own lens. This addition of a lens could be of benefit to 3D tracking with a adjustment of the focus to optimise the trackability of a particle without changing its position in the image.

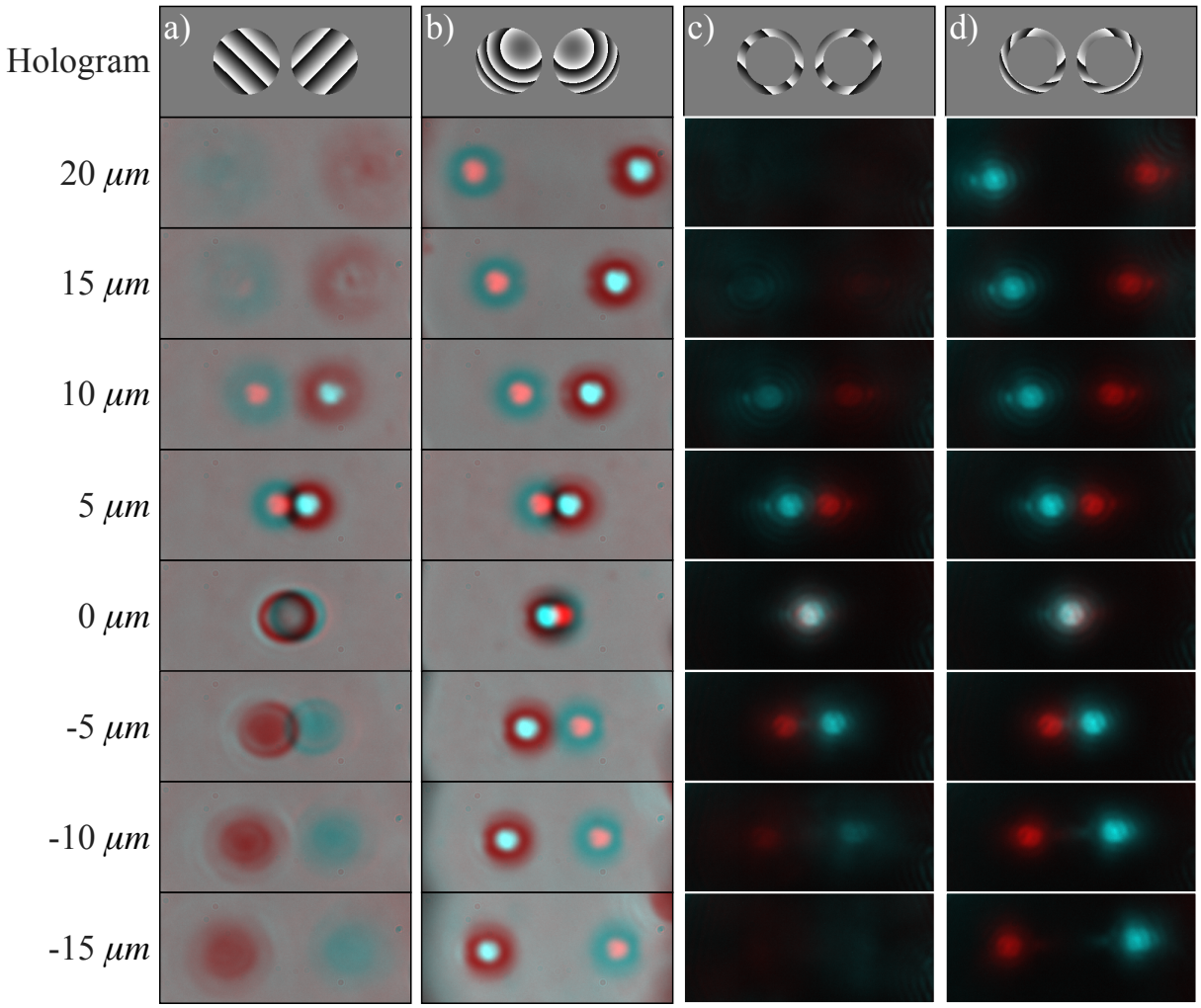

Figure 7.3: Recorded images of a 5 μm silica bead fixed in position on a microscope slide. The bead was illuminated with stereo illumination, so that the bead translates as the focus of the microscope objective is adjusted over a 35 μm range. The left and right views are diffracted to different positions on the camera then extract, colour and overlap the images. (a) The SLM display along with stereo images as the bead goes through the focus of the microscope. (b) the SLM display used to refocus the bead as the focus is changed. The holographic refocusing does not change the position of the bead. A different holographic lens is needed for each focal position, shown is an example of the lens used at the 10 μm position. (c) Darkfield stereo images. (d) Darkfield stereo with focus correction.

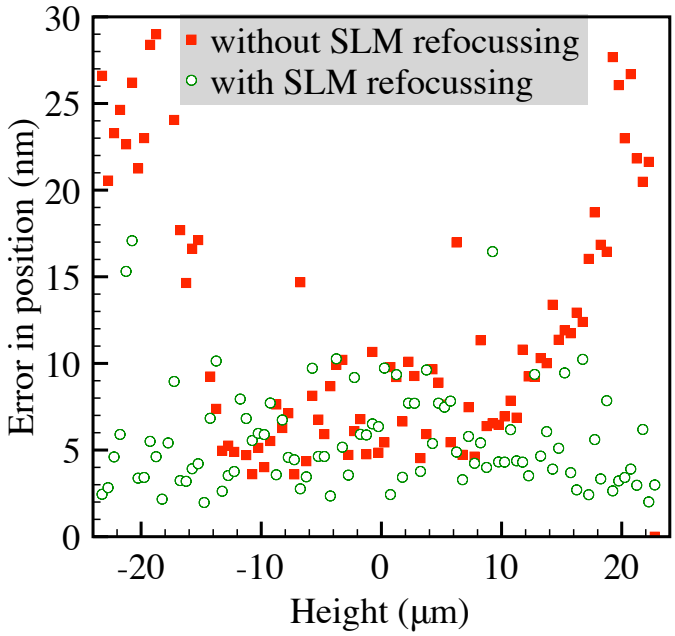

Figure 7.4: Measurement of the accuracy of z position measurement as a function of distance from the focal plane. The error is calculated from measuring the standard deviation of a series of position measurements of a 5 μm silica particle stuck on the coverslip. The improvement is due to the increased contrast brought about by keeping the particle in focus.

Again, the flexibility of the SLM implementation means that I could introduce a darkfield filter to the stereo imaging with no additional system complexity, Figs. 7.3(c) and 7.3(d). A use of the dark-field stereo could be to improve the contrast for the 3D trajectory tracking of individual water-borne single-celled organisms. In principle, all the benefits of using an SLM in the Fourier plane can be transferred to the stereo microscope, however care may be needed regarding the coherence of the illumination.

To check the calibration of the system, I studied the motion of a 5 μm silica particle optically trapped in water. The trap was positioned 20 μm above the coverslip which reduces the influence of boundary effects to below 10%. Incorporating the optical tweezer into the SLM microscope is described in more detail in Chapter 8. The camera used a reduced region of interest which allowed a frame rate of 600 frames per second. The Mean Square Displacement (MSD) of the position measurements is shown in Figure 7.5. The MSD increases linearly for free diffusion until it reaches a plateau due to the influence of the trap. The x and y MSDs agree closely due to the trap stiffnesses, κ_x and κ_y, being similar in these directions ($\kappa_x = 3.9\,\mu$N/m and $\kappa_y = 3.7\,$pN/μm). The MSD in z reaches a plateau later due to the trap stiffness being weaker in z ($\kappa_z = 1.3\,$pN/μm), yet, the fact that the slope agrees with x and y shows that the system is calibrated.

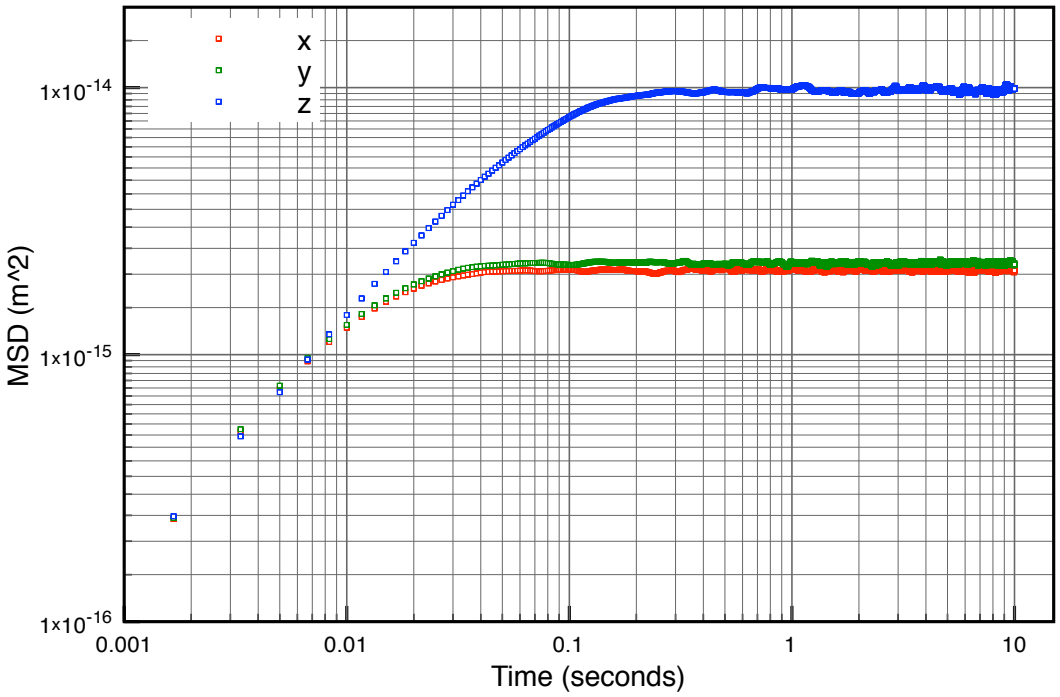

Figure 7.5: The Mean Square Displacement (MSD) of a 5 μm silica bead in water in an optical trap. The particle tracking ran at 600 Hz for 100 k frames, and the particle was held 20 μm above the coverslip, so that boundary effects were reduced. The plot shows the MSD in each axis. At short times, the bead is freely diffusing and the MSD increases linearly. At longer times, the presence of the trap inhibits diffusion and the MSD reaches a plateau region. For the x and y data, this cross over point occurs at the same time, corresponding to the trap stiffness being the same in x and y. In z, however, the trap is weaker and the particle is seen to be freely diffusing for longer.

7.2 Conclusions

I have developed a multi-modal microscope capable of stereo imaging, aberration correction and a range of other imaging modalities. The microscope uses a spatial light modulator to Fourier filter the images and generate different imaging modalities laterally displaced on the same camera. Depending on the application, existing filters can be optimised, or new filters created, and combined with stereo imaging. Novel Fourier filters can be developed with software and implemented out without additional hardware components. As an example, I demonstrated holographic stereo microscopy, and used the flexibility of the SLM to improve the range of the technique with the addition of a holographic lens, and holographic stereo darkfield microscopy, which could allow stereo microscopy to be used with weakly scattering objects.

VIII
Dynamic stereo microscopy

As described in the previous Chapter, the use of Spatial Light Modulators (SLMs) in microscopy allows the interactive control of the image Point Spread Function (PSF) [43]. This is achieved by placing the SLM in the Fourier plane of the sample, where a phase pattern can be applied to the spatial frequencies of the image. In recent years, the versatility of SLMs has allowed new forms of microscopy to be developed [48, 50, 53].

In this work, I adopt a Fourier filter that changes in real time, based on information obtained from images taken by a camera. In particular, I use an SLM based stereo microscope [118, 54] to measure the sedimentation of a silica bead immersed in water. The experimental configuration is such that the sedimenting bead falls towards the inverted microscope objective. I recorded the bead's 3D position over tens of μm *via* a stereo video particle tracking procedure. The bead position is used to continually update the focal power of a Fresnel lens on the SLM, so that the bead is always in focus. This extends the range of the procedure beyond the depth of field of standard microscopes [44], yet does not require computational deconvolution [119].

Acknowledgements for this chapter go to Dr David Phillips and Dr Richard Bowman for writing the fast hologram software. The design of the experimental procedure, running the experiment, data analysis was entirely my own work.

In absence of external flow and at low volume fractions, the bead's sedimentation is governed only by the balance between two body forces and one surface force, respectively, the gravity force ($\rho_{\mathrm{s}}\mathrm{V_s g}$), the buoyancy force ($\rho_{\mathrm{f}}\mathrm{V_s g}$, where V_s is the volume of the sphere), and the viscous force ($6\pi \mathrm{a}\eta\frac{\mathrm{dz}}{\mathrm{dt}}$):

$$\rho_s V_s g - \rho_f V_s g - 6\pi\eta a\frac{dz}{dt} = 0 \tag{8.1}$$

$$\frac{4}{3}\pi a^3 g(\rho_s - \rho_f) - 6\pi\eta a\frac{dz}{dt} = 0. \tag{8.2}$$

Rearranging gives,

$$\frac{dz}{dt} = \frac{\frac{4}{3}\pi a^3 g(\rho_s - \rho_f)}{6\pi\eta a} \tag{8.3}$$

$$= \frac{2ga^2(\rho_s - \rho_f)}{9\eta}, \tag{8.4}$$

where dz/dt is the sedimentation rate, g is the acceleration due to gravity, a is the bead's radius, ρ_s and ρ_f are, respectively, the density of the bead and of the fluid and η is the fluid viscosity (in this case a Newtonian fluid, i.e., a fluid with a constant viscosity). Sedimentation is ubiquitous in nature, from river bed formation to direction sensing in the roots of plants [120]. Sedimentation is an active area of research, with applications in many industrial processes [121, 122, 123]. It can also be used as a tool to probe physical properties of complex fluids, such as liquid crystals [124].

In this work I demonstrate a new technique to measure sedimentation rates. I use Optical Tweezers (OT) [5] to trap and raise a silica bead above a microscope coverslip. As described in Chapter 1, OT work by tightly focusing a laser beam with an inverted microscope objective, which is also used to visualise the sample. Once raised, I switch the laser beam off to allow the particle to sediment from a known height. I then use a dynamic version of Stereo microscopy [118, 54] to measure the three dimensional thermal fluctuations, along with the sedimentation. No changes are needed for stereo microscopy's implementation with OT, two light sources are positioned above the sample, illuminating it from two different angles as before. The difference in this work is that the stereo filters in the Fourier plane are dynamically updated to keep the bead in focus.

8.1 Experiment

The experimental set up is similar to that described in Chapter 7 and is shown in Fig. 8.1 a). A sample of silica beads, of mean radius $a = 2.37\,\mu$m from Bangs Lab Inc, diluted in distilled water was used. The sample is prepared in a welled microscope glass slide and sealed with a 150 μm thick coverslip. The sample is illuminated with two optical fibres (acrylic, 1.5 mm diameter) held at an angle of $\alpha = \pm 30°$ to vertical in the $x - z$ plane. These fibres are positioned in a custom 3D printed mount about 2 mm from the top of the slide. A drop of water between the fibres and slide gives brighter illumination by reducing refraction at the exit plane of the fibre. Each fibre is coupled to a high power red (637 nm, 20 nm bandwidth) LED light source (Luxeon Rebel). This light is filtered with a 636 nm, 10 nm bandwidth interference filter prior to the camera.

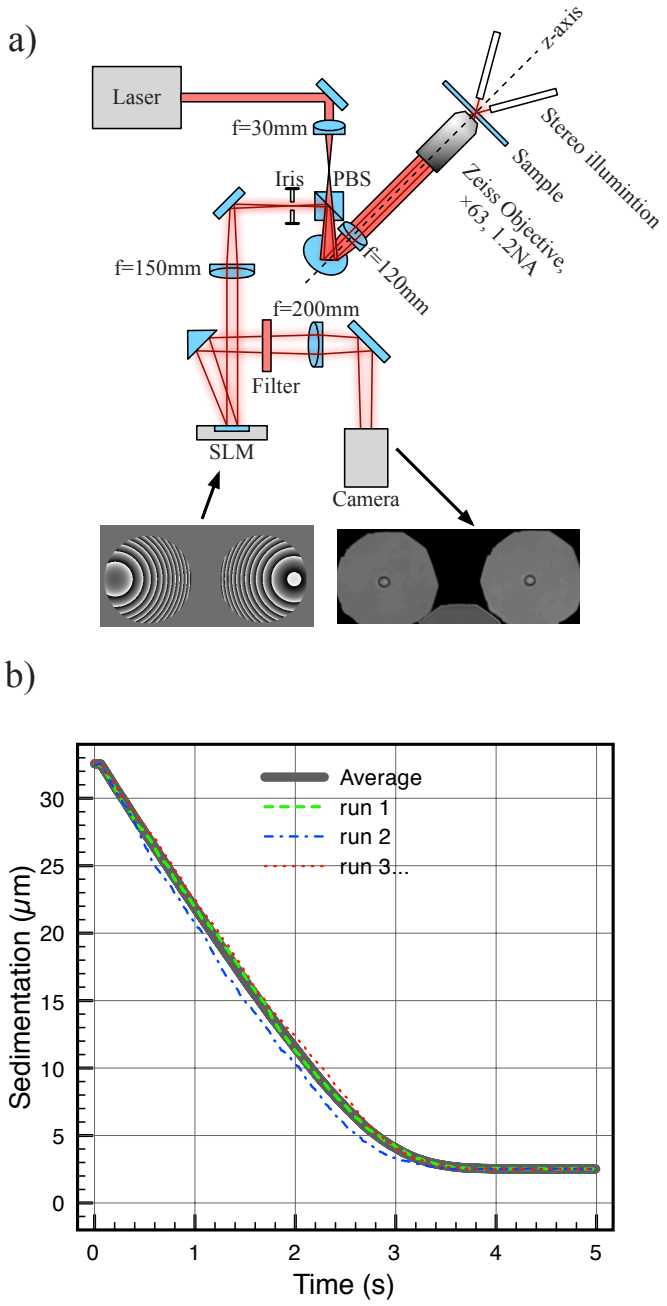

Figure 8.1: a) Schematic view of the experimental setup. The red shaded area shows the path of the trapping laser, while the two red lines show the paths of the light from the two illumination fibres. The bottom-left image shows the SLM pattern that diffracts the light at a different angle for each illumination. The bottom-right image shows an example of a stereo image taken by the camera, from which the 3D position is obtained. b) The full position trace of the bead's centre recorded during sedimentation. The green (dashed), blue (dash-dot) and red (dot) lines show positions recorded from a single sedimentation run. I recorded up to 50 runs. The averaged result, shown in grey, is normalised such that $z = 0\,\mu$m being the bead on the coverslip, its centre being one particle radius higher.

The objective is a Zeiss 63×, 1.2 NA water immersion lens which is mounted on a linear stage (LS-50-M, ASI) for focusing and positioning of the optical trap. The trapping laser is a 671 nm DPSS laser from Changchun New Industries Optoelectronics Technology Co., Ltd. which has a maximum power output of 300 mW. The beam is expanded and directed in to the back aperture of the objective. The expanded beam is slightly diverging such that the laser focus is 7 μm above the image plane.

A polarising beam splitter is used to separate image light from the light of the trapping laser. An image of the sample is formed 2 cm from the beam splitter and here is placed an adjustable aperture to reduce the field of view. A Fourier lens images the back aperture of the objective on to a 512 × 512 SLM (Boulder Nonlinear Systems XY series). The filter can be quickly updated by calculating the desired pattern on the graphics card [94]. Images are recorded with a Dalsa Genie GM1020 CMOS camera, which with a reduced region of interest, can capture images at 500 Hz. The camera is aligned such that the apparent x motion, resulting from z displacement, corresponds to pixel rows. This allows a higher acquisition rate.

8.2 Procedure

In order to perform the measurement, a bead was loaded into the trap and positioned 32 μm above the coverslip. The laser is then switched off via USB control and the bead position recorded until it sediments onto the coverslip. This is a small delay of 1.5 ± 0.1 ms between the command signal and the laser beam shut-off. This was measured by observing laser light reflected by the coverslip and by adopting a very small region of interest such that the frame rate was greater than 1 kHz. The calibration of the experiment starting time allowed us to determine exactly at which frame the laser was switched off; this being an important feature that relates to future microrheology measurements. The bead trajectory was measured by means of a video particle tracking procedure based on a centre of symmetry algorithm [125] applied separately to each view of the bead. With the stereo microscopy there are two independent measurements of the displacement in the y direction; one measurement of the displacement in the x direction, which is given by the average of the two measured x positions on the camera, and the displacement in the z direction, as deduced from the separation of the images, given by $z = \frac{\delta x}{2\tan\alpha}$, where δx is the difference between the two x measurements on the camera, and α is half angle between the fibres. As these coordinates are calculated in real time, the calculated z position can be used to update the SLM with a Fresnel lens pattern, which refocusses the bead. The SLM is updated at 100 Hz. The linear relationship between Fresnel lens power and imaged focal height was empirically found. I achieved this by measuring

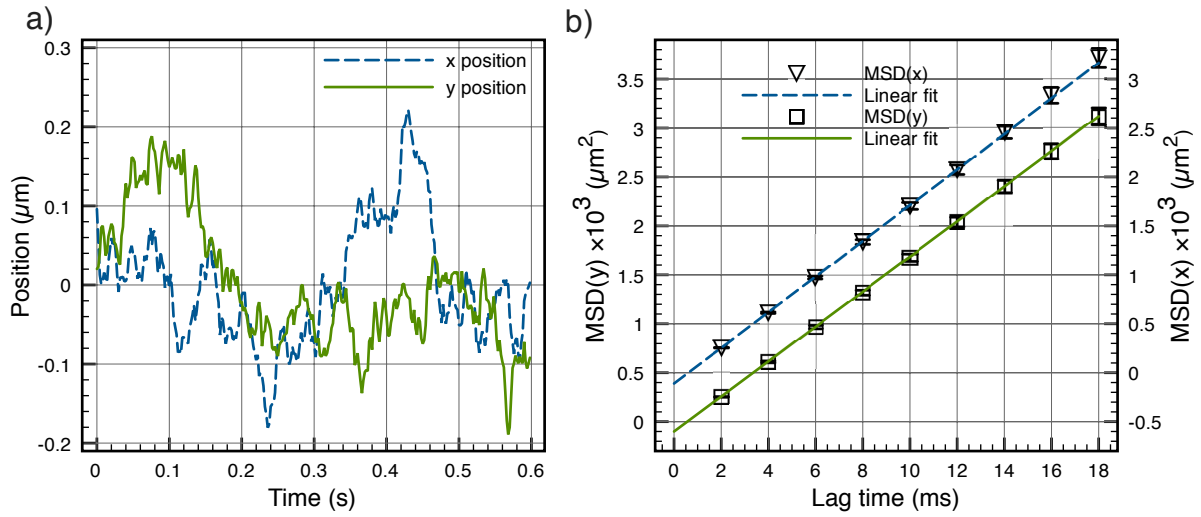

Figure 8.2: During each sedimentation run, the x and y are also recorded position of the bead. Shown in a) is the x (blue, dashed) and y (green, solid) for an example run using a particle with diameter of 4.84 μm. The Mean Square Displacement (MSD) of this trajectory can then be calculated. By averaging the MSD for 50 repeats, the data shown in b) is obtained. Here, the error bars are the standard error of the mean. The MSD(x) data ($\bigtriangledown$) has been shifted from the MSD(y) data ($\square$) for clarity. The fits do not intercept zero owing to the tracking error and finite exposure time in the acquisition [126]. From the slope of the linear fits of MSD(x) (blue, dashed) and MSD(y) (green, solid) a particle diameter of 4.77 μm and 4.90 μm is obtained, respectively

the change in observed height of a bead adhered to the coverslip, moved by a known vertical distance with the translation stage. A scaling factor can then simply multiply the measured z displacement from the focal plane to obtain the focal length needed to refocus the image. Once the auto-focussing procedure has been calibrated, a bead remains in focus without adjustment of any optics. In principle, this procedure does not affect the position measurements described above, but only the precision of the measurement as the position of a more in focus bead suffers less from camera noise. In practice, as a bead goes out of focus, it may also obtain asymmetric distortions which will lead to large errors in the centre of symmetry algorithm, i.e., the accuracy may also be more reliable for an in focus bead. In a previous work, I found that the lens correction procedure gave the position of a bead with an error of 5.5 nm over a 50 μm range [44].

8.3 Results

Typical z position traces are shown in Fig. 8.1 b). These data are from the same bead, and I average multiple sedimentations (up to 50 runs) to average out Brownian noise.

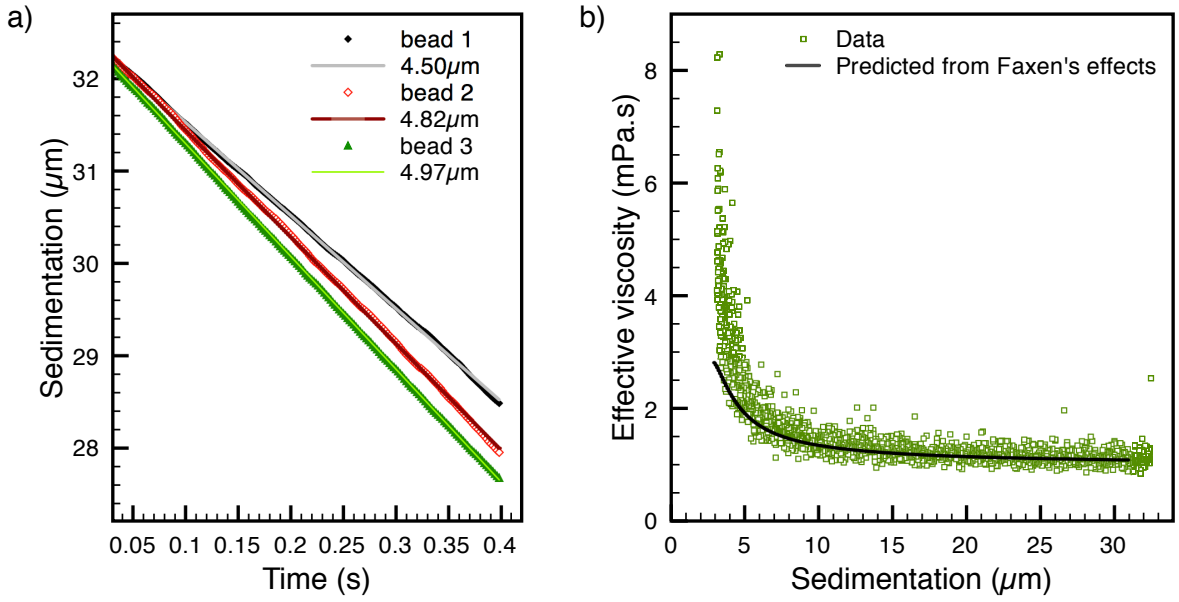

Figure 8.3: a) The average initial part of sedimentation shown for three different beads. Over this range, the viscosity is nearly constant. With a linear fit, knowing the viscosity, the bead size can be extracted and vice versa. b) The effective viscosity experienced by a sedimenting bead approaching a boundary.

8.3.1 Particle sizing by sedimentation

The distance to the bounding coverslip decreases as the particle descends, resulting in the drag coefficient of the bead increasing according to Faxén's correction. However, during the initial part of the descent, from $32 - 28\,\mu$m, this effect is small, less than 1%, and below the 4% standard deviation for repeated measurements. Therefore, only this part of the trajectory is used to calculate the bead's diameter. These measurements are shown in Fig. 8.3 a). The bead size is determined by fitting Eq. 8.4 to the data. Notably, equation **??** has a square dependence on the bead size, which enhances the sensitivity of the measurement. By averaging the measurements, the standard error in the bead sizing reduces to around 1%. The parameters used in the fitting procedure are: a temperature of 22°C, density of silica of $2.0 \times 10^3\,\mathrm{kg/m^3}$, density of water of $1.0 \times 10^3\,\mathrm{kg/m^3}$ and water viscosity of 0.96 mPas.

8.3.2 Particle sizing by diffusion

The particle tracking procedure is also able to provide the x and y coordinates. Far from the coverslip, these data are independent from the sedimentation process and there-

	Sedimentation (μm)	$MSD(x)$ (μm)	$MSD(y)$ (μm)
Particle 1	4.50	4.51	4.81
Particle 2	4.82	5.28	5.06
Particle 3	4.97	4.66	4.73
Particle 4	4.95	4.93	4.60
Particle 5	4.88	5.07	4.71
Particle 6	4.86	4.99	4.77
Particle 7	4.53	4.85	4.52
Particle 8	4.84	4.77	4.90
Mean	4.79 ± 0.18	4.87 ± 0.22	4.74 ± 0.18

Table 8.1: Results comparing the diffusion method with the sedimentation method for particle sizing. The beads used come from a population with mean diameter of $4.72\,\mu$m. For each particle, the standard deviation in sizes from the different methods is on average 3.5%.

fore can be used to estimate the bead size by means of its Mean Square Displacement (MSD) (computed as MSD $= \left\langle [x(t+\tau) - x(t)]^2 \right\rangle$, where τ is the time interval or lag-time). For Newtonian fluids (e.g. water) the bead's MSD is expected to grow linearly with time, MSD = Dt, where D is the diffusion coefficient given by $k_B T/6\pi\eta a$, where k_B is Boltzmann's constant and T is absolute temperature. Again, only the initial part of the data can be used, owing to the increase in drag coefficient closer to the coverslip. Once the MSD is calculated, a linear fit was used to obtain the diffusion coefficient from which the particle size can be found. An example x and y position measurement is shown in Fig. 8.2 a), from which the MSD is calculated. I average the MSD for the many runs and fit to obtain the diffusion coefficient, Fig. 8.2 b). There exists an offset to the data which is due to a finite exposure time (2 ms) and localisation error ($\sigma = 5\,$nm)[126]. Comparing the different methods (sedimentation and MSD) of finding bead size I found that the mean deviation between techniques is 3.5%. The mean size closely matches the given value from the manufacturer, Table 8.1. The MSD method is expected to be less reliable as the statistical averaging typically requires a long measurement, which is unavailable in this case as the bead is approaching the coverslip. Nonetheless, it provides additional information and acts as a good check that the system is calibrated.

8.3.3 Faxén's correction

In this section I show the Faxén's effect as manifested by a change in mobility experienced by a sedimenting bead. The change in mobility acts in the same way as a change in effective viscosity $\eta(z)$, which can be found as a function of distance from the coverslip is given by rearranging Eq. 8.4:

$$\eta(z) = \frac{2gr^2(\rho_s - \rho_f)}{9\frac{dz}{dt}}. \tag{8.5}$$

The change in effective viscosity is given by Faxén's correction is,

$$\eta(z) = \eta_0 \left[1 - \frac{9}{8}\frac{r}{z} + \frac{1}{2}\left(\frac{r}{z}\right)^3\right]^{-1}, \tag{8.6}$$

where η_0 is the viscosity far from any boundary [32]. I differentiate the average data shown in Fig. 8.1 b) to compute $\frac{dz}{dt}$ using finite differences. Using the bead size found previously $\eta(z)$ can be calculated, shown in Fig. 8.3 b). The fit is the equation for perpendicular Faxén's correction given in [74]. Owing to the numerical differentiation, the data is quite noisy, however there is a clear trend in agreement with theory.

8.4 Conclusion

I have demonstrated a new technique to measure the bead diameter and diffusion coefficient of microspheres by observing their sedimentation trajectory with a three dimensional SLM microscope. I used an algorithm which automatically updates the SLM Fourier filter to increase the tracking range, allowing results to be recorded over both an initial range and while approaching a boundary. The bead diameter is found using the initial data, far from the coverslip using two methods: sedimentation and mean square displacement. I then use this result to find how Faxén's correction affects the sedimentation process and show good agreement with theory. I foresee this procedure to be of interest in the study of the sedimentation process itself, or in using sedimentation as a tool to study complex fluids.

IX
Conclusion

It could be said, with the impressive control we have over the optical field, that optical systems are truly coming of age. At present, with liquid crystal SLMs, there is $10\,\mu$m spatial resolution, and 1 kHz temporal resolution. These devices can efficiently change the phase of an input light field, however amplitude modulation is inefficient (as the light can only be attenuated). Nonetheless, SLMs have been used in a large number of optics experiments, from blue sky research to practical applications. The aim of this thesis was to explore one such practical application, namely, optical microscopy. In particular, I have attempted to answer questions in optical tweezers and SLM microscopy.

In optical tweezers, I applied SLMs to investigate the processes of hydrodynamic coupling between particles in bistable potentials, Chapter 3. The experiment consisted of two bistable optical traps each containing a single particle. I was interested in what form the hydrodynamic coupling between these spheres took. This work involved recording long measurements of the particles positions, and there were a number of problems that had to be solved. I found that $0.8\,\mu$m diameter silica spheres were easier to create bistable potential traps for, but these required a new tracking procedure to be developed. I found that the long time needed for measurements often led to the experiment being contaminated with a freely diffusing particle, or that the laser would drift making the bistable trap unbalanced. I compensated for these effects by adding some salt to the sample which stuck down most particles to the coverslip. I also introduced a closed loop feedback system which automatically corrected for laser drift. I derived the mathematical expression for the power spectrum of a fluctuating particle, and the expected number of coincident hops between two randomly fluctuating systems. An analysis procedure was developed in which a low pass filter was applied to the data to remove high frequency vibrations. Also, a practical definition of what a constitutes a hop in a bistable system was developed.

With these procedures in place, I was able to record sufficient data to conclude that the probably of a symmetric (p) hop significantly outweighed the probability of an anti-

symmetric (n) hop when the two systems were placed in close proximity. As a control, I found that as the separation increased this biassing reduced, meaning that the effect was due to the coupling between the spheres, rather than any external vibration.

In Chapter 4, I used holographic optical tweezers to create an intricate energy potential to provide an alternative solution to a problem encountered in the previous chapter. Rather than adding salt to the sample (which may not always be desirable) I sought to reduce freely diffusing material entering the trap by introducing a Laguerre Gaussian beam around the trap. If this worked, there would be an all optical means to perform long measurements in colloids or biological samples, where diffusing material really compromises measurements. To test the approach I compared the length of time I were able to successfully measure the viscosity of water with and without the Laguerre Gaussian beam, which I called an "optical shield." This experiment was performed in a sample with a large number of diffusing $0.8\,\mu$m silica beads (much larger than in a typical optical tweezer experiment). To identify when the trap was compromised, I used the variance of the brightest pixel in the recorded images. If two particles are in the same trap, I observed them to jostle for position, leading to large fluctuations in the brightness of the image. I recorded 250 measurements of time until contamination, together with viscosity, which was obtained from the standard autocorrelation method. I found an order of magnitude increase in the time until contamination when using the optical shield. In addition, there was no significant difference between the viscosity measured with and without the optical shield.

In Chapter 5, I used a holographic tweezer system as a measurement device, rather than for generation of optical force. The system used a circularly polarised laser beam to trap and spin a birefringent particle. A beam was shaped holographically using a superposition of OAM modes, which illuminated the particle with a circularly symmetric petal pattern. The aim of the experiment was to find out if intensity fluctuations in the reflected probe beam could be used to infer the rotation of the particle. This was expected as OAM modes of the light beam should be frequency shifted by the rotation of the particle. The beat frequency between the these modes had been shown to give an intensity modulation at $2|\ell|\Omega$ for a macroscopic spinning disk (where ℓ is the OAM mode, and Ω is the rotation rate of the disk), but it was an open and interesting question whether this would hold for a particle the same size the as diffraction limit of the measurement beam.

I measured the intensity modulation with a photo diode, and changed the OAM modes of the illumination between $\ell = \pm 0, \pm 1, \pm 2$, and ± 3. The rotation rate of the particle was independently verified using video particle tracking. I then looked at the power spectrum of the intensity reflected off the particle. By changing the ℓ mode of the probe

beam, a significant boost in power was detected in the corresponding harmonic at $2|\ell|\Omega$, implying the Doppler shift of the illumination beam. There are also other peaks in the power spectrum corresponding to undertones of the Doppler frequency. These peaks were attributed to misalignment of the probe beam to the rotation axis of the particle. In fact, the rotation axis of the particle was ill defined due to Brownian motion. The peaks are also broadened by the effect of Brownian motion. This procedure is robust to these effects and, therefore, provides a measurement which can unambiguously determine rotational motion from translation.

The second half of the thesis concerns SLM microscopy. Chapter 6 describes the development of an SLM microscope, the intellectual property of which was transferred to a small enterprise in the USA. This chapter had the aim to design and characterise the system. I developed a compact design, which was simple to align and allowed access to the adjustable mirrors. Other design features include two cameras to make use of all the light from the sample, an adjustable iris to control field of view/number of diffracted images trade off, and an interchangeable illumination for various imaging modes. I created a user interface which was designed to be flexible and easy to use. The system was characterised in terms of its point spread function, and found the resolution to be 200 nm, which was improved by aberration correction. I provided examples of the microscope's multimodal capabilities such as the double helix point spread function, darkfield, and defocus.

In Chapter 7 I demonstrated new forms of imaging, by combining SLM microscopy with stereo microscopy. Here, I replaced the twin aperture and prism with an SLM. The advantage of this was that alignment on to the twin aperture is easier, as the aperture can be precisely positioned. Furthermore, the size of the aperture can be controlled, meaning the optimum size for a particular sample can be used without changing any physical components. As an additional benefit, the SLM displayed a lens on top of each aperture meaning that as a sample moves in three dimensions the focus can be retained as well as the parallax measurement of stereo microscopy.

In the final chapter (Chapter 8), I developed a new form of microscopy, named dynamic stereo microscopy. This is where the lens applied to stereo microscopy is constantly updated based on information obtained from the image of the sample. In the application used to illustrate the technique, the position of a micron sized sphere sedimenting in water is used to update the focus of the lens applied to each view of the sample. This allows the position of the sphere to be tracked over a much larger range than would otherwise be possible. The experiment used optical tweezers to initially levitate the sphere in the fluid, bringing together the different aspects of my thesis. From the results of the experiment, I could quickly and accurately size the particles, as well as map surface effects from the coverslip.

In all, this thesis demonstrates new applications of SLMs in microscopy. The ability to control the wavefront of an optical field has greatly enhanced the functionality of microscopes and it seems inevitable that SLMs will feature in the future generations of research microscopes. Both holographic optical tweezers and SLM microscopy are likely to see further development and usage in and outside of optics laboratories. In the first half of the thesis, I have used optical tweezers to discover subtle hydrodynamic effects, and a rotational equivalent of linear doppler velocimetry at the micro-scale. I also extended the range of environments where optical tweezers could be used by investigating an "optical shield" to protect the trap from diffusing material. In the second half , I developed a new, compact SLM microscope and created novel modes of microscopy which I used to measure the sedimentation of a micron sized sphere. This work combined optical tweezers with SLM microscopy, an idea in which I am excited to see further research.

Bibliography

[1] Maxwell, J. C. *A Treatise on Electricity and Magnetism*, vol. 2 (Clarendon Press, 1973).

[2] Nichols, E. & Hull, G. A preliminary communication on the pressure of heat and light radiation. *Phys. Rev.* **13**, 307 (1901).

[3] Ashkin, A. Acceleration and trapping of particles by radiation pressure. *Phys. Rev. Lett.* **24**, 156 (24).

[4] Lee, M. P. & Padgett, M. J. Optical tweezers: a light touch. *J. Microsc.* **248**, 219 (2012).

[5] Ashkin, A., Dziedzic, J., Bjorkholm, J. & Chu, S. Observation of a single-beam gradient force optical trap for dielectric particles. *Opt. Lett.* **11**, 288 (1986).

[6] Wright, W. H., Sonek, G. J. & Berns, M. W. Parametric study of the forces on microspheres held by optical tweezers. *Appl. Opt.* **33**, 1735 (1994).

[7] McGloin, D., Spalding, G., Melville, H., Sibbett, W. & Dholakia, K. Applications of spatial light modulators in atom optics. *Optics Express* **11**, 158–166 (2003).

[8] Simpson, S. H. & Hanna, S. Application of the discrete dipole approximation to optical trapping calculations of inhomogeneous and anisotropic particles. *Optics Express* **19**, 16526–16541 (2011).

[9] (2014). URL http://www.youtube.com/watch?v=cjWHrPYvUo0.

[10] Wang, M. C. & Uhlenbeck, G. E. On the theory of the brownian motion ii. *Reviews of Modern Physics* **17**, 323–342 (1945).

[11] Berg-Sørensen, K. & Flyvbjerg, H. The colour of thermal noise in classical brownian motion: a feasibility study of direct experimental observation. *New Journal of Physics* **7**, 38 (2005).

[12] Florin, E.-L., Pralle, A., Stelzer, E. H. K. & Hörber, J. K. H. Photonic force microscope calibration by thermal noise analysis. *Appl. Phys. A.* **66**, S75 (1998).

[13] Sinclair, G., Jordan, P., Leach, J., Padgett, M. & Cooper, J. Defining the trapping limits of holographical optical tweezers. *J. Mod. Optic.* **51**, 409 (2004).

[14] Simpson, S. H. & Hanna, S. First-order nonconservative motion of optically trapped nonspherical particles. *Phys. Rev. E* **82**, 031141 (2010).

[15] Thalhammer, G., Bowman, R. W., Love, G. D., Padgett, M. J. & Ritsch-Marte, M. Speeding up liquid crystal SLMs using overdrive with phase change reduction. *Optics express* **21**, 1779–1797 (2013).

[16] Bowman, R. *et al.* Optimisation of a low cost SLM for diffraction efficiency and ghost order suppression. *Eur. Phys. J. Special Topics* **199**, 149 (2011).

[17] Grier, D. G. A revolution in optical manipulation. *Nature* **424**, 810 (2003).

[18] Svoboda, K. & Block, S. M. Biological applications of optical forces. *Annu. Rev. of Biophy. Biomol. Struct.* **23**, 247 (1994).

[19] Wright, A. J. *et al.* Investigating the interaction forces between t cells and antigen-presenting cells using an optical trapping system. In *SPIE NanoScience+ Engineering*, 80970I–80970I (International Society for Optics and Photonics, 2011).

[20] Florin, E.-L., Pralle, A., Heinrich Hörber, J. & Stelzer, E. H. Photonic force microscope based on optical tweezers and two-photon excitation for biological applications. *Journal of structural biology* **119**, 202–211 (1997).

[21] Phillips, D. *et al.* Surface imaging using holographic optical tweezers. *Nanotechnology* **22**, 285503 (2011).

[22] Phillips, D. *et al.* Force sensing with a shaped dielectric micro-tool. *Europhys. Lett.* **99**, 58004 (2012).

[23] Phillips, D. *et al.* An optically actuated surface scanning probe. *Optics Express* **20**, 29679–29693 (2012).

[24] Phillips, D. B. *et al.* Shape-induced force fields in optical trapping. *Nature Photonics* **8**, 400–405 (2014).

[25] Kramers, H. A. Brownian motion in a field of force and the diffusion model of chemical reactions. *Physica* **7**, 284 (1940).

[26] McCann, L. I., Dykman, M. & Golding, B. Thermally activated transitions in a bistable three-dimensional optical trap. *Nature* **402**, 785 (1999).

[27] Benzi, R., Sutera, A. & Vulpiani, A. The mechanism of stochastic resonance. *J. Phys. A* **14**, L453 (1981).

[28] Grier, D. G. Optical tweezers in colloid and interface science. *Curr. Opin. Colloid Interface Sci.* **2**, 264 (1997).

[29] Kotar, J., Leoni, M., Bassetti, B., Lagomarsino, M. C. & Cicuta, P. Hydrodynamic synchronization of colloidal oscillators. *P. Natl. Acad. Sci. USA* **107**, 7669 (2010).

[30] Kotar, J. *et al.* Optimal hydrodynamic synchronization of colloidal rotors. *Physical Review Letters* **111**, 228103 (2013).

[31] Berne, B. J. & Pecora, R. *Dynamic Light Scattering: With Applications to Chemistry, Biology, and Physics* (Dover, New York, 2000).

[32] Keen, S. *et al.* Multipoint viscosity measurements in microfluidic channels using optical tweezers. *Lab Chip* **9**, 2059 (2009).

[33] i Solvas, X. *et al.* Droplet microfluidics: recent developments and future applications. *Chemical Communications* **47**, 1936–1942 (2011).

[34] Pralle, A., Florin, E.-L., Stelzer, E. H. K. & Hörber, J. K. H. Local viscosity probed by photonic force microscopy. *Appl. Phys. A.* **66**, S71 (1998).

[35] Gibson, G. M., Leach, J., Keen, S., Wright, A. J. & Padgett, M. J. Measuring the accuracy of particle position and force in optical tweezers using high-speed video microscopy. *Opt. Express* **16**, 14561 (2008).

[36] Keen, S., Leach, J., Gibson, G. & Padgett, M. J. Comparison of a high-speed camera and a quadrant detector for measuring displacements in optical tweezers. *Journal of Optics A-pure and Applied Optics* **9**, S264–S266 (2007).

[37] Bishop, A. I., Nieminen, T. A., Heckenberg, N. R. & Rubinsztein-Dunlop, H. Optical microrheology using rotating laser-trapped particles. *Phys. Rev. Lett.* **92**, 198104 (2004).

[38] Tassieri, M. *et al.* Measuring storage and loss moduli using optical tweezers: broadband microrheology. *Phys. Rev. E.* **81**, 026308 (2010).

[39] Tassieri, M., Evans, R., Warren, R. L., Bailey, N. J. & Cooper, J. M. Microrheology with optical tweezers: data analysis. *New J. Phys.* **14**, 115032 (2012).

[40] Reiner, M. The Deborah number. *Physics Today* (1964).

[41] Baumgartl, J. *et al.* Optical path clearing and enhanced transmission through colloidal suspensions. *Opt. Express* **18**, 17130 (2010).

[42] Allen, L., Beijersbergen, M. W., Spreeuw, R. J. C. & Woerdma, J. P. Orbital angular momentum of light and the transformation of Laguerre-Gaussian laser modes. *Phys. Rev. A.* **45**, 8185 (1992).

[43] Maurer, C., Jesacher, A., Bernet, S. & Ritsch-Marte, M. What spatial light modulators can do for optical microscopy. *Laser Photon. Rev.* **5**, 81 (2011).

[44] Lee, M. *et al.* A multi-modal stereo microscope based on a spatial light modulator. *Opt. Express* **21**, 16541 (2013).

[45] Maurer, C., Khan, S., Fassl, S., Bernet, S. & Ritsch-Marte, M. Depth of field multiplexing in microscopy. *Opt. Express* **18**, 3023 (2010).

[46] Maurer, C., Jesacher, A., Bernet, S. & Ritsch-Marte, M. Phase contrast microscopy with full numerical aperture illumination. *Opt. Lett.* **16**, 19821 (2008).

[47] Bhaduri, B. *et al.* Cardiomyocyte imaging using real-time spatial light interference microscopy (SLIM). *PloS one* **8**, e56930 (2013).

[48] Wang, Z. *et al.* Spatial light interference microscopy (SLIM). *Opt. Express* **19**, 1016 (2011).

[49] McIntyre, T. J., Maurer, C., Bernet, S. & Ritsch-Marte, M. Differential interference contrast imaging using a spatial light modulator. *Opt. Lett.* **34**, 2988 (2009).

[50] Bernet, S., Jesacher, A., Fürhapter, S., Maurer, C. & Ritsch-Marte, M. Quantitative imaging of complex samples by spiral phase contrast microscopy. *Opt. Express* **14**, 3792 (2006).

[51] Fürhapter, S., Jesacher, A., Bernet, S. & Ritsch-Marte, M. Spiral phase contrast imaging in microscopy. *Opt. Express* **13**, 689 (2005).

[52] Grover, G., DeLuca, K., Quirin, S., DeLuca, J. & Piestun, R. Super-resolution photon-efficient imaging by nanometric double-helix point spread function localization of emitters (SPINDLE). *Opt. Express* **20**, 26681 (2012).

[53] Pavani, S. R. P. & Piestun, R. Three dimensional tracking of fluorescent microparticles using a photon-limited double-helix response system. *Opt. Express* **16**, 22048 (2008).

[54] Bowman, R., Gibson, D. P. G. & Padgett, M. Stereoscopic particle tracking for 3D touch, vision and closed-loop control in optical tweezers. *J. Opt.* **13**, 044003 (2011).

[55] Hasler, M., Haist, T. & Osten, W. Stereo vision in spatial-light-modulator-based microscopy. *Opt. Lett.* **37**, 2238 (2012).

[56] Hänggi, P., Talkner, P. & Borkovec, M. Reaction-rate theory: fifty years after Kramers. *Rev. Mod. Phys.* **62**, 251 (1990).

[57] Knox, K. J. *et al.* Observation of bistability of trapping position in aerosol optical tweezers. *JOSA B* **27**, 582 (2010).

[58] Meiners, J. C. & Quake, S. R. Direct measurement of hydrodynamic cross correlations between two particles in an external potential. *Phys. Rev. Lett.* **82**, 2211 (1999).

[59] Simon, A. & Libchaber, A. Escape and synchronization of a Brownian particle. *Phys. Rev. Lett.* **68**, 3375 (1992).

[60] Smelyanskiy, V. N., Dykman, M. & Golding, B. Time oscillations of escape rates in periodically driven systems. *Phys. Rev. Lett.* **82**, 3193 (1999).

[61] Lehmann, J., Reimann, P. & Hänggi, P. Surmounting oscillating barriers. *Phys. Rev. Lett.* **84**, 1639 (2000).

[62] Maier, R. S. & Stein, D. L. Noise-activated escape from a sloshing potential well. *Phys. Rev. Lett.* **86**, 3942 (2001).

[63] Seol, Y., Stein, D. L. & Visscher, K. Phase measurements of barrier crossings in a periodically modulated double-well potential. *Phys. Rev. Lett.* **103**, 050601 (2009).

[64] Curran, A., Lee, M. P., Padgett, M. J., Cooper, J. & Leonardo, R. D. Partial synchronization of stochastic oscillators through hydrodynamic coupling. *Phys. Rev. Lett.* **108**, 240601 (2012).

[65] Liesener, J., Reicherter, M., Haist, T. & Tiziani, H. J. Multifunctional optical tweezers using computer-generated holograms. *Opt. Comm.* **185**, 77 (2000).

[66] Leach, J. *et al.* Interactive approach to optical tweezers control. *Appl. Opt.* **45**, 897 (2006).

[67] Alvarez, C. & Tellez, G. Screening of charged spheroidal colloidal particles. *J. Chem. Phys* **133**, 144908 (2010).

[68] Stilgoe, A. B., Heckenberg, N. R., Nieminen, T. A. & Rubinsztein-Dunlop, H. Phase-transition-like properties of double-beam optical tweezers. *Phys. Rev. Lett.* **107**, 248101 (2011).

[69] Dufresne, E. R., Squires, T. M., Brenner, M. P. & Grier, D. G. Hydrodynamic coupling of two Brownian spheres to a planar surface. *Phys. Rev. Lett.* **85**, 3317 (2000).

[70] Curran, A. *et al.* Real time characterization of hydrodynamics in optically trapped networks of micro-particles. *J. Biophoton.* **3**, 244 (2010).

[71] Happel, J. & Brenner, H. *Low Reynolds Number Hydrodynamics* (Kluwer Academic Publishers, Dordrech, 1983).

[72] Weeks, E. R., Crocker, J. C., Levitt, A. C., Schofield, A. & Weitz, D. A. Three-dimensional direct imaging of structural relaxation near the colloidal glass transition. *Science* **287**, 627 (2000).

[73] Hoogenboom, J. P., Vossen, D. L. J., Faivre-Moskalenko, C., Dogterom, M. & van Blaaderen, A. Patterning surfaces with colloidal particles using optical tweezers. *Appl. Phys. Lett.* **80**, 4828 (2002).

[74] Yao, A., Tassieri, M., Padgett, M. & Cooper, J. Microrheology with optical tweezers. *Lab Chip* **9**, 2575 (2009).

[75] Nemet, B. A., Shabtai, Y. & Cronin-Golomb, M. Imaging microscopic viscosity with confocal scanning optical tweezers. *Opt. Lett.* **27**, 264 (2002).

[76] Peterman, E. J. G., Gittes, F. & Schmidt, C. F. Laser-induced heating in optical traps. *Biophys. J.* **84**, 1308 (2003).

[77] Sinclair, G. *et al.* Interactive application in holographic optical tweezers of a multi-plane gerchberg-saxton algorithm for three-dimensional light shaping. *Opt. Express* **12**, 1665–1670 (2004).

[78] Wills, J. B., Butler, J. R., Palmer, J. & Reid, J. P. Using optical landscapes to control, direct and isolate aerosol particles. *Physical Chemistry Chemical Physics* **11**, 8015–8020 (2009).

[79] Lee, M. P. *et al.* Optical shield: measuring viscosity of turbid fluids using optical tweezers. *Opt. Express* **20**, 12127 (2012).

[80] Parkin, S. J., Knöner, G., Nieminen, T. A., Heckenberg, N. R. & Rubinsztein-Dunlop, H. Picoliter viscometry using optically rotated particles. *Phys. Rev. E.* **76**, 041507 (2007).

[81] Preece, D. *et al.* Optical tweezers: wideband microrheology. *Journal of Optics* **13**, 044022 (2011).

[82] Evans, R. M. L., Tassieri, M., Auhl, D. & Waigh, T. A. Direct conversion of rheological compliance measurements into storage and loss moduli. *Phys. Rev. E* **80**, 012501 (2009).

[83] Pommella, A. *et al.* Using optical tweezers for the characterization of polyelectrolyte solutions with very low viscoelasticity. *Langmuir* **29**, 9224–9230 (2013).

[84] Robertson, E. J. *et al.* Cryptococcus neoformans ex vivo capsule size is associated with intracranial pressure and host immune response in hiv-associated cryptococcal meningitis. *Journal of Infectious Diseases* **209**, 74–82 (2014).

[85] Watts, F. *et al.* Investigating the micro-rheology of the vitreous humor using an optically trapped local probe. *Journal of Optics* **16**, 015301 (2014).

[86] Asakura, T. & Takai, N. Dynamic laser speckles and their application to velocity measurements of the diffuse object. *Appl. Phys.* **25**, 179 (1981).

[87] Lavery, M. P. J., Speiritis, F. C., Barnett, S. M. & Padgett, M. J. Detection of a spinning object using light's orbital angular momentum. *Science* **341**, 537 (2013).

[88] Rosales-Guzmán, C., Hermosa, N., Belmonte, A. & Torres, J. P. Experimental detection of transverse particle movement with structured light. *Sci. Rep.* **3** (2013).

[89] Korech, O., Steinitz, U., Gordon, R. J., Averbukh, I. S. & Prior, Y. Observing molecular spinning via the rotational doppler effect. *Nat. Photon.* **7**, 711 (2013).

[90] Leach, J., Keen, S., Padgett, M. J., Saunter, C. & Love, G. D. Direct measurement of the skew angle of the poynting vector in a helically phased beam. *Opt. Express* **14**, 11919 (2006).

[91] Courtial, J., Robertson, D. A., Dholakia, K., Allen, L. & Padgett, M. J. Rotational frequency shift of a light beam. *Phys. Rev. Lett.* **81** (1998).

[92] Nienhuis, G. Doppler effect induced by rotating lenses. *Opt. Comm.* **132**, 8 (1996).

[93] Friese, M. E. J., Nieminen, T. A., Heckenberg, N. R. & Rubinsztein-Dunlop, H. Optical alignment and spinning of laser-trapped microscopic particles. *Nature* **394**, 348 (1998).

[94] Bowman, R. W. *et al.* Red tweezers: Fast, customisable hologram generation for optical tweezers. *Comput. Phys. Commun.* **185**, 268 (2013).

[95] Soskin, M. S., Gorshkov, V. N., Vasnetsov, M. V., Malos, J. T. & Heckenberg, N. R. Topological charge and angular momentum of light beams carrying optical vortices. *Phys. Rev. A.* **56**, 4064 (1997).

[96] Phillips, D. B. *et al.* Optimizing the optical trapping stiffness of holographically trapped microrods using high-speed video tracking. *J. Opt.* **13**, 044023 (2011).

[97] MacDonald, D. *Noise and Fluctuations: An Introduction* (Wiley, 1962).

[98] Arita, Y., Mazilu, M. & Dholakia, K. Laser-induced rotation and cooling of a trapped microgyroscope in vacuum. *Nat. Commun.* **4**, 2374 (2013).

[99] Murphy, D. B. *Fundamentals of Light Microscopy and Electronic Imaging* (Wiley-Blackwell, 2001).

[100] Haist, T., Hasler, M., Osten, W. & Baranek, M. *Programmable Microscopy, in Multi-Dimensional Imaging* (John Wiley and Sons, Ltd, 2014).

[101] Davis, J. A., McNamara, D. E., Cottrell, D. M. & Campos, J. Image processing with the radial hilbert transform: theory and experiments. *Opt. Lett.* **25**, 99 (2000).

[102] Guo, C. S., Han, Y. J., Xu, J. B. & Ding, J. Radial Hilbert transform with Laguerre-Gaussian spatial filters. *Opt. Lett.* **31**, 1394 (2006).

[103] Situ, G., Pedrini, G. & Osten, W. Spiral phase filtering and orientation-selective edge detection/enhancement. *J. Opt. Soc. Am. A.* **26**, 1788 (2009).

[104] Blanchard, P. M. & Greenaway, A. H. Simultaneous multiplane imaging with a distorted diffraction grating. *Appl. Opt.* **38**, 6692 (1999).

[105] Sierra, H., Zheng, J.-Y., Rabin, B. & Boustany, N. N. Measurement of object structure from size-encoded images generated by optically-implemented Gabor filters. *Opt. Express* **20**, 28698 (2012).

[106] Greengard, A., Schechner, Y. Y. & Piestun, R. Depth from diffracted rotation. *Opt. Lett.* **31**, 181 (2006).

[107] Lew, M. D., Lee, S. F., Badieirostami, M. & Moerner, W. Corkscrew point spread function for far-field three-dimensional nanoscale localization of pointlike objects. *Opt. Lett.* **36**, 202 (2011).

[108] Camacho, L., Micó, V., Zalevsky, Z. & Garcí, J. Quantitative phase microscopy using defocusing by means of a spatial light modulator. *Opt. Express* **18**, 6755 (2010).

[109] Gibson, G. M. *et al.* A compact holographic optical tweezers instrument. *Rev. Sci. Instrum.* **83**, 113107 (2012).

[110] Radwell, N., Boukhet, M. A. & Franke-Arnold, S. 3d beam reconstruction by fluorescence imaging. *Optics express* **21**, 22215–22220 (2013).

[111] Dowski, E. R. & Cathey, W. T. Extended depth of field through wave-front coding. *Appl. Opt.* **34**, 1859 (1995).

[112] Poon, T.-C. & Motamedi, M. Optical/digital incoherent image processing for extended depth of field. *Appl. Opt.* **26**, 4612 (1987).

[113] Siviloglou, G. A., Broky, J., Dogariu, A. & Christodoulides, D. N. Observation of accelerating Airy beams. *Phys. Rev. Lett.* **99**, 213901 (2007).

[114] Zernike, F. How I discovered phase contrast. *Science* **121**, 345 (1955).

[115] Montes-Usategui, M., Pleguezuelos, E., Andilla, J. & Martín-Badosa, E. Fast generation of holographic optical tweezers by random mask encoding of fourier components. *Opt. Express* **14**, 2101–2107 (2006).

[116] Wulff, K. D. *et al.* Aberration correction in holographic optical tweezers. *Opt. Express* **14**, 4170 (2006).

[117] Bowman, R. W., Wright, A. J. & Padgett, M. J. An SLM-based shack–hartmann wavefront sensor for aberration correction in optical tweezers. *J. Opt.* **12**, 124004 (2010).

[118] Dam, J. S., Perch-Nielsen, I. R., Palima, D. & Glückstad, J. Three-dimensional optical multi-beam micromanipulation. *Opt. Express* **16**, 7244 (2008).

[119] Quirin, S., Peterka, D. S. & Yuste, R. Instantaneous three-dimensional sensing using spatial light modulator illumination with extended depth of field imaging. *Opt. Express* **21**, 16007 (2013).

[120] Leitz, G., Kang, B.-H., Schoenwaelder, M. E. & Staehelin, L. A. Statolith sedimentation kinetics and force transduction to the cortical endoplasmic reticulum in gravity-sensing arabidopsis columella cells. *Plant Cell* **21**, 843 (2009).

[121] Heitkam, S. *et al.* Speeding up of sedimentation under confinement. *Phys. Rev. Lett.* **110**, 178302 (2013).

[122] Blazejewsk, R. Apparent viscosity and settling velocity of suspensions of rigid monosized spheres in stokes flow. *Int. J. Multiph. Flow.* **39**, 179 (2012).

[123] Palacci, J., Cottin-Bizonne, C., Ybert, C. & Bocquet, L. Sedimentation and effective temperature of active colloidal suspensions. *Phys. Rev. Lett.* **105**, 088304 (2010).

[124] Juhl, A. T. *et al.* Ordering of glass rods in nematic and cholesteric liquid crystals. *Opt. Mater. Express* **8**, 1536 (2011).

[125] Gosse, C. & Croquette, V. Magnetic tweezers: micromanipulation and force measurement at the molecular level. *Biophys. J.* **62**, 3314 (2002).

[126] Michalet, X. Mean square displacement analysis of single-particle trajectories with localization error: Brownian motion in an isotropic medium. *Phys. Rev. E* **82**, 041914 (2010).